



## **Ion thrusters for electric propulsion: Scientific issues developing a niche technology into a game changer**

Holste Kristof, Patrick Dietz, Steffen Scharmann, Konstantin Keil, Thomas Henning, D. Zschätzsch, M. Reitemeyer, B. Nauschütt, F. Kiefer, F. Kunze, et al.

### **► To cite this version:**

Holste Kristof, Patrick Dietz, Steffen Scharmann, Konstantin Keil, Thomas Henning, et al.. Ion thrusters for electric propulsion: Scientific issues developing a niche technology into a game changer. Review of Scientific Instruments, 2020, 91 (6), pp.061101. 10.1063/5.0010134 . hal-03201691

**HAL Id: hal-03201691**

**<https://hal.science/hal-03201691>**

Submitted on 19 Apr 2021







**HAL** is a multi-disciplinary open access archive for the deposit and dissemination of scientific research documents, whether they are published or not. The documents may come from teaching and research institutions in France or abroad, or from public or private research centers.

L'archive ouverte pluridisciplinaire **HAL**, est destinée au dépôt et à la diffusion de documents scientifiques de niveau recherche, publiés ou non, émanant des établissements d'enseignement et de recherche français ou étrangers, des laboratoires publics ou privés.

# Ion thrusters for electric propulsion: Scientific issues developing a niche technology into a game changer F

Cite as: Rev. Sci. Instrum. **91**, 061101 (2020); <https://doi.org/10.1063/5.0010134>

Submitted: 08 April 2020 . Accepted: 18 May 2020 . Published Online: 24 June 2020

 K. Holste, P. Dietz, S. Scharmann, K. Keil,  T. Henning, D. Zschätzsch, M. Reitemeyer, B. Nauschütt, F. Kiefer, F. Kunze, J. Zorn, C. Heiliger, N. Joshi, U. Probst, R. Thüringer,  C. Volkmar, D. Packan, S. Peterschmitt, K. -T. Brinkmann, H.-G. Zaunick, M. H. Thoma,  M. Kretschmer, H. J. Leiter,  S. Schippers, K. Hannemann, and  P. J. Klar

## COLLECTIONS

F This paper was selected as Featured



View Online



Export Citation



CrossMark

## ARTICLES YOU MAY BE INTERESTED IN

[Space micropropulsion systems for Cubesats and small satellites: From proximate targets to furthestmost frontiers](#)

Applied Physics Reviews **5**, 011104 (2018); <https://doi.org/10.1063/1.5007734>

[Tutorial: Physics and modeling of Hall thrusters](#)

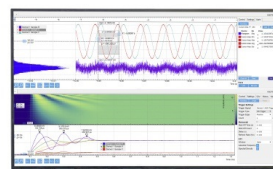
Journal of Applied Physics **121**, 011101 (2017); <https://doi.org/10.1063/1.4972269>

[Jet propulsion by microwave air plasma in the atmosphere](#)

AIP Advances **10**, 055002 (2020); <https://doi.org/10.1063/5.0005814>

## Challenge us.

What are your needs for  
periodic signal detection?



Zurich  
Instruments



# Ion thrusters for electric propulsion: Scientific issues developing a niche technology into a game changer

Cite as: Rev. Sci. Instrum. 91, 061101 (2020); doi: 10.1063/5.0010134

Submitted: 8 April 2020 • Accepted: 18 May 2020 •

Published Online: 24 June 2020



K. Holste,<sup>1,a)</sup>  P. Dietz,<sup>1</sup> S. Scharmann,<sup>1</sup> K. Keil,<sup>1</sup> T. Henning,<sup>1</sup>  D. Zschätzsch,<sup>1</sup> M. Reitemeyer,<sup>1</sup> B. Nauschütt,<sup>1</sup> F. Kiefer,<sup>1</sup> F. Kunze,<sup>1</sup> J. Zorn,<sup>1</sup> C. Heiliger,<sup>2</sup> N. Joshi,<sup>2</sup> U. Probst,<sup>3</sup> R. Thüringer,<sup>3</sup> C. Volkmar,<sup>3</sup>  D. Packan,<sup>4</sup> S. Peterschmitt,<sup>4</sup> K. -T. Brinkmann,<sup>5</sup> H.-G. Zaunick,<sup>5</sup> M. H. Thoma,<sup>1</sup> M. Kretschmer,<sup>1</sup>  H. J. Leiter,<sup>1</sup> S. Schippers,<sup>1</sup>  K. Hannemann,<sup>1,6</sup> and P. J. Klar<sup>1</sup> 

## AFFILIATIONS

<sup>1</sup>Institute of Experimental Physics I, Justus Liebig University, Heinrich-Buff-Ring 16, 35392 Giessen, Germany

<sup>2</sup>Institute of Theoretical Physics, Justus Liebig University, Heinrich-Buff-Ring 16, 35392 Giessen, Germany

<sup>3</sup>Department of Electrical Engineering, University of Applied Sciences, Wiesenstr. 14, 35390 Giessen, Germany

<sup>4</sup>ONERA, Palaiseau 91120, France

<sup>5</sup>Institute of Experimental Physics II, Justus Liebig University, Heinrich-Buff-Ring 16, 35392 Giessen, Germany

<sup>6</sup>German Aerospace Center, Institute of Aerodynamics and Flow Technology, Spacecraft Department, Bunsenstrasse 10, 37073 Goettingen, Germany

<sup>a)</sup>Author to whom correspondence should be addressed: [Kristof.Holste@physik.uni-giessen.de](mailto:Kristof.Holste@physik.uni-giessen.de)

## ABSTRACT

The transition from OLD SPACE to NEW SPACE along with increasing commercialization has a major impact on space flight, in general, and on electric propulsion (EP) by ion thrusters, in particular. Ion thrusters are nowadays used as primary propulsion systems in space. This article describes how these changes related to NEW SPACE affect various aspects that are important for the development of EP systems. Starting with a historical overview of the development of space flight and of the technology of EP systems, a number of important missions with EP and the underlying technologies are presented. The focus of our discussion is the technology of the radio frequency ion thruster as a prominent member of the gridded ion engine family. Based on this discussion, we give an overview of important research topics such as the search for alternative propellants, the development of reliable neutralizer concepts based on novel insert materials, as well as promising neutralizer-free propulsion concepts. In addition, aspects of thruster modeling and requirements for test facilities are discussed. Furthermore, we address aspects of space electronics with regard to the development of highly efficient electronic components as well as aspects of electromagnetic compatibility and radiation hardness. This article concludes with a presentation of the interaction of EP systems with the spacecraft.

© 2020 Author(s). All article content, except where otherwise noted, is licensed under a Creative Commons Attribution (CC BY) license (<http://creativecommons.org/licenses/by/4.0/>). <https://doi.org/10.1063/5.0010134>

## NOMENCLATURE

AEPD	advanced electric propulsion platform	CEX	charge exchange
AEHF	advanced extremely high frequency	CME	coronal mass ejection
BBi	beamlet–beamlet interaction	COTS	custom-off-the-shelf
BEB	binary encounter Bethe	CS	conducted susceptibility
CE	conducted emission	DETOF	delayed extraction time-of-flight
		DSMC	direct simulation Monte Carlo
		DUT	device under test

ECR	electron cyclotron resonance
ECRT	electron cyclotron resonance thruster
EMC	electromagnetic compatibility
EOR	electric orbit raising
EP	electric propulsion
FEPP	field-emission electric propulsion
GEO	geostationary orbit
GIE	gridded ion engine
GMAT	general mission analysis tool
GSO	geosynchronous orbit
GTEM	gigahertz transverse electromagnetic
GTO	geosynchronous transfer orbit
HELT	helicon thruster
HEMPT	high efficiency multistage plasma thruster
HET	Hall effect thruster
IBS	ion-beam shepherd
ICT	impulse compensation thruster
ILIS	ionic liquid ion source
Isp	specific impulse
ISS	International Space Station
JLU	Justus Liebig University of Giessen
LEO	low Earth orbit
LISA	laser interferometer space antenna
LLST	low-low satellite tracking
LMIS	liquid metal ion source
LN2	liquid nitrogen
LOX	liquid oxygen
MCC	Monte Carlo collision
MEMS	microelectromechanical system
MPDT	magnetoplasmadynamic thruster
NCHS	neutralizer cathode heater power supply
NGGM	next generation gravity mission
NHV	negative high voltage
NIEL	non-ionizing energy loss
NKS	neutralizer keeper power supply
NSSK	north-south station-keeping
PCU	power control unit
PHV	positive high voltage
PIC	particle in cell
PPA	parallel plate analyzer
PPT	pulsed plasma thruster
PPU	power processing unit
PTFE	polytetrafluorethylene
RAM-EP	residual atmosphere electric propulsion
RE	radiated emission
RFG	radio frequency generator
RIT	radio frequency ion thruster
RPA	retarding potential analyzer
RS	radiated susceptibility
SC	spacecraft
SEB	single event burn-out
SEE	single event effect
SEL	single event latch-up
SEM	scanning electron microscopy
SET	single event transient
SEU	single event upset
SME	small or medium enterprise
SPT	stationary plasma thruster

SSG	secondary star ground
TID	total ionizing dose
TOF	time of flight
ZCS	zero current switching
ZVS	zero voltage switching

## I. INTRODUCTION

Until recently, the exploration of space had been subjected to strong political and economic constraints due to the immense costs involved. As a result, space was only accessible to countries that had the necessary financial and technological resources. The organization of space missions was the responsibility of potent space agencies such as ESA, NASA, JAXA, CNSA, ISRO, or ROSCOSMOS. The fields of activity of these agencies were manifold. As governmental institutions, they also fulfilled societal functions such as in education, as knowledge carriers, and in transferring and promoting technology. Furthermore, they developed into a large scientific, technical, and administrative apparatus. In the case of ESA, a multitude of national interests need to be accounted for in the running of the institution and in day-to-day routine.<sup>1</sup> The funds spent by the agencies typically are distributed to a great extent among a few long-established suppliers. In the case of ESA, 85% of the budget in 2017 was distributed to European industry, but only ~6% was distributed to SMEs.<sup>2</sup> As a result, a high-tech space community with reliable products has been established from the alliance of agencies and industry, which only to a limited extent was subjected to the laws of the free market. These structures and scenarios are referred to as “OLD SPACE.” Since the beginning of the new millennium, however, a paradigm shift, which is often referred to as “NEW SPACE,” has taken place.<sup>3</sup> A number of companies have emerged with the aim of carrying out space missions at a fraction of the cost spent before and accepting the risk of failure in space due to shorter development times and cheaper production. This group of companies includes Blue Origin, Rocketplane Kistler, or SpaceX, to name a few. This has resulted, for instance, in the Commercial Orbital Transportation Services program, which is funded by NASA with \$500 million to restore US access to the International Space Station (ISS) with the help of private-sector companies as there was no replacement after the Space Shuttle was decommissioned in 2011.

Irrespective of how the established structures between agencies, established industries, and newly created companies will reform, it can be said that this process will have a significant impact on the space technology sector. We believe that it will affect all branches of space industry and, in particular, the electric propulsion (EP) sector. There are also a number of new companies in the EP sector—similar to the case of the big launchers—which are offering low-cost EP systems for satellites and competing with the incumbent companies. Many of these propulsion systems focus on smaller satellites, which are currently gaining importance, principally due to the low cost of a rocket launch facilitated by NEW SPACE, e.g., in the context of mega constellations.<sup>4</sup> Despite the ongoing commercialization of EP systems, a number of requirements, somewhat similar to those of the established chemical systems, have to be met by these propulsion systems, such as reliability, robustness, electromagnetic compatibility (EMC), radiation hardness, non-hazardous interaction with the satellite, and energy efficiency. In addition, the speed of development, improvement, and adaptation of propulsion



systems to the conditions of the specific mission has to increase for reasons of competitiveness. This will only be achieved if suitable test facilities with standardized measurement procedures and validated computer-aided modeling of the engines are both available for developers.

The aim of this article is to give an overview of established EP systems and to discuss the impact of *NEW SPACE* on these matured devices. In addition, the effects of the ongoing commercialization on the boundary conditions necessary for the development of EP systems will be addressed. The focus will be on ion propulsion systems, in particular, on the technology of gridded ion engines (GIE) such as the radio-frequency ion-thruster (RIT). Hall effect thrusters (HETs) belong to another class of ion propulsion systems and are only briefly described and discussed for comparison. For more detailed information on HETs, we refer the reader to the numerous excellent overview articles and the references mentioned therein.<sup>5–8</sup> The article is structured as follows: Since *NEW SPACE* is a change of course in the field of space travel, we first like to show the chronological development that led to the grown structures of *OLD SPACE* and how they fit in with the new boundary conditions. Section II A therefore gives a brief overview of the history of space travel, which is characterized by the development of chemical high-thrust propulsion systems, and traces the parallel development of EP systems, which have increasingly evolved from their niche existence over time. Based on this, a series of missions will be presented in Sec. II B whose implementation or success is or was largely determined by EP. The challenges we have identified in the field of EP resulting from its commercialization are discussed in Sec. II C. The major EP thruster concepts are briefly introduced in Sec. III A, and the basic quantities for describing these thrusters are discussed in Sec. III B. For comparison, references will be made to chemical thrusters. Using the example of the RIT, deeper aspects of ion propulsion will be discussed in Sec. III C. The focus on this thruster type has two reasons. On the one hand, there are—in contrast to the RIT technology—a number of overview articles about other thruster types, especially the aforementioned Hall thrusters. On the other hand, RIT is a propulsion technology that was developed at the Justus Liebig University of Giessen (JLU) and is therefore also in the focus of our research activities. Hence, a number of RIT-related aspects that we consider important will be discussed in more detail at appropriate points. The challenges identified in EP are discussed in more detail in Sec. IV. These comprise the search of alternative propellants (Sec. IV A), the development of reliable neutralizers with low work function insert materials (Sec. IV B), neutralizer-free thrusters (Sec. IV C), modeling of thrusters and facilities (Sec. IV D), test facilities and standardization of test procedures (Sec. IV E), miniaturized thrusters for small satellites (CubeSats) (Sec. IV F), electronics developments (Sec. IV G), electromagnetic compatibility (Sec. IV H), radiation hardness of electronics (Sec. IV I), and spacecraft (SC)/EP interaction (Sec. IV J). An outlook is given in Sec. V.

## II. FROM THE BEGINNINGS OF SPACE TRAVEL TO THE ALL-EP SYSTEM

### A. Brief history of space flight

For almost 100 years now, one can speak of space travel as an independent discipline. It started with the visionary theoretical

work of Tsiolkovsky, Goddard, and Oberth at the beginning of the 20th century and has been followed by first experimental successes, especially through the work of Goddard, who was the first to construct a rocket that succeeded in breaking the sound barrier in 1935.<sup>9–12</sup> Development work on the Redstone rockets began in the United States of America (USA) in Huntsville (Alabama) in 1950 and was led by von Braun. Parallel development work on the Atlas intercontinental rocket was led by the part of the Air Force.<sup>13,14</sup> The Redstone rockets have been based on the technology of the A4 rocket, which was developed prior and during the Second World War by German scientists headed by von Braun and depicted the low point of this phase of rocket development, both through its use as weapon and through its production with the help of forced labourers.<sup>15,16</sup>

The works of the period after 1945 were significantly influenced by the Cold War between the US and the Soviet Union.<sup>17</sup> Both countries possessed the atomic bomb and hoped for an advantage or a deterrent potential to bring this threat to its destination with intercontinental missiles. During this heated period, the Soviet Union initially had a technological advantage. Thus, the age of space exploration began with *Sputnik-1*, the first man-made satellite on an orbit in the Low Earth Orbit (LEO), on 4 October 1957. Only a few days later, on 3 November 1957, the follow-up mission *Sputnik-2* succeeded in bringing the first living creature into orbit, the female dog Laika. *Sputnik-2* may therefore be regarded as the first test toward manned space flight as it was controversially discussed until then even whether living beings could survive in weightlessness for a longer period of time. The biomedical data obtained on this mission also contributed significantly to the success of the *Vostok-1* mission with Yuri Gagarin. Although *Sputnik-1* was technically only able to send a steady beeping sound toward Earth, it demonstrated that the Soviet Union had the advantage and could now reach American territory with intercontinental missiles. This significantly increased American efforts to close this technological gap. Subsequently, during the development of the first artificial American satellite (*Explorer 1*), the radiation belts, which had been suspected for a long time, were discovered by Van Allen, who was responsible for the measurement technology on board *Explorer 1*. Van Allen studied them with regard to their radiation strength.<sup>18</sup> Physical parameters such as the Earth's magnetic field and the radiation levels from the Sun were determined in follow-up missions. The backwardness of the US in the development of space technology led to the foundation of the National Aeronautics and Space Administration (NASA) in 1958. The founder president Dwight D. Eisenhower immediately launched a manned space program, the Mercury Project (1958–1963), which was later continued as Gemini (1965–1966) and Apollo (1961–1972) programs. Despite these increased efforts on part of the US, the Soviet Union managed to maintain its leadership. On 12 April 1961, Yuri Gagarin was the first human being in space to circumnavigate the Earth at an altitude of about 300 km with the spaceship *Vostok 1*. This was only just a few months before the maiden flight of the American Alan Shepard in a Redstone rocket. The Americans subsequently succeeded in clearing the backlog. On behalf of von Braun, the Rocketdyne company developed the F-1 rocket engine, a high-thrust rocket motor with 670 tons of thrust (6.7 MN) for a potential manned journey to the Moon. Only a few years later, on 21 July 1969, Neil Armstrong and Buzz Aldrin were the first men to set foot on the Moon in the

context of the *Apollo 11* mission. After this up to now most important event in the history of space travel, the public perception has faded considerably. Nevertheless, this quieter phase of space travel, which continues to this day, is marked by far-reaching developments, which include electric spaceflight propulsion systems, especially ion engines.

Since the very beginning of modern astronautics, EP was considered an option for spacecraft transportation.<sup>19,20</sup> Already in 1906, Goddard speculated that electron acceleration by an electric field might be utilized for propelling a spacecraft. In 1917, he submitted a patent on the first electrostatic ion thruster, which was issued in 1920.<sup>21</sup> Tsiolkovsky realized that electricity may be used to eject particles with a large velocity from rocket devices. Between 1919 and 1938, Kondratyuk came up with an idea that may be considered the first sketch of a colloid thruster.<sup>19</sup> The first more substantial concepts were proposed by Oberth, who devoted an entire chapter, entitled *Das elektrische Raumschiff* (*The electric spaceship*), to EP in his famous text book *Wege zur Raumschiffahrt* (*Ways to Spaceflight*) published 1929. Between 1929 and 1933, Glushko probably built the first electric thruster, an electrothermal version, and tested it on a thrust stand. Shepherd and Cleaver published in 1948/1949 a series of four articles on nuclear thermal propulsion and gave the first analysis on the feasibility of electrostatic propulsion, recognizing the necessity of using a propellant with large atomic mass and the importance of beam neutralization.<sup>22–25</sup> However, they concluded that the minimum acceleration of a spacecraft caused by EP, which they estimated as 0.01 g, would render ion thrusters impractical. Fortunately, Spitzer realized in 1951 that a much lower acceleration ( $3 \times 10^{-4}$  g) with  $g = 9.81 \text{ ms}^{-2}$  would be sufficient for space applications and feasible. Comprehensive and systematic investigations of EP, in particular, ion thrusters, by Stuhlinger started around 1954 and led to his standard reference text book *Ion Propulsion for Space Flight* published in 1964.<sup>26</sup> In the following years, the basic thruster types were developed, which have proved to be successful and are still in use today. These include the electron-bombardment engines, developed by Kaufman; the radio frequency ion engines, developed by Löb; and the stationary plasma thruster (SPT, also known as Hall Thrusters), developed by Morozov.<sup>27–32</sup>

The development of space travel has always been and still is a reflection of the technical possibilities of the respective epoch and always is connected with scientific, political, military, and economic objectives. After the race in space had ended with the moon landing of the Americans at the time of the Cold War, civil, i.e., commercial and scientific interests of space travel began to develop in addition to the military one. Nowadays, economic aspects have become a main driving force and commercial aspects play a major role in space travel. Scientific and technical developments are increasingly aimed at optimizing efficiency. Solar cells became more and more powerful through the use of III–V compound semiconductor technology, i.e., they achieved higher electrical efficiencies while simultaneously increasing their radiation hardness. Better solar technology increased the amount of electrical power available on a satellite.<sup>33,34</sup> This increase enables the rather triumphal advance of EP systems.

Since the thrust  $T$  of a propulsion system is composed of the product of the ejection velocity and the mass of propellant emitted per time interval,  $\dot{m}$ , i.e.,

$$T = -v_{\text{ex}} \cdot \dot{m}, \quad (1)$$

increasing the ejection velocity will save a certain amount of propellant for the same thrust. Achievable ejection velocities in EP are about 10 times higher than in chemical propulsion. A satellite that is electrically propelled can therefore get by with less propellant, which leads to a significant cost saving, on the one hand, since this propellant does not have to be carried from Earth into space. On the other hand, requiring less propellant increases the payload ratio, i.e., an electrically propelled satellite can be equipped with a much larger payload. This relationship, which follows from the Tsiolkovsky equation, is

$$\frac{m_d}{m_0} = \exp\left(\frac{-\Delta v}{v_{\text{ex}}}\right) \quad (2)$$

and is shown in Fig. 1(a) as an example for three different  $\Delta v$ -values as a function of the exhaust velocity. Here,  $m_d$  stands for the dry mass of the satellite (without propellant),  $m_0$  stands for the total mass of the satellite (including all propellants), and  $\Delta v$  stands for the change in velocity, which can be achieved by mass ejection with an exhaust velocity  $v_{\text{ex}}$ . According to Löb, the exhaust velocity of chemical fuels depends theoretically only on the energy yield  $\omega$ , i.e., the ratio of the enthalpy change  $H_p$  during combustion and the rest energy of the propellant,<sup>31</sup>

$$\omega = \frac{H_p}{m_p c^2}. \quad (3)$$

It results in  $v_{\text{ex}} = c\sqrt{2\omega - \omega^2}$ , where  $\omega^2$  can be neglected for chemical thrusters. The energy yield  $\omega$  of chemical propellants is about  $10^{-10}$ – $10^{-9}$  and provides theoretical exhaust velocities between 4.5 km/s for kerosene–oxygen and 5.2 km/s for hydrogen–oxygen mixtures (all components being liquid). These values are significantly lower due to real existing combustion thruster efficiencies (about 4.3 km/s for LH2–LOX). In the field of chemical propulsion, there have been a number of efforts for decades to find high-energy density materials providing high exhaust velocities. There are older approaches, e.g., by triergolic combinations of fuels, e.g., the oxidation of beryllium via  $\text{BeH}_2$ – $\text{H}_2$ – $\text{O}_2$  or hydrogen–radicals, to achieve significantly higher exhaust velocities, but these have not yet been successfully implemented. Other potentially interesting materials are high-nitrogen compounds, octanitrocubanes, metallic hydrogen, atomic radicals, metastable helium, etc. However, many of these approaches are at a very low level of maturity and some are of theoretical nature only.<sup>35</sup>

Thus, for chemical thrusters, the maximum  $v_{\text{ex}}$  is about 5 km/s. EP systems such as resistojets or arcjets, which heat the propellant electrically and then eject it, possess exhaust velocities in a comparable range.<sup>36</sup> In contrast, highly mass efficient systems such as the ion propulsion systems yield propellant exhaust velocities of 30 km/s–40 km/s. It can be seen very clearly in Fig. 1(a) that especially for missions requiring a large  $\Delta v$ , the use of EP is mandatory as such missions are not feasible with chemical propulsion alone. Even north-south station-keeping (NSSK), i.e., maintaining and aligning a satellite in its geosynchronous orbit (GSO), for which a  $\Delta v$  of only 1 km/s is needed over a period of time of about 15 years, benefits significantly from EP. It should be noted that we prefer the term GSO, which as a special case includes the geostationary orbit (GEO). Nevertheless, we will occasionally use the term GEO in cases where references use this term. When using an ion propulsion system for

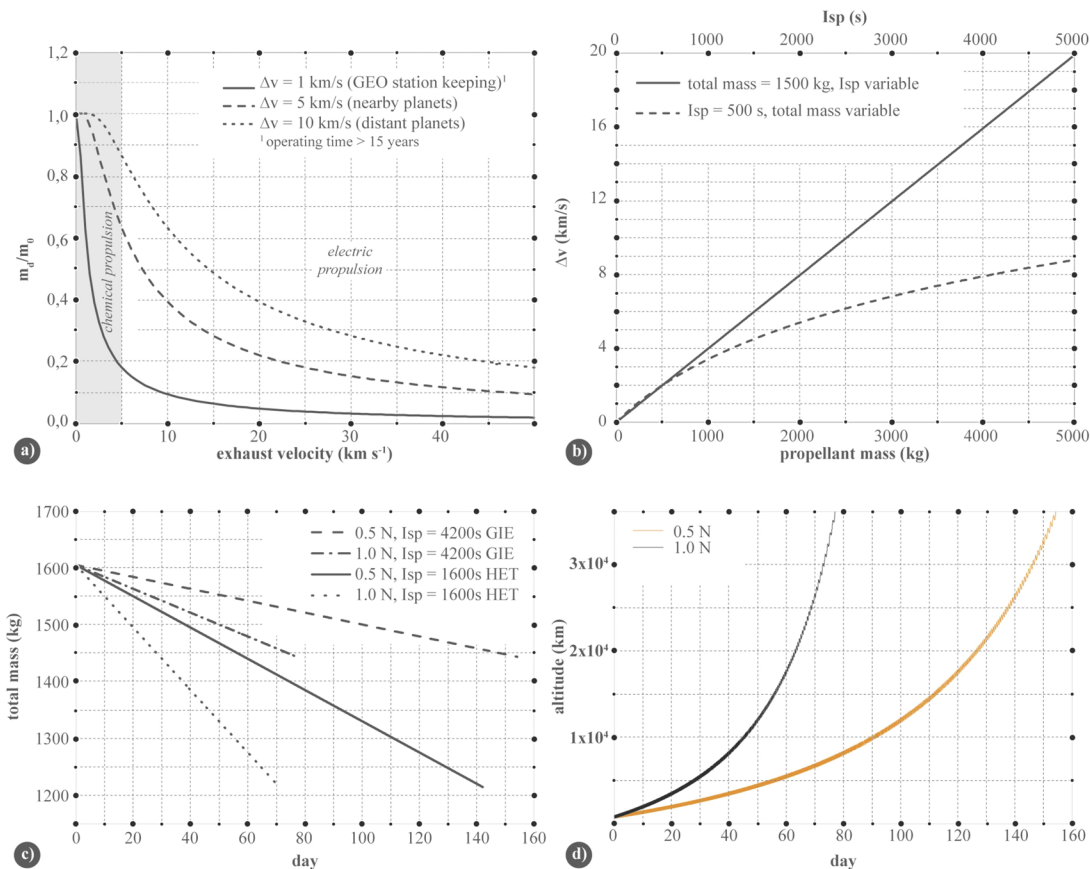


**FIG. 1.** (a) Ratio of dry mass  $m_d$  to the total mass of a satellite  $m_0$  as a function of the exhaust velocity of the propellant for specific constant  $\Delta v$  values. The gray-shaded area corresponds to the typical exhaust velocities of chemical engines. (b) Dependence of the velocity increment  $\Delta v$  [see Eq. (2)] on the total mass [for a constant Isp of 500 s (chemical propulsion) and a fixed dry mass of 1000 kg] and on the Isp (for a constant total mass of 1500 kg and dry mass of 1000 kg). The definition of Isp, which is a measure of mass efficiency, is given in Eq. (4). The Isp values cover the range from 500 s (typical for chemical propulsion) to 5000 s (typical for a GIE). It is clearly evident that it is uneconomic and technically challenging to increase  $\Delta v$  by solely increasing the wet mass. (c) Spiraling of a satellite from the transfer to geosynchronous orbit with the help of an electric thruster. Calculations were done with the software GMAT (see also Ref. 44) for a satellite of dry mass 850 kg, which carries 756 kg xenon as the propellant. The satellite starts at the coordinates  $x = 7100 \text{ km}$ ,  $y = 0 \text{ km}$ ,  $z = 1300 \text{ km}$ . The initial velocity is  $v_y = 7.35 \text{ km/s}$ . Calculations were made with an Isp of 4200 s, representing a gridded ion engine, and 1600 s for a Hall engine (typical, e.g., for an SPT-100) in constant thrust mode (for 1 N and 0.5 N). Plotted is the total mass of the satellite (i.e., the fuel consumption) and the altitude of the satellite as a function of time in days. (d) Altitude as a function of elapsed days for spiraling from GTO to GSO for two different thrusts and an Isp of 4200 s.

NSSK, propellant savings of about 50% are possible in comparison with chemical thrusters providing the same  $\Delta v$ . Considering that each satellite and its propellant mass have to be launched into space by a chemically propelled launcher, the use of EP in space is almost indispensable in order to be commercially viable. Even highly efficient launch vehicles such as *Ariane-5* can only transport a payload of a few tons into the geostationary or transfer orbit despite possessing a launch mass of about 725 tons, i.e., every kilogram saved in propellant for satellite operation is of immense importance.<sup>37</sup>

## B. Missions with EP

Until 2019, more than 500 spacecrafts were equipped with EP thrusters, 340 of them in GSO between 1981 and 2018.<sup>38</sup> Here, we

want to highlight only a selection of space missions using EP (cf. Table I). The chronological development of EP systems over the last decades as well as the frequency of their use for different types of missions is shown in Fig. 2. The first space application of electric thrusters occurred in 1964 with the suborbital mission *SERT-1* (*Space Electric Rocket Test*) by NASA, in which ion engines with mercury and cesium as propellants were tested for 31 min.<sup>39</sup> The Russian space probe *Zond-2* was launched on November 30, 1964, from Baikonur Cosmodrome.<sup>40,41</sup> It was supposed to explore Mars in a flyby mission. However, communication was lost in May 1965 before it reached Mars. *Zond-2* had six pulsed plasma thrusters (PPTs) for attitude control on board, which were tested successfully for 70 min at a distance of  $5.37 \times 10^6 \text{ km}$  from Earth. The thrusters that used PTFE (polytetrafluoroethylene, known as Teflon®) as the

TABLE I. List of selected EP missions. The thrust in mN is given per thruster.

Mission	Objective	Country	Launch	Orbit	Thruster	Propellant	Thrust (mN)	Isp (s)	Purpose
SERT-1	Technology test	US	1964	Sub-orb	Ion	Hg Cs	28 5.6	4900 8050	EP test
Zond-2	Exploration	USSR	1964	Interplanet (Mars)	PPT	Teflon	2	410	EP test
Meteor 1-10	Meteorology	USSR	1971	LEO	Hall	Xe	20	800	Orbit control
Intelsat V 2	Communication	US	1980	GSO	Resistojet	Hydrazine	0.45	300	Station keeping
Telstar 401	Communication	US	1993	GSO	Arcjet (MR-508)	Hydrazine	250	500	Station keeping
Deep Space 1	Technology test	US	1998	Interplanet	Ion (NSTAR)	Xe	20–90	3100	EP test
Artemis	Communication	Europe and Japan	2001	GSO	Ion RIT-10 Kaufman	Xe	15 18	3370	EP test, orbit raising
Smart-1	Technology test	Europe	2003	Moon	Hall	Xe	67	1540	Main propulsion
Hayabusa-1	Exploration	Japan	2003	Interplanet	ECR ion (4 $\mu$ 10)	Xe	8	3000	Main propulsion
Dawn	Exploration	US	2007	Interplanet	Ion (3 NSTAR)	Xe	90	3100	Main propulsion
Goce	Earth observation	Europe	2009	LEO	Ion (2 T5)	Xe	1–20	3000	Air drag compensation
Hayabusa-2	Exploration	Japan	2014	Interplanet	ECR ion (4 $\mu$ 10)	Xe	10	3000	Main propulsion
LISA	Technology test	Europe	2015	L1	Colloid	Cs	0.0001–0.15	240	Orbit and attitude control
Pathfinder									
BepiColombo	Exploration	Europe, Japan	2018	Interplanet (Mercury)	Ion (4 T6)	Xe	145	4000	Main propulsion
Uwe-4	Technology test, nano sat	Germany, Russia	2019	LEO	FEFP	Ga	0.001	Several thousand	Orbit control

propellant and provided a thrust of 2 mN (Isp = 410 s) were developed by the Kurchatov Institute together with today's RSC Energia. *Zond-2* is regarded as the first application of EP in space. The Isp indicates how efficiently the exhausted mass is converted into a change in momentum and is defined in Eq. (4). The first HET was tested on board the Russian meteorological satellite *Meteor 1-10*, launched on December 29, 1971.<sup>42</sup> Two Hall thrusters (SPT-60, stationary plasma thruster) developed by the Kurchatov Institute of Atomic Energy running with xenon were used for orbit control.<sup>43</sup>

One of the first communication satellites with EP was *Intelsat V 2* launched on December 6, 1980, using a resistojet engine with hydrazine as the propellant for NSSK on GSO.<sup>45</sup> At this time, EP systems for station keeping, in particular, resistojets, began to compete commercially with chemical propulsion systems. This trend has continued until today, e.g., on the *Iridium* constellation.<sup>38</sup> Another breakthrough for commercial application was the employment of arcjets, for the first time, on the *Telstar-401* communication satellite in 1993, allowing a large reduction of propellant mass. At the same time, the importance of HETs, originally developed mainly in USSR, increased. This thruster type nowadays dominates the GSO satellite sector (cf. Fig. 2). However, also ion thrusters play a significant role in this market, whereas resistojets and arcjets become less important now.

The success of EP for orbit raising from the geostationary transfer orbit (GTO) to GSO started at the beginning of the new century. In particular, the rescue of the European-Japanese communication

satellite *Artemis* operated by ESA contributed significantly to this utilization concept.<sup>48,49</sup> It was launched on July 12, 2001, on board of an *Ariane 5* rocket. Due to a malfunction of the upper stage, the GTO with a planned apogee of 36 000 km could not be reached. Instead, *Artemis* ended up on an elliptic orbit ( $590 \times 17\,487$  km<sup>2</sup>). The apogee boost motor, originally supposed to raise the satellite to GSO, was just able to bring it to a circular orbit at 31 000 km outside the Van Allen radiation belt. From there, the GSO was reached by employing the four experimental ion thrusters on board. Operating from February to November 2002 with a height increase of 20 km per day, *Artemis* flew on a spiral orbit to GSO and established its destined position in March 2003. Two of the ion engines were RIT-10 engines using xenon with a thrust of 15 mN, and the other two were of the Kaufman type with a thrust of 18 mN. About 90%, corresponding to 6000 h of operation, of this electric orbit raising (EOR) maneuver was performed with the RIT-10. Motivated by this success story, ESA started a program called *Electra* for supporting the European satellite industry in developing EP concepts for EOR and station keeping of telecommunication satellites up to 3 tons.<sup>50</sup> The capability of HETs for EOR was successfully demonstrated in a similar scenario as for the GIEs on the *ARTEMIS* satellite. During the launch of the first Advanced Extremely High Frequency (AEHF) system, an anomaly in the chemical propulsion system also occurred. The chemical propulsion system was intended for a fast passage through the Van Allen belt. Two HETs onboard the AEHF satellite, which should perform EOR to the target orbit after passing



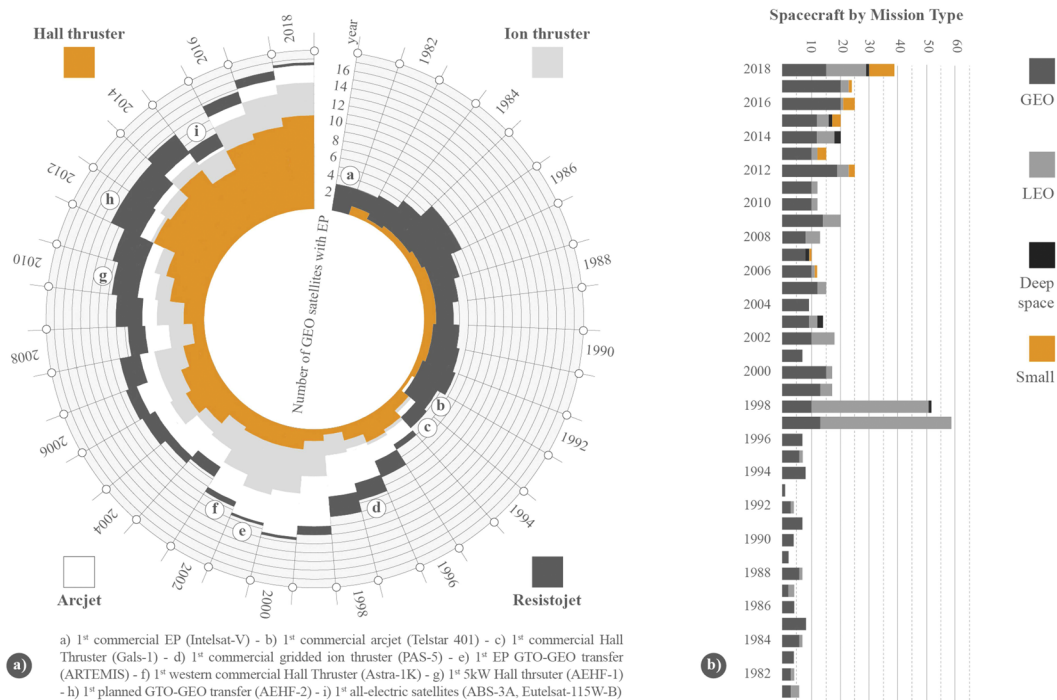


**FIG. 2.** (a) Chronicle of the use of arcjets, resistojets, ion thrusters, and Hall thrusters between 1981 and 2018 in the geosynchronous orbit. (b) Distribution of the thruster types among the mission types GEO, LEO, Deep Space, and small satellites (data taken from Ref. 46). It can be seen that, on the one hand, Hall thrusters and ion thrusters have become the preferred EP systems in recent years. There has also been a steady increase in the use of EP systems and a recent rise in the number of EP systems employed on small satellites. The high number of LEO satellites in 1997/98 can be traced back to the *Iridium* constellation.<sup>47</sup>

the radiation belts, had to be employed already at an earlier stage of the mission.<sup>51</sup> Another demonstration of the powerful capacity of EP for EOR was the lunar probe *SMART-1*.<sup>52–55</sup> This small spacecraft (launch mass 367 kg), designed by the Swedish Space Cooperation, was launched on an *Ariane 5* rocket on September 27, 2003, as a technology demonstrator. It was transported to the Moon on a spiral orbit within 13 months from GTO solely with its solar electric primary propulsion system using a single HET (PPS-1350). The PPS-1350 was operated with xenon as the propellant (propellant mass of 82.5 kg stored at a pressure of 150 bars) and provided a thrust of 70 mN and an Isp of 1600 s and required 1.2 kW of power. After orbiting the Moon for almost two years, it impacted on the Moon's surface as planned on September 3, 2006.

The use of electric thrusters for LEO missions, apart from the *Iridium* satellites, is not established yet. However, since the Starlink constellation of SpaceX adopted HETs using krypton as the propellant for orbit and attitude control, it may be anticipated that the number of LEO satellites using EP will soon increase drastically. Moreover, there are interesting prospects for CubeSats as demonstrated, for example, by the picosatellite *UWE-4* (mass of 1 kg), designed by the University of Würzburg and launched with a Soyuz rocket in 2018, using a small field-effect electric propulsion (FEEP) thruster for orbit control. Another interesting application of EP in LEO is given by the *GOCE* mission where EP was used for atmospheric drag compensation.<sup>56,57</sup> The low flying ESA satellite in a

sun-synchronous circular orbit at 255 km was launched on March 17, 2009, and deorbited on October 21, 2013. Its goal was to map the Earth's gravity field in detail using accelerometers. The continuously operating ion propulsion system compensated the air drag in the low orbit without vibrations, allowing the high-precision measurements to be performed. The EP system consisted of two QinetiQ Kaufman type ion thrusters operated with xenon (40 kg), producing a real time adjustable thrust between 1 mN and 20 mN.

Another important application field for EP are deep space missions for exploration and fundamental research. The first mission of this type was *Deep Space 1* in 1998, which besides technology tests encountered and observed the asteroid (9969) *Braille* and the comet *19P/Borrelly*.<sup>58,59</sup> One of the most important mission goals was the test of the NSTAR (NASA Solar Technology Application Readiness) ion engine providing a thrust of 20 mN–90 mN, which was ignited more than 200 times and run in total for more than 16 000 h, consuming 72 kg of xenon. The proven reliability of this thruster was crucial for the decision to use it for the deep space mission *Dawn*. The NASA space probe *Dawn* was an exploratory mission to the asteroid belt for investigating the asteroid Vesta and the dwarf planet Ceres.<sup>60</sup> *Dawn* is still the only spacecraft entering orbits around two celestial bodies besides Earth. It was launched on September 26, 2007, with a Delta rocket. After reaching the second cosmic velocity, the three NSTAR xenon ion thrusters were ignited. The advantage of EP for this mission was the precise maneuverability allowing to assist

the insertion in the orbits around low-gravity objects and changing orbits around them.<sup>61</sup> For the first time, NASA used EP for an exploratory mission. Similar missions using EP for exploration were the Japanese sample return missions *Hayabusa-1* and *Hayabusa-2*.<sup>62,63</sup> *Hayabusa-1* was launched in 2003 to visit the asteroid *Itokawa*. In addition, here, the precise control of the high specific impulse of the four ECR (electron cyclotron resonance) ion thrusters ( $\mu 10$ ) was a big advantage. The return to Earth was accomplished by the EP system alone due to a failure of the chemical thrusters.<sup>64</sup> The follow-up sample-return mission *Hayabusa-2* using also four  $\mu 10$  ion thrusters started in 2014 to the asteroid *Ryugu* where it arrived in 2018.<sup>65</sup> Furthermore, the combined ESA/JAXA spacecraft *Bepi-Colombo* launched in 2018 and heading currently toward Mercury is equipped with a solar EP system consisting of four Kaufman type thrusters (T6 from QinetiQ) as the main spacecraft propulsion system.<sup>66–68</sup> In contrast to the GOCE mission, where the satellite was permanently exposed to a frictional force with the residual atmosphere, which had to be compensated, the ion thrusters on *Bepi-Colombo* will not run continuously but only during certain travel segments between the nine planned swing-by maneuvers.

Finally, future formation flights where the positions of the spacecrafts involved have to be controlled very precisely will be an interesting application of EP. Such a mission will be *LISA* (Laser Interferometer Space Antenna) where three satellites will fly in an triangular formation around the sun with distances of  $2.5 \times 10^6$  km between them for detecting gravitational waves at frequencies of less than 1 Hz.<sup>69</sup> The frequency range to be covered by *LISA* lies between  $10^{-4}$  Hz and  $10^{-1}$  Hz and is thus outside the frequency range of terrestrial interferometric measuring systems covering the high-frequency range ( $>1$  Hz), which have already recently been able to achieve groundbreaking results through direct detection of gravitational waves.<sup>70</sup> Perturbations due to the gravitational forces of other planets and the light pressure from sun have to be compensated precisely using this antenna approach in space. In the technology-demonstrating mission *LISA Pathfinder* by ESA, launched in 2015, cold gas and colloidal thrusters using cesium with thrusts between  $0.1 \mu\text{N}$  and  $150 \mu\text{N}$  have been tested successfully.<sup>71</sup> NGGM (Next Generation Gravity Mission) is an ESA mission that has been in the preparatory phase since about 2003 and is a continuation of GOCE. The goal is the time-resolved measurement of the Earth's gravitational field with high spatial resolution over a period of about 11 years, covering one solar cycle.<sup>72</sup> The method used is low-low satellite tracking (LLST), i.e., a method of formation flight of at least two satellites both in LEO, which are driven by ion engines. In particular, information on the melting of ice layers, variations in sea level and groundwater reserves, and post-seismic changes will be obtained. Two propulsion topologies have been identified as suitable candidates: on the one hand, a topology comprising engines of two different sizes, one for the compensation of air friction and the other for the other control functions. On the other hand, a topology employing engines of the same size for all control functions. The topology used will largely depend on the working flight altitude, on the number and orientation of the engines, and on the type of LLST formation flight. A potential candidate for the small engines of mixed topology is miniaturized RF engines.<sup>73,74</sup> Current research activities are addressing the interaction of several engines regarding their electromagnetic compatibility in cluster operation.

### C. Commercialization of EP and challenges

A main handle in successful commercialization of any kind of space technology and, thus, also of propulsion systems is simply mass reduction.<sup>75</sup> A reduction in mass means lower launch costs and a greater flexibility in choosing an appropriate launch system. Both aspects are therefore decisive from an economic point of view. Electric propulsion offers this advantage and has become more and more accepted compared to classical, i.e., chemical, systems. The commercialization of EP began in 1982 with the use of resistojets for GSO NSSK on the telecommunications satellite *Intelsat-V*. Initially, electrothermal propulsion systems (resistojets and arcjets) dominated the EP sector, but they were increasingly replaced by HETs from the mid-1990s onwards.<sup>46</sup> Out of the numerous EP systems, two types of EP thrusters have proven to be particularly suitable in terms of their characteristics: the HETs and the GIEs.<sup>6</sup> While the former are particularly suitable for classical tasks such as orbital maintenance due to their high power-to-thrust efficiency, the GIEs are suitable for long term missions due to their higher Isp, which enables longer operating times based on the same amount of propellant, e.g., in the context of the GOCE- and the *BepiColombo* mission.<sup>57,66</sup> HETs deliver thruster-to-power ratios in the order of  $60 \text{ mN/kW}$  with a thrust density of about  $30 \text{ N/m}^2$ , while GIEs deliver only  $30 \text{ mN/kW}$  and  $5 \text{ N/m}^2$ , respectively.<sup>76</sup> On the other hand, GIEs provide a certain flexibility and can switch between the high-thrust/low-Isp mode and the low-thrust/high-Isp mode so that they can be used for EOR in the high thrust mode and for station keeping (after reaching the targeted orbit) in the high Isp-mode. Launching a satellite by combining the use of a chemical rocket up to a low orbit and EOR to the final orbit saves a significant amount of chemical propellant and thus launch mass, compared to a launch to the final orbit employing a chemical rocket only. The resulting reduction in launch costs can be up to 40%. As an example, a spiral rise from GTO to GSO of a satellite was calculated with the help of the open source software GMAT (*General Mission Analysis Tool*) provided by NASA [cf. Figs. 1(c) and 1(d)]. The time needed for spiraling up depends on the available thrust of the engines and their Isp value and is in the order of several months. HETs have a slight time advantage over GIEs in that they take slightly less time to spiral up, but this is at the expense of the amount of propellant needed. Thrusts of 0.5 N and 1 N were assumed in the GMAT calculation. Such thrust values may be achieved by operation of a thruster cluster consisting of two or more large thrusters. Operating a cluster can be challenging also from the electrical performance point of view, for instance, due to electromagnetic compatibility issues, which are discussed in detail in Sec. IV H.

Employing EP for all relevant maneuvers in space due to its low propellant consumption, significant launch mass reduction, and extended operational time is the obvious conclusion and common practice for at least two decades now. Boeing pioneered in this field with its 702 satellite bus using four onboard xenon ion propulsion systems (XIPSS) and providing the first all-electric satellite system for NSSK.<sup>77</sup> Since there has been no market interest in large and therefore expensive satellites that operate exclusively with EP, i.e., also reach their target orbit with EOR, Boeing introduced its 702SP (small platform) satellite bus in 2012. The 702SP is able to perform all relevant maneuvers, especially EOR, with EP in space. This results in a dry matter content of about 80% compared to conventional

platforms whose payload share is only about 40%–60%.<sup>78</sup> This concept has been accepted by the market and has led to a number of orders of this platform and corresponding missions in space, for instance, the ABS-3A and Eutelsat 115 West B satellites launched in March 2015, in a stacked configuration on a Falcon 9. Other market players have followed this approach and are developing all EP systems themselves. In Europe, the trend is driven by the Electra program, which is a public–private partnership between ESA, SES, and OHB for developing small to medium sized full EP satellite platforms.<sup>79</sup>

In addition to these two main propulsion systems (HET and GIE), there are a number of new propulsion concepts that currently are entering the market. These novel thruster types are often tailored to the needs of smaller satellite systems (CubeSats and small satellites for constellations). Furthermore, there are new mission scenarios, e.g., the megaconstellations, in which a very large number of small satellites operate in a network.<sup>80</sup> An example is the OneWeb project, a constellation of about 720 satellites in LEO to provide global broadband internet access. Similar projects with similar objectives are also planned by SpaceX (Starlink project) and Amazon (Kuiper project). All these satellites will have electric thrusters for attitude and altitude control. For Starlink, the planned number of satellites is in the order of about 40 000 (in the final phase of the project; according to Portillo, permits for 4425 SpaceX satellites have been applied for with the Federal Communications Commission so far), and for Kuiper, about 3000 satellites are to be deployed.<sup>81</sup> Currently (as of December 2019), about 76 satellites are already in orbit as part of OneWeb and StarLink [cf. Fig. 3(a)].

With this large number of satellites in LEO, aspects of the avoidance of space debris or the assessment of risks of potential satellite collisions must also be considered.<sup>83</sup> Recent studies estimated a high probability of at least one satellite collision during 5 years of operation (5% for OneWeb and 45.8% for SpaceX).<sup>84</sup> Recent studies also imply that the risk for collisions in GEO is significantly higher than previous findings have claimed. Accordingly, a collision of a satellite in GEO with a 1 cm object is likely to occur every 4 years.<sup>85</sup> Already now, a number of about 19 000 possible collision partners are monitored [cf. Fig. 3(c)] with the total mass of electronic waste amounting to about 7700 tons. Space debris poses a risk in that, according to Kessler, a tipping point might exist from which a chain reaction of collision processes between debris particles is likely to occur, leading to an associated exponential growth in particle density.<sup>86,87</sup> This tipping point is defined by a critical population density of scrap particles. There are a number of approaches to get rid of space debris, but none has been successfully implemented yet.<sup>88</sup> One approach is the use of the ion beam of an EP system to send a disused satellite into a so-called graveyard orbit by means of momentum transfer, also known as the ion-beam shepherd (IBS) concept [cf. Fig. 3(b)].<sup>89–91</sup> The IBS concept is often referred to as a contactless debris removal method. However, this term is somewhat misleading because there is a contact between the thruster plume and the debris object. The bombardment of a debris object with ions leads to sputtering processes. Sputtering takes place on the atomic level (see Sec. IV J). However, it cannot be ruled out that larger fragments of the debris object may be broken off in the process, which can then become dangerous as collision partners and may

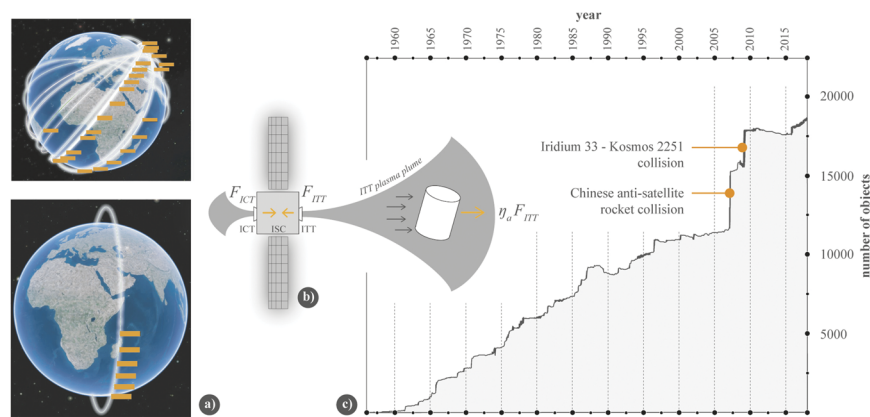


**FIG. 3.** (a) Satellite orbits (as of December 2019) of the OneWeb (6 in total) and Starlink project satellites in orbit (122 in total, 3 of which are out of service). OneWeb plans a Ku + Ka band constellation of 720 satellites in 18 circular orbital planes at an altitude of 1200 km. Starlink is also planned as a Ku + Ka band constellation, here with 4425 satellites. The orbital planes are more complex, the first 1600 satellites will be distributed evenly over 32 orbits, and the flight altitude will be 1150 km. In a second wave, 2825 satellites will be distributed at slightly different altitudes (data and further information can be found in Ref. 81 and the references therein). As of April 1, 2020, OneWeb has launched 34 more satellites, and Starlink has launched 240 more satellites. The images were created using the online tool of the *Celestrak Orbit Visualization* website. (b) Concept of space debris removal employing the ion beam shepherd (IBS) concept.<sup>82</sup> The debris object will be pushed out of its orbit by momentum transfer from impinging ions generated in an ion thruster of an external satellite. The thrust of the ITT (impulse transfer thruster) has to be compensated with an additional thruster (ICT, impulse compensation thruster) to keep a fixed distance between the satellite and the debris object. (c) Number of trackable objects in orbit. Data taken from Orbital Debris Quarterly News (NASA), Vol. 22, Issue 1, February 2018. The graphs include all objects that have been officially cataloged by the U.S. Space Surveillance Network. Also included are two relevant recent collisions. On January 11, 2007, China deliberately destroyed one of its weather satellites with a projectile of unknown design, resulting in the largest increase in space debris particles to date. About two years later, on February 10, 2009, the first collision of two communications satellites [Iridium (US) and Kosmos (Russia)] occurred, also with a significant increase in the number of scrap particles.



even be that small that tracking from the Earth's surface will not be possible. The literature on the IBS concept mainly deals with the influence of the sputter products on the performance of the impulse transfer engine.<sup>92</sup> So far, a risk assessment considering the formation of larger fragments has not been performed. Nevertheless, the IBS method has its advantages because it does not require complicated docking maneuvers and will be applicable, if the amount of larger fragments released by sputtering processes is sufficiently low or can be entirely avoided.<sup>93</sup> A risk assessment of IBS can be performed by modeling the sputter interaction between ion beam and space debris. Details on modeling can be found in Sec. IV D, and further information on sputtering is given in Sec. IV J. The IBS method is even considered a potential method to deflect larger asteroids, which are on collision course with Earth.<sup>94</sup> Due to the low momentum transfer, however, this method will be very time consuming, bombardment times for a significant change of course, especially in the case of larger asteroids, will be in the range of several years.

EP systems will have to be produced in large quantities to meet the great demand, e.g., for mega-constellations. The competition will get tougher as many small spin-offs with successful products will enter the market (ENPULSION, ExoTrail, AvantSpace, etc.). Despite this commercialization, EP systems are still the subject of extensive research, even on a fundamental basis.<sup>95</sup> The reasons are manifold:

- (i) EP systems are only partially scalable. Typically, the efficiency decreases significantly with smaller size so that new concepts may have to be used in the long run, when miniaturizing EP systems further. Currently, most of the new concepts are still at a low level of technological maturity. This has consequences, especially for CubeSats and other small satellites, which have very low electrical power reserves and cannot be operated with conventional engines. On the other hand, there is a need for high power engines with a long lifetime used for larger spacecrafts and interplanetary missions. This places enormous demands on the vacuum facilities needed for testing and qualification in terms of size and pumping speed and also on the available peripheral technologies such as high-performance power supply units as well as on an efficient temperature management, since unavoidable power losses in high power engines can lead to significantly higher undesired heating of the EP system.
- (ii) All types of EP systems require specialized electronics for driving them. Design of such space electronics is governed by other requirements than that of electronics for terrestrial applications. Space electronics is restricted in electric power budget and must be particularly efficient to avoid Joule heating. Furthermore, the high demands placed on space electronics require extensive development and testing. Consequently, space electronics components are among the most expensive components of EP systems. It therefore makes sense to strive for modularization here, which makes it possible to supply a larger number of engines with a smaller number of standardized modular electronic components.
- (iii) During the spiraling from the GTO to target orbit, which, using EP, takes a long time depending on the available thrust, the satellite has to cross the Van Allen belts where it is permanently exposed to hard radiation. This radiation may damage

- the satellite's electronics, so all electrical components must be built radiation-hard and tested accordingly in the laboratory.
- (iv) Electrical components of ion thrusters and the thrusters themselves are sources and sinks of electromagnetic radiation that can interact with other electronics of the satellite. In order to rule out any danger to the satellite, ion thrusters must be tested with respect to their electromagnetic compatibility (EMC). Since these engines only function under vacuum conditions, special requirements for the test environment have to be met in order to ensure that the measurements comply with existing standards.
- (v) Ion engines use the noble gas xenon as the propellant. According to the German Federal Institute for Geosciences and Natural Resources, the annual production in 2017 was about 72 tons (12 200 m<sup>3</sup>) of xenon. In view of the increasing demand for space travel, this quantity will not be sufficient or will drive the price up. Currently, there are about 63 plants worldwide with xenon production capacities and about 21 sites for xenon purification.<sup>96</sup> Even additional plants will hardly cover the demand. The mass fraction of xenon in air is 400 ppb. If 1000 tons of air were liquefied, only 400 g xenon may be produced (at 100% efficiency). The search for readily available, efficient, and cost-effective alternatives to xenon has therefore become of fundamental research interest in the EP area.
- (vi) A neutralizer is an elementary component of any EP system. It supplies an electron current equivalent to the positive ion current to prevent the satellite from being charged. The most common implementation is the hollow cathode, equipped with a so-called insert material, which has a low electron work function. Unfortunately, despite the already quite low work function of about 1.6 eV–2.8 eV, high temperatures are required to ensure sufficient thermionic emission, typically 1000 °C and higher. These high temperatures are technically challenging. Neutralizers are among the most failure-prone components of EP systems, mainly due to the high thermal loads. The search for novel materials with even lower work functions and the development of EP approaches with inherent neutralization are constant research themes here.

As can be seen, there are a number of aspects that illustrate that there are still a variety of unresolved issues in the field of EP. The field is also interesting in that it links a large number of different areas and is truly interdisciplinary. The plasma needs atomic physical quantities (excitation and ionization cross sections) in order to be described sufficiently accurately by global rate models or particle-in-cell (PIC) methods. Alternative propellants on a molecular basis can be analyzed in terms of their suitability by means of various analytical methods, such as time-of-flight mass spectrometry. In the case of reactive alternatives such as iodine, chemical material interactions must be taken into account that do not occur in the case of the noble gas xenon currently used. Material aspects also play an important role in the field of neutralizer development and also for the development of radiation-hard electronics. Electrical engineering plays a major role in the investigation of EMC aspects. This interplay of physics, chemistry, electrical engineering, and materials science ensures that electric space propulsion systems are constantly evolving.

One may say that EP is nowadays commercialized. At least in the case of megaconstellations for LEO, the propulsion systems will become mass products. The transition from a niche technology to a technology employed in large numbers requires rethinking in terms of production costs (e.g., using components off-the-shelf) and resources (e.g., availability of Xe as a propellant) as well as in terms of time to market of EP products (i.e., shorter and cheaper qualification for space). These challenges also concern the aspect of standardization of test systems, diagnostic procedures, and their analysis. They will be considered in the discussion of these topics.

### III. SPACE PROPULSION SYSTEMS

#### A. Thruster types

Electric space engines have evolved out of their shadowy existence due to the abovementioned strong points.<sup>97–101</sup> There are a

large number of different types of EP systems, some still at a conceptual level, others already at a very high technological maturity level, and a few already in use in space (cf. Fig. 4). These different propulsion systems have often been developed for special mission scenarios or maneuvers. Nevertheless, three main types of thrusters can be distinguished:

#### 1. Electrothermal thrusters

The gaseous propellant is heated electrically, and the thrust is generated by thermodynamical expansion of the propellant with the help of a nozzle. Thrusters of this type are simple in design; however, they do not provide high exhaust velocities of the propellant. Classical electrothermal thrusters are the resistojet and the arcjet [see Figs. 4(a) and 4(b)]. The resistojet increases the exhaust velocity simply by heating the propellant through an electric heater element based on Ohmic heating. In the arcjet, the propellant is passed through an arc discharge. Collisions between propellant

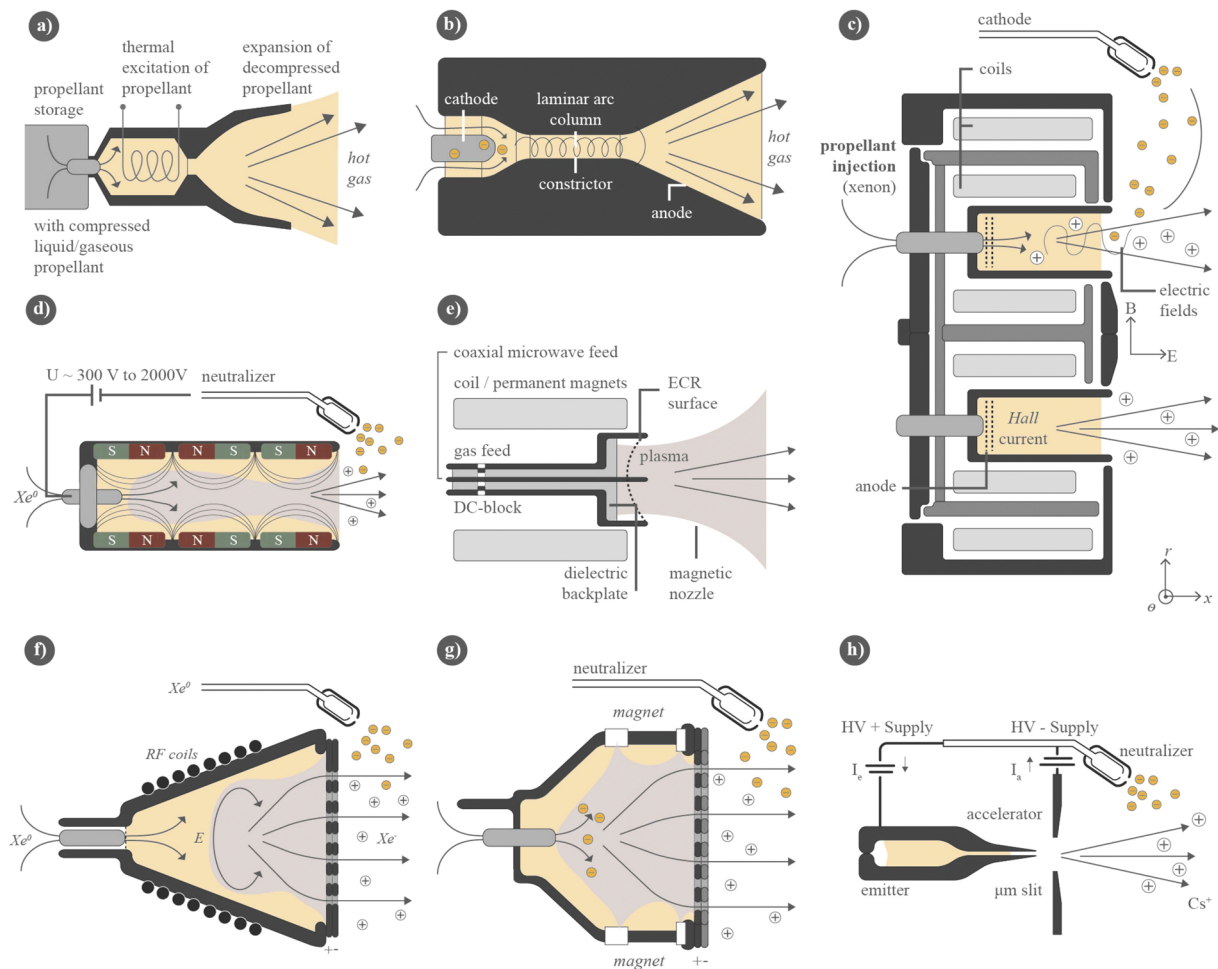


**FIG. 4.** Schematic drawings of the main EP systems: (a) resistojet, (b) arcjet, (c) Hall thruster, (d) HEMP thruster, (e) ECR thruster, (f) radiofrequency ion thruster, (g) electron bombardment thruster, and (h) FEEP.

and discharge particles heat the propellant, yielding higher exhaust velocity.

## 2. Electrostatic thrusters

The generation of thrust is concatenated by electrostatic field acceleration of the charged ion. Typically, the ionization of the propellant and the acceleration can be regarded as two separate processes, i.e., a two-step process. In the case of GIEs [Figs. 4(f) and 4(g)], the two steps can be directly assigned to the spatial segments of the thrusters. The plasma is generated from the propellant in the discharge vessel, and ions are extracted from the plasma by means of the grid system. In a HET [Fig. 4(c)] or a high efficiency multistage plasma thruster (HEMPT) [Fig. 4(d)], a crossed electric and magnetic force is used to generate a plasma discharge from the propellant, whereby the acceleration of ions occurs in the electric field. We would like to emphasize that some authors assign the HET to the class of electromagnetic thrusters due to the primal thrust transfer mechanism, which results in a thrust  $\vec{T}$  given by  $\vec{T} = \vec{J}_{Hall} \times \vec{B}$ , where  $\vec{J}_{Hall}$  is the Hall current and  $\vec{B}$  is the magnetic field strength induced by the magnets of the HET. Nevertheless, we follow the classification given by Goebel and Katz, who stress the electromagnetic acceleration of the ions.<sup>6</sup> The discharge takes place in an one-side open channel (linear for HEMPT and cylindrical for HET), in which the anode and the propellant inlet are located at the bottom end. Electrons from the neutralizer cathode are attracted by the anode potential, ignite the plasma, and sustain the discharge inside this channel. The plasma is positively biased by the anode voltage, which defines (neglecting the offset by the employed plasma potential) the ion energy. The acceleration takes place in a region close to the exit plane of the discharge channel, which is characterized by a potential drop occurring from the neutralizer's electrons, establishing a virtual cathode in front of the channel. We have subsumed HETs and high efficiency multistage plasma thrusters (HEMPTs) under this thruster class due to the underlying physical processes and their similarity.<sup>102</sup> Both, HET and HEMPT, exploit a crossed electric and magnetic field topology to generate Hall current loops for the electrons within the discharge region, providing a highly efficient ionization of the propellant. The main difference between the HET and the HEMPT is the periodic magnetic cusp field of the HEMPT, which enhances the plasma confinement in the discharge channel. As a consequence, HEMPTs provide higher plasma thrust densities and less channel erosion than HETs.<sup>103</sup> The operation principle of colloid emitters or FEEPs [Fig. 4(h)] is based on the formation and extraction of a beam of charged droplets or ions from a liquid propellant by the applied electrostatic field.

## 3. Electromagnetic thrusters

Permanent magnets are used to generate the static magnetic field in the case of a HET and of a HEMPT. In contrast, the magnetic field of a pulsed plasma thruster (PPT) is generated by the (arc) discharge itself, resulting in an accelerating  $\vec{j} \times \vec{B}$  Lorentz force. Therefore, ionization and acceleration cannot be regarded as separate processes. Another variant is the magnetoplasma dynamic thrusters (MPDTs). MPDTs can be interpreted as a powerful variant of an arcjet, in which the arc discharge is of such an intensity that the propellant is not just heated thermally but also is

ionized to a high degree and accelerated by the electromagnetic fields associated with the discharge. It can therefore be concluded that MPDTs only perform efficiently at relatively high electrical power levels; otherwise, the electromagnetic fields, which are generated by the arc, are not sufficiently intense to accelerate the propellant. Applied field MPDs (AF-MPDs) provide an external magnetic field to increase the efficiency of the thruster. Engines without assisting magnetic fields are named self-field MPD (SF-MPD). We also assign the electrodeless magnetic nozzle ECR thruster [see Fig. 4(e)] to this thruster type due to the lack of accelerating electrodes. Therefore, the generation of thrust of this engine is caused by a complex interplay of processes inside the plasma, resulting in an acceleration of the plasma by ambipolar fields, which is until now not entirely understood.<sup>104</sup>

We do not provide a detailed description of all individual thruster types here and refer the reader—to beside the already mentioned—to other relevant literature.<sup>41,105–112</sup> All three main thruster types have in common that electrical energy is converted into kinetic energy of the exhausted particles to generate or increase thrust. This energy conversion process differs in efficiency for the three types and is also very different in terms of the complexity of the technical implementation. For an overview, important thruster parameters are summarized in Table II.

Additional relevant parameters to describe EP systems are defined in Sec. III B, and details about GIEs are provided in Sec. III C. A special type of thruster based on the ECR principle is presented in Sec. IV C.

## B. Basics of electric propulsion

Under the assumption that EP systems can provide the necessary thrust in a mission scenario, two criteria are ultimately decisive for the selection of the appropriate engine type. The first criterion is the electrical power available on the satellite and thus the thrust-to-power ratio of the propulsion system. Higher thrust with the same power means faster travel in space, and thus, this key parameter correlates with time efficiency. The second criterion is the specific impulse Isp of the propulsion system. The specific impulse is the achievable change in momentum  $\Delta p$  per ejected mass  $\Delta m$ . This can be extended (in infinitesimal form) to

$$I_{sp} = \frac{dp}{dm} = \frac{T}{\dot{m}} = v_{ex}. \quad (4)$$

The Isp corresponds to the generated thrust per temporal mass output and is equivalent to the velocity  $v_{ex}$  of exhausted particles. Usually, this expression is divided by the gravitational acceleration  $g = 9.807 \text{ m/s}^2$ . This gives the Isp the unit second, which is used in all unit systems. Sources of error due to different unit systems, whereby satellites have already been damaged, for example, the loss of the Mars Climate Orbiter, are excluded by this definition of the specific momentum.<sup>119</sup> Since the thrust  $T$  is defined as  $v_{ex}\dot{m}$ , the Isp in this notation corresponds to the exhaust velocity of the propellant divided by the gravitational acceleration. The discussion about the usefulness of referencing the specific impulse to the weight of the emitted propellant seems to be an ongoing matter of dispute in rocket science. We refer the interested reader to Refs. 120 and 121 where this somehow diverting topic is discussed in more detail.

**TABLE II.** Characteristics of main EP thruster types. Data taken from Refs. 6, 36, 68, 105, and 113–118. For reasons of clarity, we have combined the HET and HEMPT as well as MPDT and ECR into one class, since they exhibit similar performances. It should also be mentioned that there are mixed versions of these engines, e.g., a GIE can be based on a plasma generation using the ECR principle. In the case of the ECR engine listed here, we refer to an electrodeless variant, as described in Sec. IV C. The specified parameters are not limited to thrusters with flight heritage. The given ranges of parameters can therefore be much wider than typical flight parameters would suggest. The electrical efficiency  $\eta_e$  of the thrusters is defined by Eq. (9).

	Resistojet	Arcjet	GIE	HET/HEMPT	PPT	MPDT/ECR
Type	Electrothermal	Electrothermal	Electrostatic	Electrostatic	Electromagnetic	Electromagnetic
Achievable thrust (mN)	0.5–6000	50–6800	0.01–750	0.01–2000	0.05–10	0.001–2000
Isp (s)	150–850	130–2200	1 500–10 000	600–3000	1400–2700	200–3200
Efficiency $\eta_e$ (%)	30–110 <sup>a)</sup>	25–60	30–90	20–70	5–30	20–70 <sup>b)</sup>
Thrust-to-power ratio (mN/kW)	450–700	150–600	20–250	150–300	50–200	150–500
Operational time	Month	Month	Years	Month	Years	Weeks
Propellants	NH <sub>3</sub> , hydrazine, H <sub>2</sub> , Xe, and N <sub>2</sub>	H <sub>2</sub> , N <sub>2</sub> , hydrazine, and NH <sub>3</sub>	Xe, Kr, Ar, Bi, I <sub>2</sub> , and H <sub>2</sub> O	Xe, Kr, Ar, and I <sub>2</sub>	PTFE	Ar, Xe, H <sub>2</sub> , and Li
Benefit	Low level of complexity	High thrust	High Isp and high efficiency	High power-to-thrust-ratio	Simple device and solid propellant	High Isp and high thrust density
Drawback	Very low Isp	Low efficiency	Low thrust density and complex PPU	High beam divergence and channel erosion	Low efficiency	Low lifetime and high power requirement

<sup>a)</sup> Equation (9) does not take into account the contribution of chemical energy and cold-flow power to the increase in the specific impulse. Therefore, electrical efficiencies higher than 100% are achievable (cf. Ref. 105).

<sup>b)</sup> MPDT only.

High Isp values correspond to a high mass efficiency, i.e., less propellant is needed for the same thrust. However, these high values are typically accompanied by a higher electrical power input so that the thrust-to-power ratio usually decreases. The choice of the appropriate propulsion system is, therefore, always a trade-off between the available electrical power and the amount of propellant that can be transported. For high Isp-values, this power is mainly determined by the jet power  $P_{jet}$  of the exhausted ion beam given by

$$P_{jet} = \frac{1}{2} \dot{m} v_{ex}^2. \quad (5)$$

For the thrust, this results in the useful relationship

$$T = \frac{2P_{jet}}{I_{sp} \cdot g}. \quad (6)$$

In principle, all essential mission parameters concerning the EP system can be derived from Eq. (6). For example, increasing the thrust without changing the mass output  $\dot{m}$  leads to an increase in jet power. Assuming that a satellite with a dry mass of one ton and 500 kg propellant is sent out with a 20 kW engine with an Isp of 5000 s, a  $\Delta v$  of about 20.3 km/s can be achieved (with a corresponding thrust of about 0.8 N). This would allow a mission to the outer planets of the solar system. If one now wants to travel to more distant destinations, one could of course increase the amount of propellant, but due to the logarithmic dependence of  $\Delta v$  in the Tsiolkovsky equation, the increase in  $\Delta v$  is less than if one increased the actual Isp value [cf. Fig. 1(b)]. However, the jet power is linked to the Isp

by the relation  $P_{jet} \propto I_{sp}^2$ , so thrusters of a higher power class would have to be used. An increase in the Isp can be achieved, for example, with GIEs with 4-grid ion optics.<sup>122,123</sup>

A number of additional characteristic quantities are defined for ion thrusters. Since the thrust is mainly generated by the amount of exhausted ions  $\dot{m}_i$ , the introduction of a mass utilization efficiency  $\eta_m$ , i.e., the proportion of ions emitted in relation to the amount of propellant admitted  $\dot{m}_p$ , is reasonable,

$$\eta_m = \frac{\dot{m}_i}{\dot{m}_p}. \quad (7)$$

For singly charged ions and an atomic propellant, the following applies:

$$\eta_m = \frac{I_b}{e} \frac{M}{\dot{m}_p}, \quad (8)$$

where  $I_b$  stands for the exhausted ion beam current,  $M$  stands for the atomic mass, and  $e$  stands for the elementary charge. From the point of electrical efficiency, it makes sense to introduce the relation

$$\eta_e = \frac{P_{jet}}{P_T}, \quad (9)$$

i.e., the ratio of jet power  $P_{jet}$  and total input power  $P_T$  provided to the thruster. The total input power is made up of the jet power and the power  $P_d$  required for ion production. Figure 5 shows the thrust-to-power ratio as a function of Isp for various EP systems and their thrust efficiency according to Eq. (9). In ion thrusters, the ions are



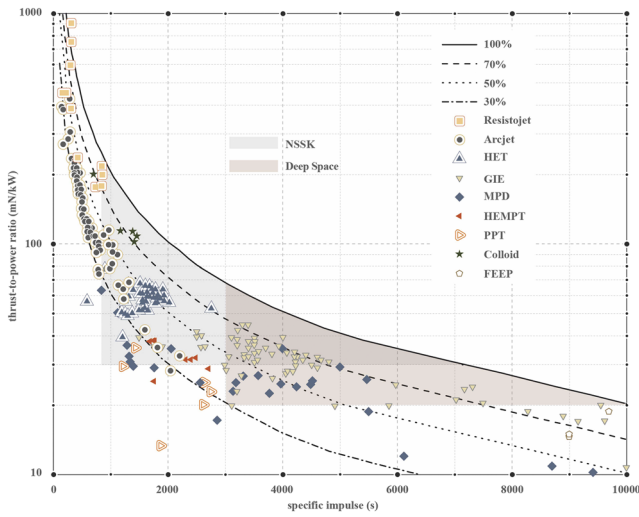


**FIG. 5.** Thrust-to-power ratio for various types of EP systems as a function of specific impulse (Isp). The lines define the thruster efficiency according to Eq. (9). The colored highlighted areas represent the operational range of EP systems for NSSK and DS missions. This figure shows that EP systems cover a very wide parameter range, i.e., they are suitable for very different mission requirements. High Isp values stand for applications that depend on high mass efficiency, while high thrust-to-power ratios are becoming increasingly important for time-critical missions. Data taken from Refs. 113 and 114.

accelerated by a voltage  $U$ . Therefore, the exhaust velocity is given by the relation

$$v_{\text{ex}}^2 = \frac{2eU}{M}. \quad (10)$$

Using this equation in Eq. (5), the jet power is simply given by the relation  $P_{\text{jet}} = UI_b$ . The ion production cost can be expressed as

$$\eta_d = \frac{P_d}{I_b} \quad (11)$$

and is typically given in eV per ion. The minimum ion production cost is given by the ionization threshold of the propellant. In ion thrusters, usually several hundreds of eV per ion are needed. If the contribution of expelled neutrals to the total thrust is neglected, the total thruster efficiency  $\eta_T$  is defined by Eq. (9). It is convenient to express the total efficiency by the thrust, the propellant mass flow, and the total input power,

$$\eta_T = \frac{T^2}{2\dot{m}_p P_{\text{in}}}. \quad (12)$$

Equation (12) allows a comparison of different thruster types, since significant differences in the characteristics of the thrusters, such as beam divergence, acceleration voltage, and influence of multiple-charged ions, are included in the parameters.

### C. Radio frequency ion thruster

The evolution of the RIT technology has gone always hand in hand with the development of plasma technology for processing

of materials, which requires robust ion sources for ion beam etching, sputtering, and related processes.<sup>124–126</sup> Löb finally regarded the rf technology in the 1960s as promising for EP systems for space travel and confirmed this in his pioneering work.<sup>30</sup> The thrusters are labeled RIT-3.5, RIT-4, etc. The number denotes the inner diameter of the cylindrical discharge vessel in cm. One can highlight three regions in the process of generating thrust from a neutral propellant gas, i.e., the ionization region, the ion acceleration region within the ion optics, and the neutralization region, where electrons for charge neutralization are provided by the neutralizer. The main components of the thruster are the discharge vessel surrounded by a coil, the grid system, and the gas injection system. These components are contained in a housing.

#### 1. Ionization region

The propellant is injected from the backside through a gas distributor, for instance, a porous ceramic interface. The porous ceramic prevents the plasma from igniting in the direction of the gas supply system and also acts as a particle filter. The coil is connected to a radio frequency generator (RFG) providing alternating voltages and currents, respectively, typically with a frequency in the range between 500 kHz and 5 MHz. The RFG sustains the plasma after ignition due to inductive coupling between the coil and the plasma. In an equivalent circuit diagram, the plasma can be regarded as a short-circuited ring coil with one winding. More details about RFGs and thruster electronics are given in Sec. IV G. Discharge vessels may have cylindrical, conical, or hemispherical shapes. The shape determines the degree of power loss due to the geometrical surface-to-volume ratio.

According to the Maxwell equation  $\nabla \times \vec{E} = -\frac{\partial \vec{B}}{\partial t}$ , the alternating magnetic field generates a time-varying rotating electric field within the coil volume, i.e., in the discharge vessel of the engine, which is given by

$$E_{\text{ind}}(r, t) = \frac{\mu_0}{2l_c} N_c \eta_c r \omega I_c e^{i\omega t}, \quad (13)$$

where  $N_c$  denotes the number of coil windings,  $l_c$  denotes the length of the coil,  $\eta_c$  denotes a correction factor for short coils,  $r$  denotes the radius of the discharge vessel relative to the symmetry axis of the thruster,  $\omega$  denotes the angular frequency of excitation, and  $I_c$  denotes the coil current. Typical coil currents are in the order of a few amperes, with the number of windings smaller than 10, and the electric field strengths calculated from Eq. (13) are usually in the range of a few V/cm. Within half a rf cycle, an electron cannot gain enough energy to reach the ionization threshold of, e.g., a xenon atom. Therefore, it must elastically collide with a xenon atom within this half cycle and change its direction so that it is further accelerated in the other direction in the second half of the cycle, where the field is of opposite sign. Hence, the neutral gas density must be adapted to the probability of collision with the electrons, which in turn depends on the frequency of the excitation current. This accumulation of energy leads to an almost stable thermalization of the electrons. Electron temperatures of the low-temperature plasma are typically in the order of a few electron volts. Representative for the orders of magnitude and the spatial distribution of the most important plasma parameters of a RIT, Figs. 6(a) and 6(b) show the results of radially resolved Langmuir measurements of electron

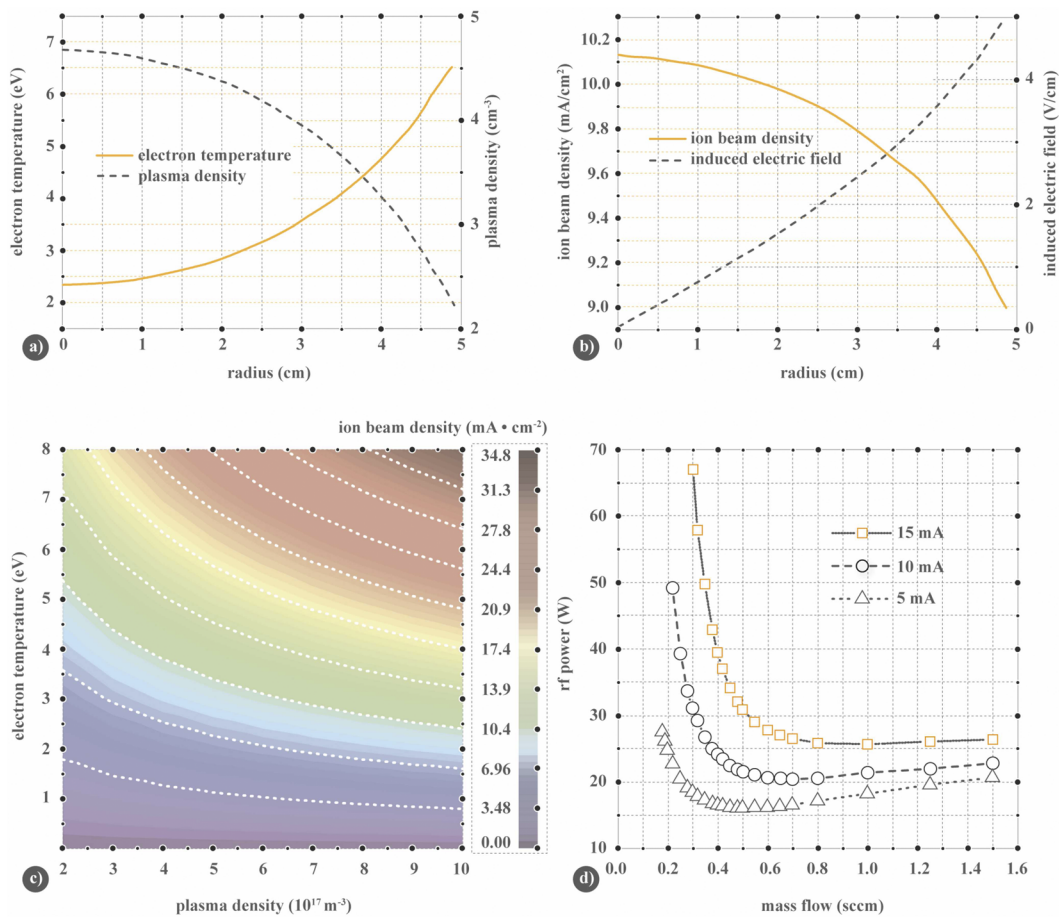


**FIG. 6.** (a) Radial distribution of electron temperature and plasma density and (b) ion beam density and induced electric field of a RIT-10. The data were obtained experimentally by means of double Langmuir probe measurements.<sup>127</sup> (c) Representation of the dependence of the ion current density  $j_{ion}$  on the density  $n$  of the plasma (related to the charged particles) and on the electron temperature  $T_e$  according to  $j_{ion} \propto n\sqrt{T_e}$ . (d) Performance mapping of a RIT-like 4 cm ion thruster developed at JLU using xenon as the propellant.

temperature, plasma density, ion current density, and induced electric field in a RIT-10.<sup>127</sup> Due to the inductive coupling, the induced electric field  $E_{ind}$  and as a result the electron temperature  $T_e$  have their maximum values at the wall of the discharge vessel, while due to ambipolar diffusion, the plasma density  $n$  decreases toward the walls. For the design of an engine, the following relationship can be assumed as the basis for a scaling of excitation frequency  $\nu$ , neutral pressure  $p$  inside the discharge vessel, and radius  $R$  of the discharge vessel (assumed to be cylindrical), starting from an already efficiently operating engine,

$$p \propto \nu \propto \frac{1}{R}. \quad (14)$$

This implies that for very small engines, it is necessary to increase the probability of collision with a propellant atom by increasing the neutral particle density; otherwise, electrons would recombine at the wall of the discharge vessel, i.e., increase in the neutral particle

density reduces the electron mean free path between collisions. The latter should be smaller than  $R$ . In addition to the unfavorable surface-to-volume ratio of the discharge vessel for small thrusters, this leads to a reduction in the mass efficiency and the specific impulse of the engine (for the same thrust). Further adjustments of the excitation frequency result from the matching/bridging network used, losses due to eddy currents, ohmic losses in the feeding line of the RFG, in the line between RFG and the coil as well as the coil itself, and other parasitic effects.

RF ion thrusters are usually characterized by so-called performance mappings. These are plots of the required DC power consumption of the RFG vs the mass flow admitted to the thruster for given constant ion beam current or thrust. These curves exhibit a characteristic shape, which is determined by the interplay of electron temperature, plasma density, and ion beam density. Figure 6(d) shows such a set of performance curves. Obviously, considering a curve for fixed thrust, the minimum of the curve stands for power

efficiency, whereas the lower values on the abscissa, i.e., small mass flows, where the RIT still operates, stands for mass efficiency. The power penalty to pay for mass efficiency can be very high, and a trade-off depending on the mission scenario is required here. If the mass flow is reduced starting from the point of optimum power efficiency, the neutral particle density decreases. As a result, fewer collision partners are available to the electrons and the energy accumulation through elastic collisions becomes inefficient. Although the electron temperature rises, the rate of ionizing collisions decreases, which lowers the plasma and the ion current density. To maintain a constant ion beam current, this decrease in ionization efficiency has to be compensated by an increased rf power. If the mass flow is increased starting from the point of optimum power efficiency, the electrons thermalize with the much colder neutral gas. The electron temperature decreases, whereas the plasma density increases accordingly to maintain the same current density. The relationship between electron temperature, plasma density, and beam current density is shown in Fig. 6(c). A performance mapping of a 4 cm rf-engine [shown in Fig. 6(d)] reflects this correlation of the three mentioned quantities under consideration and specific properties of the measured engine (design parameters, loss mechanisms, etc.).

## 2. Acceleration region

Ions from the engine can be accelerated by the grid system that is in direct contact with the plasma. The grid system acts as ion optics to ensure high directionality of the extracted beam. Furthermore, the thrust is generated within the grid system due to the counterforce between ions and the net field between the grids. The screen grid adjacent to the plasma is typically on a positive potential in the range of 1 kV–1.5 kV. This potential defines the reference potential of the plasma by direct contact, except for an offset due to the plasma and floating potential. The second grid (acceleration grid), which is typically at a negative potential, accelerates ions emerging from the plasma. The interplay of these two potentials with the plasma parameters defines the shape of the plasma meniscus, which determines the shape of the beamlet. The third (optional) grid defines a zero point potential. In two-grid systems, it may be replaced by a ring electrode or by a virtual cathode defined by the electron emission from the neutralizer. The maximum achievable ion current density  $j_{\max}$  in gridded ion thrusters is limited by the space charge between the screen and the acceleration grid and is described by the Child–Langmuir law,

$$j_{\max} = \frac{4\epsilon_0}{9} \sqrt{\frac{2e}{M}} \frac{U^{3/2}}{d^2}, \quad (15)$$

where  $M$  is the mass of the ion,  $U$  is the net extracting voltage (potential difference between the screen and the acceleration grid), and  $d$  is the effective distance between the acceleration grid and the plasma meniscus. For the ion yield of the plasma, in addition to the space-charge limitation, the relationship

$$j_{\text{ion}} = e^{-0.5} \cdot n_0 e \cdot \sqrt{\frac{k_B \cdot T_e}{m_i}} \quad (16)$$

has to be taken into account. Equation (16) is derived from  $j_{\text{ion}} = nev$ , assuming that  $T_{\text{ion}}/T_e \ll 1$  (cold plasma), and

consequently, the Bohm velocity  $v_B$  can be simplified to

$$v_B \approx \sqrt{\frac{k_B T_e}{M}}. \quad (17)$$

In particular, the pre-factor,  $\exp(-1/2) \approx 0.61$  for a cold plasma, in Eq. (16) will vary for different regimes, i.e., it depends on the assumptions made about the plasma density  $n$  contributing to  $j_{\text{ion}} = qnv$ . The interested reader is referred to Ref. 128 and the references therein.

The grid system is one of the critical components of this type of thruster and must meet a variety of requirements, such as low material erosion on ion impact, precisely defined thermal properties, good machinability, and high manufacturing precision.<sup>129</sup> These requirements have to be implemented for a long lifetime of the grid system. The lifetime of GIE is mainly determined by the erosion of the grid system. Although it is difficult to make general statements about the properties of many different types of HETs and GIEs, a few numbers are worth mentioning. Typically, the lifetime of a HET is in the order of 10 000 h.<sup>6,130</sup> During the same period of time, the erosion phenomena observed at the RITA, which was aboard the ARTEMIS satellite, showed a mean increase in the acceleration grid diameter of about 25%.<sup>131</sup> By definition, a structural defect of the RITA acceleration grid corresponds to an increase in aperture diameter of 75%. Results from a 15 000 h lifetime test and their extrapolation predicted a lifetime of the RITA grid system of more than 20 000 h.<sup>132</sup>

Optimization of ion optics was initially carried out with the aid of systematic experimental investigations in which grid voltages, spacings, thicknesses, and hole diameters were varied.<sup>133,134</sup> Calculations of the extraction process were initially possible using supercomputers only but are now feasible on personal computers due to their enormous increase in performance.<sup>135,136</sup> Details about the methods used to model the beam extraction can be found elsewhere.<sup>137</sup> Figure 7(a) shows exemplarily an ion beam extraction from a plasma via a grid system showing three beamlets. Figures 7(b) and 7(c) show the space charge distribution for a single beamlet with compensation and the shape of the plasma meniscus, respectively. The simulation has been carried out with KOBRA. Commercial tools such as IGUN (2D-code) and KOBRA (3D-code) as well as open source tools such as IBSIMU (3D-code) are available for simulating the extraction of the ion beam.<sup>138–140</sup> A comparison between IGUN and KOBRA was published by Hanke and co-workers.<sup>141</sup> Tartz and co-workers have combined the IGUN code with a charge-exchange model to simulate the grid erosion for determining the thruster's lifetime.<sup>142</sup> The code was validated for various gridded ion thrusters. When calculating the grid erosion, it is necessary to consider the charge-exchange (CEX) interaction between the extracted ion beam and the neutral gas particles. In the CEX process, a fast charged xenon ion, extracted from the plasma, and a thermal xenon atom exchange an electron in a collision. This recharged ion, due to its 'wrong' initial momentum, will follow a different trajectory through the ion optics than that designed for an ion entering the grid region from the plasma. Thus, it is likely that it will be accelerated toward the negatively biased acceleration grid in the electric field and sputter off material on impact [see also Fig. 7(c) where the region where CEX occurs within the grid system is highlighted]. Over time, this erosion increases the effective grid transparency of the ion optics



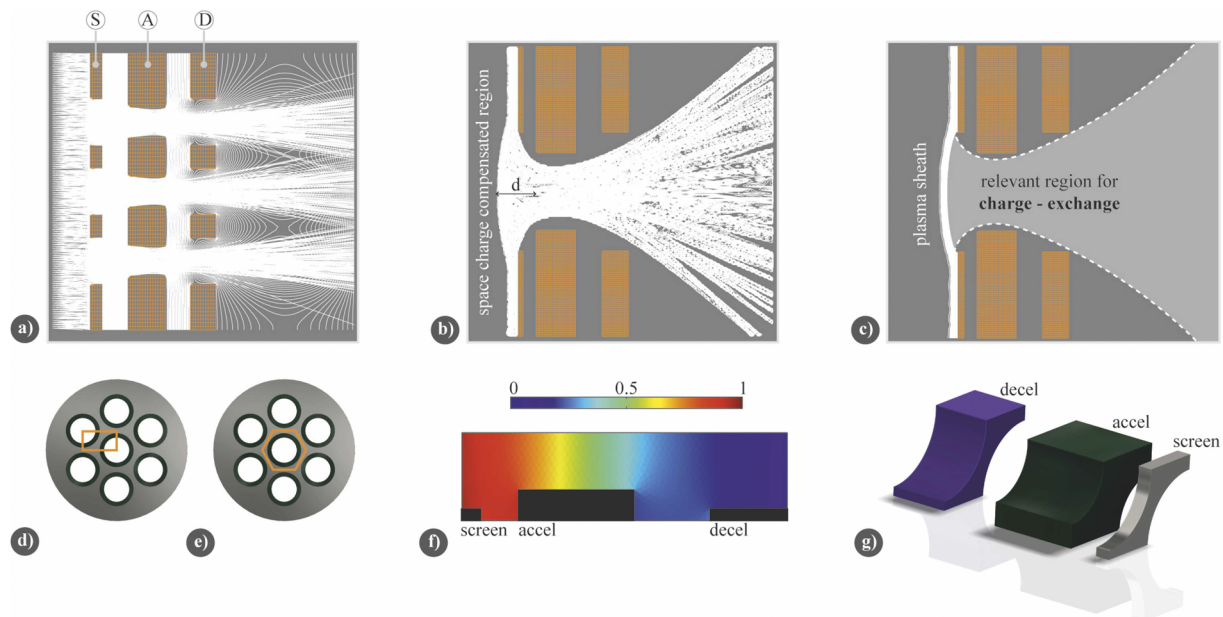


**FIG. 7.** Simulated ion beam extraction via an ion optical grid system that connects the plasma region and the region of the ion beam. Interaction forces between the extracted ions and the grids generate the thrust. Sophisticated 3D codes such as KOBRA used here make it possible to examine the interaction of the individual beamlets with each other. Furthermore, the influence of not optimally aligned grids on the beam extraction can be analyzed. (a) Simultaneous extraction of three beamlets to study beamlet–beamlet interaction. (b) Space charge distribution for one beamlet with compensation. (c) Potential drop between the plasma and the screen grid potential. The parameter  $d$  defines the effective distance between the curved plasma meniscus and the acceleration grid and is an input parameter in the Child–Langmuir law [see Eq. (15)]. Charge exchange (CEX) between xenon ions and neutrals within the extraction channel results in slow ions, which may be accelerated toward the negatively biased acceleration grid and may lead to grid erosion, limiting the lifetime of the ion thruster. CEX processes far downstream the extraction path may also lead to erosion, but due to the lower neutral density, this effect is less pronounced. In the case of a three-grid system, the deceleration grid will reduce this effect even further. However, due to the presence of a third grid, the neutral density at the acceleration grid is higher, which in turn may increase CEX losses. An advantageous representation of the simulation area in the case of a hexagonal arrangement of grid apertures for ion extraction is shown in (d). For the calculation of transmission coefficients for both neutral gas and ions, the corresponding non-transparent grid area required as reference for normalization is already taken into account. Furthermore, beamlet–beamlet interaction (BBI) is taken into account, which may have an influence on ion transparency. An equivalent representation (but without including BBI) is shown in (e). Both (d) and (e) are equivalent representations of a so-called unit cell for a hexagonal arrangement. (f) Calculated relative neutral particle density along a single extraction channel assuming free molecular flow. The density was calculated for the following parameters: screen diameter of 2 mm, screen thickness of 0.25 mm, screen-accel gap of 0.5 mm, accel diameter of 1.5 mm, accel thickness of 1.5 mm, accel-decel gap of 1 mm, decel diameter of 2 mm, and decel thickness of 1 mm. The result of the calculated transmission probability is 0.137. The calculation was performed using the angular coefficient method from the COMSOL MolecularFlow module. (g) shows the cut-out simulation area.

and leads to higher neutral gas losses, resulting in a degradation of the thruster's performance at the operating point of the engine. The CEX scales linearly with the neutral particle density and will accordingly be particularly pronounced in the extraction channels. Lingwei *et al.* have investigated the influence of the origin of CEX ions on grid erosion using an axially symmetric 2D code and emphasize the strong influence of CEX ions formed far downstream.<sup>143</sup> The influence of multiple colliding ions, which can account for about 7%–8% of the current on the acceleration grid, is investigated by Miyasaka *et al.* using a 3D-code. According to their analysis, these multiple impact processes should be considered for an accurate evaluation of the grid lifetime.<sup>144</sup> The contribution of doubly charged ions is also discussed on the basis of numerical calculations by Nakano. Especially for thrusters with a high proportion of doubly charged ions, these have to be accounted for in the calculations of grid erosion in order to obtain meaningful results.<sup>145</sup> The effect of a misalignment of the grids on beam extraction and grid erosion was discussed by Shagayda *et al.*<sup>146</sup> In order to calculate grid erosion, the neutral gas

density in the area of the extracted ion beam must first be known, especially in the area of the grid system, where the density is high. If the CEX cross section is also known, the number and places of birth of the secondary charged particles created, i.e., of the CEX ions, can be deduced. The program can generate them at the appropriate locations and then include them in the calculation of the beam trajectories. If these secondaries impinge on the grid material, the sputter removal can be derived by determining the number of particles hitting each grid element, their impact energy, and their impact angle. Knowing the sputter yield or the sputtering cross section of the grid material, the effects of the microscopic sputtering incidences can be added up until a mesoscopic grid element in the model is removed. Further details on sputtering and its relation to EP are given in Sec. IV J. Under certain circumstances, e.g., if an extraction channel is clearly eroded, a recalculation of the electric field distribution and the beam extraction may be necessary. In addition to the codes already mentioned, there are a number of validated in-house code developments of different research groups, for example,

the programs CEX2D or CEX3D of the Jet Propulsion Laboratory, the JIEDI tool of JAXA, and others.<sup>147–149</sup>

The neutral particle density within a channel, which has to be known for simulation of grid erosion, can be calculated using a number of available programs based, e.g., on the direct simulation Monte Carlo (DSMC) method (SPARTA, OpenFOAM) or others (COMSOL).<sup>150–152</sup> Figure 7 shows an example of a particle density calculated with COMSOL. A base pressure within the RIT discharge vessel of 0.15 Pa was assumed. The molecular flow is modeled by an angular coefficient method.<sup>153</sup> Such calculations provide the transmission probability of an incident gas particle through the grid system, the so-called Clausing factor  $\eta_{cl}$ , which is needed to calculate the neutral gas losses from the engine.<sup>154</sup> Assuming an optical grid transparency  $T_{opt}$ , the neutral particle flux  $Q_n$  through the grid system can be

calculated using

$$Q_n = \frac{1}{4} n v T_{opt} A_{grid} \eta_{cl}, \quad (18)$$

where  $A_{grid}$  is the surface area of the screen grid exposed to the plasma and  $v$  is the mean velocity of the neutrals. Similar to neutral particles, it is necessary to calculate the transparency of the grid system for ions. This can be done, for example, with the aforementioned ion beam extraction codes. It is useful to define a kind of unit cell for the typically hexagonally arranged apertures of the grid system in order to derive the correct ion current density within the simulated domain [cf. Figs. 7(e)–7(g)].

A number of approaches are available for modeling an entire RIT. Self-consistent models based on global (volume-averaged)

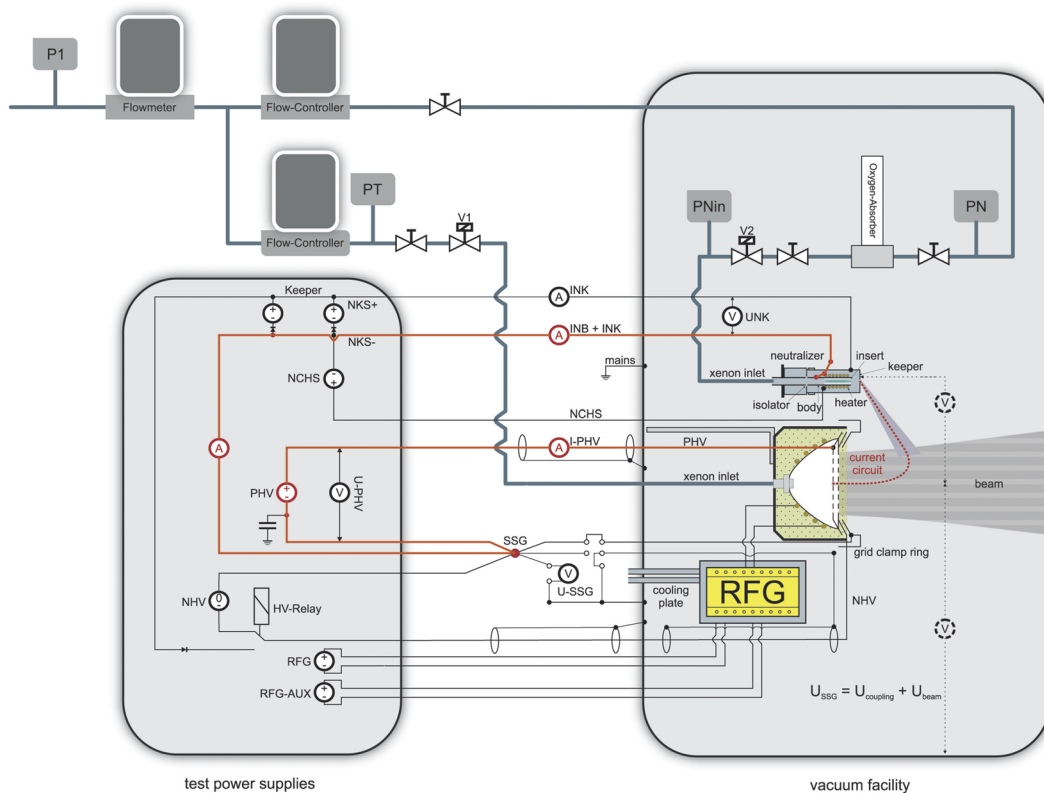


**FIG. 8.** Possible test scenario for the near-space operation of a rf driven gridded ion thruster with a neutralizer (without realistic imitation of mass flow control). The abbreviations stand for radio frequency generator (RFG), positive high voltage (PHV), negative high voltage (NHV), secondary star ground (SSG), auxiliary (AUX), neutralizer keeper power supply (NKS), neutralizer cathode heater power supply (NCHS), valve (V), pressure (P), neutralizer (N), and thruster (T). It should be mentioned that this scheme is not generally valid but has to be adapted to the electronic requirements of the hardware used. An important feature is the use of a potential reference decoupled from the ground potential, the SSG, to which all power supply units must refer. This makes it possible to close the electric circuit of the system consisting of the thruster and neutralizer via the plasma bridge (red wire path). With grounded power supplies, one would instead close the circuit via the vacuum tank and generate different operating conditions. For the ignition of the engine, the NHV grid is connected to the positive potential of the keeper. Due to the even more positive potential of the PHV, electrons from the neutralizer are accelerated toward the grid system, can enter the discharge chamber, and are accelerated there by the rf field, gaining enough energy to ionize propellant atoms and to ignite the plasma discharge of the thruster. After ignition, this connection is cut off by means of a HV relay and the NHV powering the acceleration grid. The mass flow control consists of commercially available mass flow controllers and meters. An oxygen absorber may be necessary to prevent poisoning of the neutralizer, especially when using BaO inserts. The manual valves upstream and downstream of the oxygen absorber have a protective function. They are only in use during the installation and deinstallation of the absorber and are closed then. Somewhat similar is the function of the V2 electric valve, it is required to prevent saturation of the oxygen absorber during venting of the vacuum system, which would make it non-operational. The valve V1 can optionally be used for controlled ignition via a pressure shock.

considerations offer a promising approach here. Fundamental considerations for the modeling of RF ion sources can be found in studies by Goebel.<sup>155–157</sup> An extended global model approach including power transfer from RFG to plasma and neutral gas heating but limited to cylindrical discharge vessel geometries was published by Chabert and co-workers.<sup>158</sup> For the simulation of the RIT as a complete unit including thermal modeling of the engine, commercial tools such as COMSOL can be employed, as shown by Dobkevicius and Feili, where beam extraction simulation was supported by IBSIMU.<sup>159</sup> Volkmar and Ricklefs introduced a self-consistent scripted code based on global model assumptions and providing performance data for RITs.<sup>160</sup> The code supports 3D coil geometries and has the advantage of low central processing unit (CPU) requirements. Reeh *et al.* have extended this code introducing an ion beam extraction module and a neutral gas transmission calculation.<sup>161</sup> Pham and Shin reported on a zero-dimensional model for rf ion thrusters including additional effects such as secondary electron emission at high temperature plasmas, the influence of double ionization, a variable Clausing factor, and an ion confinement factor due to the electromagnetic field of the coil, whereby the latter has the strongest effect on the calculations.<sup>162</sup> Henrich and Heiliger have developed a full 3D-PIC-DSMC code to simulate plasma properties of RITs, which is currently limited to small thruster geometries only due to the high demands on computing power. Nevertheless, it provides important information about the spatial distribution of plasma parameters.<sup>163</sup> How model descriptions on different length scales need to be combined to provide a predictive tool will be discussed in Sec. IV D.

In addition to the actual thruster body and neutralizer, the overall EP system includes a periphery of electrical and fluid supply systems, as exemplarily shown in Fig. 8. The circuit topology differs from the normal operation of an ion source, whose power supply is typically referenced to ground potential. In terrestrial testing, the satellite potential is simulated by introducing a reference potential decoupled from the earth potential, the secondary star ground (SSG).

### 3. Neutralization region

To ensure the electrical neutrality of the satellite or other spacecraft, the same amount of electrons than positively charged ions has to be expelled from the satellite. Typically, electrons are added to the positively charged ion beam. As already mentioned, this is done in EP systems with a neutralizer; typically, a hollow cathode is used. Neutralizers require additional electric and fluidic support lines. The operating principle of hollow cathodes is described in detail in the literature.<sup>6,38,164</sup> It is desirable that a neutralizer uses the same propellant as the thruster to prevent the need for another propellant reservoir. A discharge is ignited inside the hollow cathode coated with the insert material. The discharge is coupled with the ion beam of the thruster by the formation of a plasma bridge. The electrons extracted from the hollow cathode flow across the plasma bridge and neutralize the ion beam.

## IV. CHALLENGES

### A. Alternative propellants

Currently, ion thrusters are routinely propelled with the noble gas xenon, which replaced the previously used mercury. Xenon is

chemically inert, has a comparatively high mass, and is present in the gas phase under standard conditions. However, two decisive disadvantages have emerged: xenon is a rare resource and, accordingly, expensive. In addition, it must be stored in special pressure tanks on the satellite, which represents a potential risk for failures. In particular, in the case of small satellites, which often are brought into space as secondary payloads, the pressure tanks are undesirable not only because of their size but because of the additional risk they present to the primary payload.

Assessing whether a material is suitable as a propellant has become a rather complex task. The complexity is related to the transition of EP technology from a niche market item to a mass product. As a consequence, economic and environmental issues have to be treated on the same level as atomic or molecular properties. Studies of this kind have been performed for a number of atomic propellants.<sup>172,173</sup> Important properties that need to be considered in the case of atomic propellants are the atomic mass, the ionization energy, and the ionization cross section, and also the boiling point.<sup>174</sup> From the energetic point of view, the cross section for ionization plays an important role. Figure 9(a) shows the ionization cross sections for a number of materials that are of interest for EP. Xenon's ionization efficiency is in the upper range, and those of the other noble gases shown are significantly lower. The molecular propellant adamantane has by far the largest cross section of the examples shown. The large cross section is due to the size of the molecule. However, molecular propellants exhibit more possible loss mechanisms than their atomic competitors, such as dissociation of the molecule into lighter fragments and the excitation of molecular vibrations. In addition to the actual size of the cross sections, the ionization threshold must also be included in the assessment. Here, the noble gases naturally perform worse, since the filled shell structure of the atoms proves to be particularly stable. Atoms that are close to the noble gas structure, such as the alkali metals or halogens, can be ionized at much lower electron energies, but these substances are, for the same reason, chemically very reactive, which can lead to undesired material interactions. In addition to these atomic physics considerations, technical aspects are important. As a rule, propellants must be available as a gas in order to be ionized inside the thruster. Here, the efficiency of the evaporation as well as the boiling temperature of the propellant plays a decisive role. Also important are possible loss mechanisms (electronic or molecular excitation processes, electron capture processes, etc.) and the density of the material. It may be advantageous to store the propellant in solid form, which makes a pressure tank unnecessary.

An alternative to xenon often discussed is krypton that is about ten times more abundant in the Earth's atmosphere. Its current price is about a tenth of that of xenon. From a physical point of view, it is necessary to increase the jet power, i.e., the electrical power required for generating the same thrust by extracting Kr ions instead of Xe ions, according to

$$P_{\text{Kr}} = P_{\text{Xe}} \cdot \sqrt{\frac{m_{\text{i,Xe}}}{m_{\text{i,Kr}}}} = 1.25 \cdot P_{\text{Xe}}. \quad (19)$$

In addition to this 25% increase in jet power required for the same thrust, there are other factors that need to be considered due to different ionization energies, excitation and ionization cross sections,

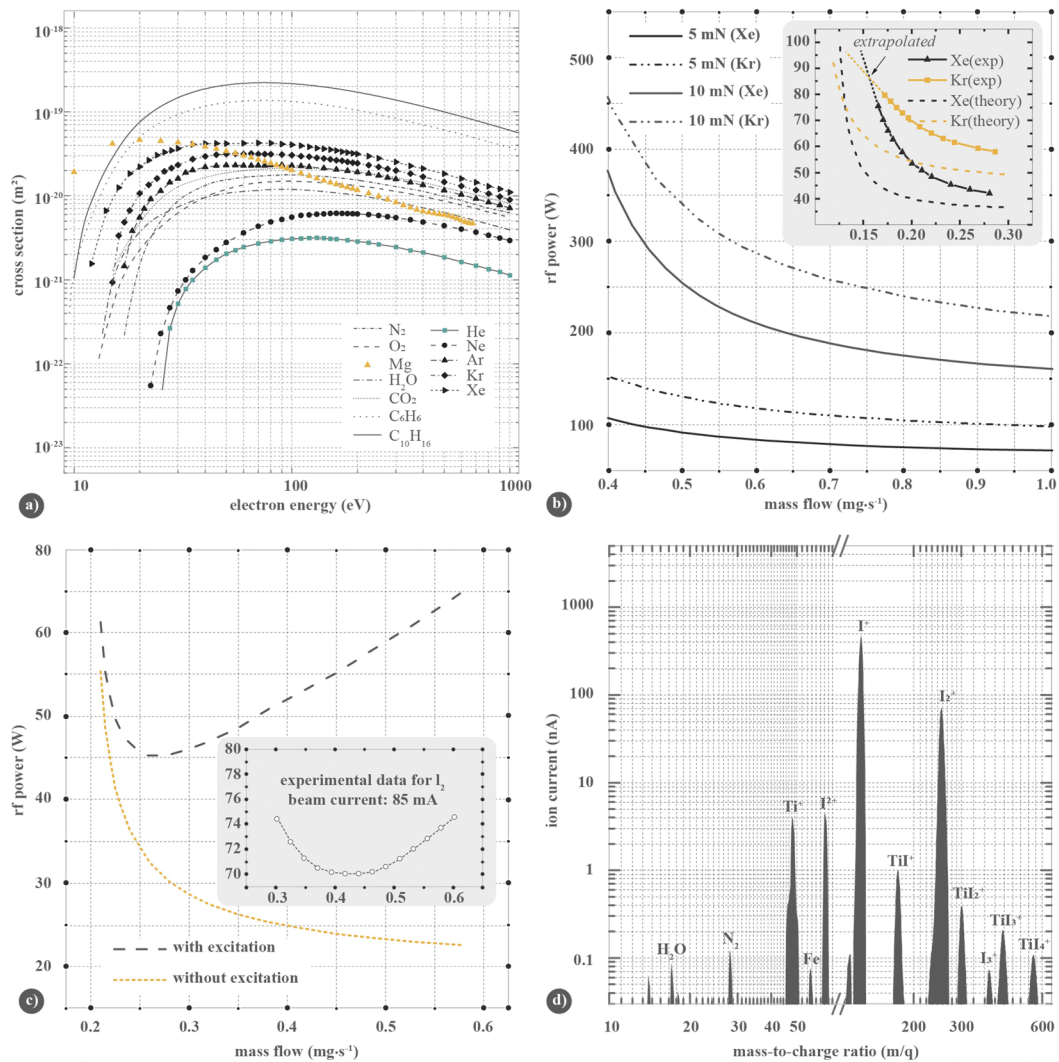


**FIG. 9.** (a) Electron impact ionization cross section of adamantane  $C_{10}H_{16}$  and other atoms or molecules relevant as propellants for ion thrusters. The cross section of adamantane was calculated using a binary encounter Bethe (BEB) approach.<sup>165</sup> Magnesium cross section data are taken from Ref. 166, water data are taken from Ref. 167, noble gas data are taken from Ref. 168,  $O_2$  and  $N_2$  data are taken from Ref. 169, and benzene data are taken from the NIST database (Ref. 170). (b) Calculation of the output rf-power of the RFG as a function of propellant mass flow (Xe and Kr) for constant thrusts obtained by global modeling. For comparison, sets of experimental and theoretical data comparing xenon and krypton are provided in the inset. The experimental data are limited in range by the current of RFG used. The intersection of the two calculated performance curves agrees with a linear extrapolation of the experimental data sets. (c) Effect of the electronic excitation of the neutral iodine atom on the performance mapping of a RIT. The curve shape agrees qualitatively with recently published experimental data (inset with data for a RIT-10 operated with iodine as the propellant).<sup>171</sup> (d) Spectrogram of the extracted ion beam of a RIT-10 equipped with titanium grids and operated with iodine. For better visualization, the mass scale is interrupted between 70 and 110, since there are no additional signals.

as well as flow properties. Global models may be used to correlate these microscopic properties with electrical power requirements for generating thrust. The global models comprise a system of rate equations for excitation, ionization, and other processes inside the plasma, which need to be solved for a given thruster geometry. We performed such calculations for a RIT-10 using the model suggested by Chabert and co-workers.<sup>158</sup> Figure 9(b) shows the results

for xenon and krypton used as the propellant for the thruster. It is assumed that the RIT-10 is operated with an excitation frequency of 1 MHz and a screen grid voltage of 1000 V and possesses a cylindrical discharge vessel. One can clearly see that the power consumption of the RFG is significantly higher for krypton than for xenon under the given assumptions. However, it can be concluded that, if sufficient electrical power is available, krypton will indeed be a suitable,



cheap alternative to xenon. In many mission scenarios, also mixtures of Xe and Kr may be considered a good compromise between cost and performance.<sup>175,176</sup>

A number of other chemical elements and compounds have been investigated in recent years in terms of their suitability as a propellant.<sup>172,177–179</sup> A promising candidate is molecular iodine, which was envisaged as propellant in the early 2000s.<sup>180,181</sup> Iodine has interesting properties. It is a solid under standard conditions but can be brought into the gas phase by sublimation at low power consumption. The mass density of  $4.9 \text{ g cm}^{-3}$  is about three times larger than that of xenon under storage conditions. Tsay and co-workers have shown the compatibility of iodine with rf-driven gridded ion engines.<sup>182,183</sup> A detailed experimental description of a laboratory iodine fluidic control and a test setup as well as a comparison of thruster performances for xenon and iodine have been published recently by Holste and co-workers.<sup>171</sup> Iodine shows similar performance values to xenon up to a certain mass flow. At higher mass flows, the power consumption for maintaining the same extraction current increases significantly compared to xenon. Global modeling, based on the work of Grondein and co-workers,<sup>184</sup> reveals that this increase in power is related to the amplified electronic excitation of neutral iodine atoms, which are present in the plasma in significant quantities due to the dissociation of the iodine molecule [cf. Fig. 9(c).]

Iodine as a propellant can be considered a good alternative to xenon for small satellites, since no pressure tank is required, the reservoir can take on any shape, and the storage volume for the same amount of propellant atoms is smaller than that for xenon. However, material issues due to the reactivity of iodine need to be addressed. Material issues may not play a dominant role in the case of small satellites as their operating times are short. However, for satellites that are operated with iodine over a longer period of time, the corrosiveness of the propellant cannot be ignored. An atmosphere of iodine will build up around the satellite and will be in contact with the materials used, giving the opportunity of chemical reactions. For example, mass spectrometric investigations [cf. Fig. 9(d)] of the extracted ion beam of a RIT operated with iodine as the propellant reveal that the titanium extraction grids react with iodine, yielding various titanium-iodine compounds as reaction products. Very likely, the protective oxide layer of the titanium metal is removed by the ion bombardment during thruster operation, exposing pure titanium metal to iodine and causing the reaction. A consequence of this reaction is the formation of a titanium iodide layer inside the discharge vessel, which in turn negatively affects the rf coupling efficiency. Similarly, it remains to be seen whether iodine is compatible with current neutralizer technology because the thruster and neutralizer of an EP system should run on the same propellant for economic reasons and for keeping the room needed on the spacecraft and the dry mass of the system low. This may pose some severe difficulties in the case of hollow cathodes (cf. Sec. IV B). However, first experiments at JLU show that rf-neutralizer technology can be made compatible with iodine as the propellant. Thus, material issues need to be clarified and will require adaptations of the EP system design. Besides this kind of intermediate material interaction, which is mainly an effect of plasma chemistry, there is already a simple chemical interaction of materials, mainly metals and alloys, by mere contact with iodine or iodine vapor, which is relevant for the entire spacecraft (for further details, see also Sec. IV J).

A more general investigation of molecular propellants was started by Dietz *et al.*<sup>174</sup> using molecules from the class of diamondoids as propellants for a RIT-type thruster.<sup>185</sup> These hydrocarbons sublime into the gas phase at moderate temperatures and, therefore, do not have to be stored in pressure tanks. The ionization energy of adamantane, the lightest of the diamondoids, is only about 9 eV, and for heavier diamondoids, the ionization energies are even lower.<sup>186</sup> Despite a high stability suggested by their structural relationship with diamond, a fragmentation of the diamondoids occurred in the plasma. However, these deficits may be overcome by a systematic screening for suitable molecular candidates combined with their improvement by chemical engineering.<sup>174,187</sup> This screening is based on an analysis of the fragmentation and ionization behavior of a molecule when bombarded by electrons of defined energy and is referred to as the delayed extraction time-of-flight (DETOF) method. For this purpose, a small amount of a potential alternative propellant is vaporized and introduced into a vacuum system so that a constant gas pressure is established. This gas target is ionized by means of an electron pulse in a defined interaction volume, whereby care is taken to ensure that at maximum, one ion is generated per electron pulse. This ion is accelerated by a high-voltage pulse to a single-particle detector, where it is detected. If the target density, number of electrons per pulse, interaction length, and response probability of the detector are known, the ionization cross section can be measured quantitatively. The mass of the fragments can be determined by measuring the time of flight from the point of origin of the ions until they hit the detector. The experimental setup is mainly based on the work of Straub and co-workers.<sup>169,188–190</sup>

The advantage of this method is that only a small amount of a possible molecular propellant needs to be analyzed, so there is no need to synthesize large quantities of the candidate molecule and to make time-consuming modifications to a test ion engine to obtain information about its suitability as a propellant. A further advantage over the use of photons as collision partners is the compact design of the experiment as well as the independence from large synchrotron radiation or complex laser sources. However, some inaccuracy must be accepted when determining the appearance energies, since UV light sources offer a significantly higher energy resolution.<sup>191</sup> If the DETOF method proves that a material is suitable, i.e., that it can be ionized with sufficiently high efficiency and only little dissociation occurs, the effort of testing the candidate molecule as a propellant in a thruster system will be worthwhile. Figure 10 shows representative mass spectra of three different molecules obtained by this method. Starting point of an extensive test series in search of alternative propellants, which is currently being carried out at JLU, is the aforementioned adamantane. Shown here are results obtained when bombarding adamantane with 15 eV electrons. Clearly visible are the dominant dissociation channels with masses around 93 u and 79 u. It should be mentioned that the setup is not optimized for mass resolution but for detection efficiency, therefore, the fragments at high mass numbers can only be measured with a resolution that extends over several proton masses. Similar results obtained under the same conditions at the same electron energy of the derivative 1-fluoroadamantane are shown for comparison. Already substituting one hydrogen atom with a fluorine atom leads to a significant change of the fragmentation behavior of the molecule at this energy. In addition to the mother peak at mass 154, another dominant peak appears

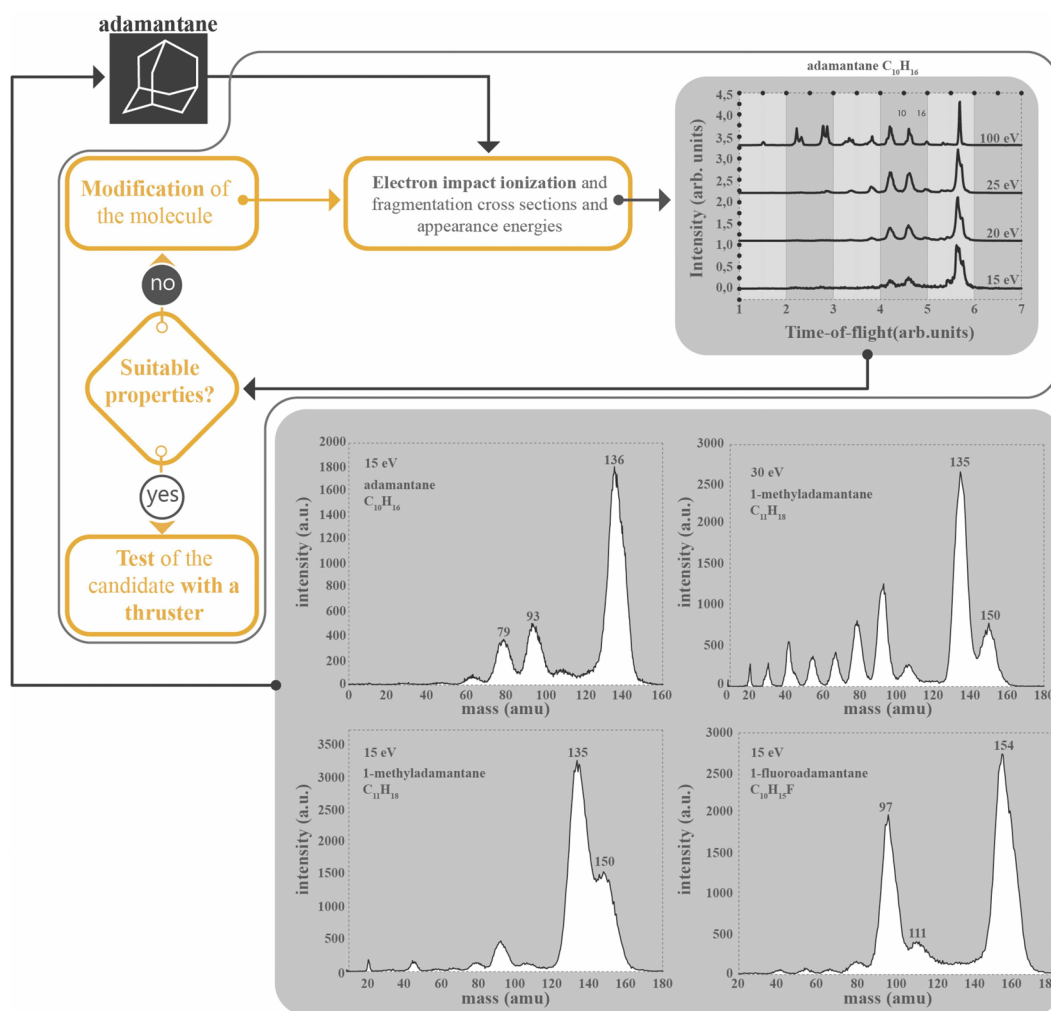


**FIG. 10.** Strategy for finding suitable alternative molecular propellants, exemplarily shown for adamantane  $C_{10}H_{16}$  and some of its derivatives. The idea is to determine the ionization efficiency and the dissociation of a molecule by electron impact at different impact energies. This measurement routine is performed for the molecule initially used as the starting point as well as for its derivatives in order to systematically investigate the effect of chemical modification on the parameters of interest. Shown is the energy-dependent dissociation of adamantane at different electron energies (small graph) and the dissociation of 1-fluoroadamantane  $C_{10}H_{15}F$  for 15 eV and 1-methyladamantane  $C_{11}H_{18}$  for 15 eV and 30 eV incident electron energy compared to adamantane at 15 eV impact energy (large graphs).

at mass 97 and a significantly smaller contribution at mass 111. Such a dissociation behavior would initially be considered favorable, since there are mainly two fragment groups, which makes the plasma not too complex, similar to an iodine plasma. Unfortunately, however, all diamondoid derivatives have so far shown a tendency to dissociate into a large number of fragments at higher electron energies, as shown here exemplarily for 1-methyladamantane for 15 eV and 30 eV electron bombardment. This gives the processes taking place inside the plasma a high degree of complexity, in particular, as fragmentation of the fragments may also occur. Thus, the density of both the neutral particles and the ions is difficult to control in such a plasma, making stable extraction challenging. In addition, deposits may form on the inner surface of the discharge vessel, e.g., in case

of adamantane, amorphous carbon is deposited. If the deposited material is conducting, the layer thickness will increase over time. This will deteriorate the coupling between rf coil and plasma and increase the risk of deposits between the screen and the acceleration grid, which may lead to short circuits. Furthermore, in case of barely conductive layers, charging effects may occur, which may result in charge eruption, e.g., between the grids and distort the stability of the thruster's discharge. Despite the challenges described above with the molecules tested so far, this systematic screening approach is a promising way forward. Currently ongoing investigations of heavier diamondoids are intended to test the hypothesis whether heavier molecules, in general, are more stable at electron energies up to a few tens of electronvolts. The electron-energy-selective analysis is

motivated by the assumption that the distribution of electron energies in the plasma is given by a Maxwell-Boltzmann distribution. Typically, the corresponding electron temperature  $T_e$  is in the range of a few electronvolts, but the high-energy tail of this distribution can contribute significantly to dissociation. In conclusion, taking into account that none of the chemical elements is the perfect atomic propellant in terms of the desired properties such as low ionization energy, high ionization cross section, high atomic mass, and availability the chemically designed molecules may provide interesting alternatives in the future, in particular, if the challenge of fragmentation may be overcome.

Due to the increasing number of small satellites in LEO, there might be an increasing demand for ion thrusters, which refuel their propellant reservoir exploiting the residual atmosphere. Such a possibility of refueling will increase the operating time of these satellites, which may even have a positive effect on the space debris issue. It may also give access to the altitude range between 120 km and 300 km, which is accessible neither with balloons or aircrafts as the particle density in this region of the atmosphere is too low for these vehicles to operate nor with satellites (only for a short mission duration) as the drag force caused by the residual atmosphere is very high.<sup>192</sup> The idea is to collect residual gas, which causes the drag force on the satellite, to compress it and to use it for thruster operation. This approach offers new possibilities for satellite operation in LEO. The atmosphere in LEO is mainly composed of nitrogen and oxygen. Therefore, this concept is known as air-breathing or residual atmosphere electric propulsion (RAM-EP). The viability of this method can be demonstrated in a back of an envelope fashion.

First, we will estimate whether the atmospheric pressure experienced by the moving spacecraft as static pressure is comparable to that inside a discharge vessel, i.e., whether further active compression is required in order to reach static pressures suitable for thruster operation. For simplicity, we assume that the residual atmosphere consists of a 1:1 mixture of molecular nitrogen and oxygen. The mixture possesses a mean molecular mass of 30 g/mol. Assuming that the satellite has an orbiting velocity of 7800 m/s, additional atmospheric random movement is negligible. The particle density of the residual atmosphere is then about  $10^{16}$  molecules per  $\text{m}^3$ . The maximum achievable static pressure  $p_{\text{stat}}$  inside the thruster vessel is given by the dynamic pressure  $p_{\text{dyn}}$  arising from the relative movement between the spacecraft and the atmosphere,

$$p_{\text{stat}} \leq p_{\text{dyn}} = \frac{1}{2} \rho v^2. \quad (20)$$

At best, one obtains  $p_{\text{stat}} = 0.015$  Pa. This pressure value is almost in agreement with the neutral gas pressure  $p_{\text{thrust}}$  required for operating a larger ion thruster such as a RIT-2X and more than one tenth of the neutral gas pressure required for operating a RIT- $\mu$ X. Thus, active compression of the collected gas is necessary in the case of smaller ion thrusters on the basis of atmospheric fuel intake only. However, achieving a compression factor  $f_{\text{comp}}$  between 1 and 10 should be technologically feasible.

Second, we will estimate whether the thrust  $T$  that can be generated by the collected atmospheric propellant is sufficient to overcome the atmospheric drag force  $D$  experienced by the satellite. The

latter is given by

$$D = \frac{1}{2} \rho c_D A v^2, \quad (21)$$

where  $c_D$  is the drag coefficient,  $A = 1 \text{ m}^2$  is the effective satellite area,  $\rho$  is the mass density, and  $v$  is the velocity of the medium with respect to the satellite, i.e., the orbiting velocity of the satellite. According to Jackson and Marshall, a typical value for the drag coefficient of a satellite is  $c_D = 2.2$ .<sup>192,193</sup> Under these assumptions, the drag force is about 33 mN. Assuming further that the accelerating voltage  $U$  of the thruster is 1000 V, the thrust (in mN) necessary to compensate the drag  $D$  can be written as

$$T [\text{mN}] = \sqrt{\frac{2M}{e}} I_b \cdot \sqrt{U} = 0.775 \cdot \frac{I_b}{[\text{A}]} \cdot \sqrt{U}. \quad (22)$$

A compensation of drag force  $D$  by the thrust  $T$  requires a beam current of  $I_b = 1.4 \text{ A}$ , which corresponds to a particle current of  $\sim 8 \cdot 10^{18}$  of singly charged exhausted particles per second. Assuming that the collection area corresponds to  $A$  and a compression factor  $f_{\text{comp}} = 10$ , the neutral particle current in the thruster is  $I_{\text{neutral}} = A f_{\text{comp}} \rho v \approx 8 \cdot 10^{20}$  particles per second. A typical value of the degree of ionization of the low-temperature plasma inside the thruster vessel is about 1%; thus, a compensation of the drag  $D$  by the generated thrust  $T$  based on the collected atmospheric propellant will be possible if the efficiency of collecting particles from the residual atmosphere is sufficiently high and if sufficient electrical power is available. In other words, the RAM-EP concept is viable.

Of course, these assumptions are only a rough estimate and there may be conditions where the mass intake is not sufficient to operate a thruster.<sup>194</sup> More realistic calculations must take into account additional effects such as the flow regime or special features of the atmospheric density distribution. For example, there are strong density fluctuations in the Earth's atmosphere in dependence on the solar activity. Furthermore, ionization efficiencies inside the plasma as well as aspects of material compatibility have to be considered in more detail on the system level. For example, hollow cathodes based on BaO are not suitable for operation in oxygen-rich environments. The RAM-EP concept occupies a small niche in the field of electric space propulsion. Publications are mainly found in the gray literature.<sup>195–197</sup> Nevertheless, some concepts seem to be pursued at least by JAXA and ESA. JAXA uses an ECR ion thruster and an intake with reflectors and honeycomb structure to prevent backflow of the trapped gas particles, yielding an inlet pressure of 0.5 Pa. The power requirement for an orbit at 170 km height is almost 5 kW.<sup>195</sup> ESA has carried out a feasibility study on RAM-EP and defined a potential roadmap for it.<sup>196</sup> Andreussi *et al.* from SITAEL have designed and tested with the support of ESA a RAM-EP system based on a double stage Hall effect thruster combined with an effective intake/collector assembly.<sup>198</sup> Test results are reported to be in line with the assumptions and have proven the functionality of RAM-EP on a sophisticated technology level.

It should be noted that the RAM-EP concept is not restricted to the Earth's atmosphere. It may also become of major interest for refueling thruster systems on interplanetary missions, e.g., on a Mars mission for refueling with  $\text{CO}_2/\text{N}_2$  from the Mars' atmosphere.<sup>199</sup> Somewhat similar is the idea of employing a minor fraction of



chemical propellant LH2/LOX or splitting H<sub>2</sub>O, i.e., H<sub>2</sub> and O<sub>2</sub> as propellants in an EP system, e.g., running the thruster on O<sub>2</sub> and a hollow cathode on H<sub>2</sub>.<sup>200–204</sup> Using H<sub>2</sub>O in a wider sense on a satellite can be very promising. On the one hand, water can be split into H<sub>2</sub> and O<sub>2</sub> using excess energy from the solar panels, and on the other hand, it may be used in a fuel cell to generate additional electric energy, when the electric energy output of the solar panels is low. Furthermore, a fraction of the water may be used as the propellant. Thus, a high degree of flexibility is gained in terms of energy and thrust management.

Finally, there is the group of solid metal propellants that we will briefly discuss. Here, magnesium, zinc, and bismuth, in particular, are considered suitable candidates for ion thrusters and indium is being used in FEEPs. In particular, the first two candidates are characterized by their easy availability and their non-toxicity. Due to their low atomic weight, they can be used to achieve high specific impulses, which is particularly interesting for Hall engines. Szabo *et al.* have demonstrated stable operating conditions for magnesium and zinc in a Hall engine.<sup>205</sup> The low atomic masses, i.e., high specific impulses at the usual 300 V anode voltage, have a positive influence on erosion rates. Equivalent specific impulses with xenon could only be achieved with high anode voltages (700 V and more), which may result in high erosion rates in the discharge channel. Another advantage of magnesium is that in the regolith of Mars and the Moon, larger amounts (~8%–10%) of magnesium can be found in the form of MgO, from which magnesium can be obtained quite easily, which would then be available as a propellant. In addition, the oxygen released in the process may be used as the propellant for thrusters, which are based on the RAM-EP concept. In contrast to these two light alternatives, bismuth has a high atomic weight but a very low vapor pressure. In order to provide sufficient propellant for operating the thruster, propellant temperatures of more than 700 °C are necessary, which makes the development and manufacture of a mass flow control system more difficult.<sup>179</sup> It is worth noting that mercury has been used as a propellant in the early days of EP.<sup>206</sup> Despite its toxicity, it is considered again as a suitable propellant for small satellites of LEO formations, raising major environmental concerns.<sup>207</sup> From the point of view of the required EP test facilities, these condensable metallic substances have advantages with regard to the pumping capacities required, since they are pumped off efficiently by condensation on almost any cold surface. Therefore, inexpensive cryogenic pumping systems can be used, which significantly reduces operating costs. The main disadvantage in terms of test facilities is, however, that these substances may be distributed throughout the entire vacuum chamber, where they can possibly lead to undesired material interactions, e.g., with the diagnostics systems.

## B. Neutralizer technology

The conventional established ion thrusters such as the HETs and the GIEs require electron sources for neutralizing the positive ion beams that generate the thrust. In the case of HETs and HEMPTs, the electrons from these cathodes are even essential for the operation of the thruster itself. The discussion in Sec. IV A has already demonstrated that using an alternative propellant in a thruster will also require an adoption of the corresponding neutralizer system as the same propellant should be used for both the

thruster and neutralizer for various technical and economic reasons. In the case of high thrusts, i.e., high ion currents in the range of a few amperes, which need to be compensated, hollow cathode neutralizer technology is currently the only choice. In the case of somewhat lower thrusts in the range of a few hundred milliamperes, rf-neutralizers may be an alternative. The working principle of the latter is somewhat similar to that of a RIT; only the electrons are extracted from the propellant plasma instead of ions.<sup>208</sup> Obviously, the electrode design will differ considerably. Going to even smaller systems, i.e., real miniaturized thrusters, both neutralizer schemes will fail as the challenges of miniaturization and also space-saving integration cannot be overcome. In this section, we will mainly focus on issues related to hollow cathode technology, and other developments in neutralizer technology, i.e., thruster systems with inherent neutralization, are addressed in Secs. IV C and IV F.

The insert material of a hollow cathode emits electrons by thermionic emission basically following the Richardson–Dushman equation

$$J = A \cdot T^2 \cdot \exp\left(-\frac{e\phi}{k_B T}\right), \quad (23)$$

where  $J$  is the current density,  $T$  is the temperature of the insert,  $e$  is the elementary charge,  $\phi$  is the work function of the material, and  $A$  is a material constant. Applying electric fields further reduces the work function due to the Schottky effect. A low work function severely increases the emitted current at a given temperature. Established technologies rely on the already mentioned materials BaO–W and LaB<sub>6</sub>.

The electride material C12A7:e<sup>−</sup> is currently considered a promising candidate for an insert material, in particular, due to preliminary reports of an ultra-low work function of 0.6 eV.<sup>209</sup> Such a low work function would reduce the temperature of the insert material required for operating the neutralizer to values below 1000 K. This should reduce the thermal stress on the hollow cathode system considerably. C12A7 stands for the ceramic Ca<sub>12</sub>Al<sub>14</sub>O<sub>33</sub>, which is synonym for the quasi-binary compound 12CaO·7Al<sub>2</sub>O<sub>3</sub> also known as mayenite. Lacerda and co-workers first reported on the high ionic conductivity of the material in 1988.<sup>210</sup> The material itself has so far been studied mainly for its unique crystal structure and the resulting properties.<sup>211</sup> It has a positively charged lattice framework, where one unit cell is made out of 12 cages, incorporating two unbound O<sup>2−</sup> ions in two central cage positions in order to maintain charge neutrality. The ionic conductivity is caused by these weakly bound oxygen ions O<sup>2−</sup>. A large number of investigations dealt with the transformation of the mayenite material into the electride phase where the two weakly bound oxygen ions O<sup>2−</sup> per unit cell are replaced by four electrons e<sup>−</sup> under strongly reducing conditions.<sup>212</sup> The transition C12A7:2O<sup>2−</sup> to C12A7:4e<sup>−</sup> is accompanied by a color change from almost colorless mayenite to black electride.<sup>213</sup> This color change reflects the change from the ionic hopping conductivity of the O<sup>2−</sup> ions to a metal-like conductivity of the electrons substituting the O<sup>2−</sup> ions.<sup>214</sup> The theoretical maximum electron density is  $N_e = 2.3 \times 10^{21} \text{ cm}^{-3}$ .

To optimize the electride material as an insert material for hollow cathodes, it is necessary to reliably assess the material's electronic and structural properties, in particular, to verify  $N_e$  of the electride samples. Different methods of verification were described by Yoshizumi.<sup>214</sup> Kim and co-workers used Raman spectroscopy to

assess  $N_e$ . This method is advantageous since it is non-invasive and quick as no sample preparation is required.<sup>215</sup> The work function  $\phi$  can be determined by the method reported by Matsuiishi *et al.*<sup>209</sup> A corresponding setup built at JLU for this purpose is described in the work of Reitemeyer and co-workers.<sup>216</sup> Recent measurements at JLU and other institutions have raised doubts concerning the ultra-low work function. Measurements yielded work functions in the range of BaO–W and LaB6 for the electride material provided by Advanced Thermal Devices (ATD) and Fraunhofer IKTS. Further investigations are required to clarify this issue. Another challenge to overcome is the low thermal conductivity of the electride material. Excess heat input into the electride may lead to structural destruction, i.e., means of efficient heat dissipation from the material into the environment need to be established in corresponding devices. The use of a heat sink<sup>217</sup> metallic coating on the outer surface of electride hollow cathodes or employing thin films of electride material is the first attempt in this direction. Improving the material properties by substitution offers additional possibilities of optimization. A major advantage that makes the investigation of this material worthwhile is its anticipated chemical inertness to many alternative propellants, in particular, iodine.

### C. Neutralizer-free technology

The development of neutralizer-free thrusters is sufficiently motivated by the challenges arising from the use of hollow cathodes for neutralization. Neutralizer failure is one of the main reasons for the failure of conventional EP systems on satellites.<sup>218</sup> In addition, with regard to small satellites, sufficient down-scalability cannot be achieved, i.e., these systems operate with low efficiency when miniaturized and therefore do not meet the low power requirements.

A simple concept of a cathodeless thruster has been suggested by Blackhall and Khachan.<sup>219</sup> They investigated an asymmetric hollow cathode with a hydrogen glow discharge inside providing a collimated plume of high velocity neutrals with a specific impulse of about  $3 \times 10^4$  s. The high amount of neutrals is caused by charge-exchange collisions between protons and neutrals. A thrust of 1 mN for 1 kW input power was estimated, yielding a power-to-thrust of 1000 W/mN. The hydrogen mass flow was 45 SCCM ( $66.9 \mu\text{g s}^{-1}$ ). Compared with the power-to-thrust ratio of a RIT, which is about 25 W/mN for large (RIT-10 and larger) and about 100 W/mN for miniaturized versions (e.g., RIT-2.5), the thrust efficiency is very low. The same applies to the mass efficiency of the cathodeless thruster. Nevertheless, this concept captivates by its simplicity.

Boswell and Charles followed a somewhat similar approach with their Pocket Rocket, using a capacitively driven rf microdischarge and jet expansion through a tube to increase the specific impulse of the emitted neutral gas.<sup>220,221</sup> The Pocket Rocket uses argon as the propellant and is driven with 13.56 MHz voltages. The dominant heating process is caused by ion-neutral collisions. Mitic and co-workers from JLU have studied the influence of the excitation frequency on discharge parameters using a comparable low-pressure argon plasma source with a hybrid surface/jet geometry.<sup>222</sup> The glassy discharge vessel has a conical shaped body (20 mm base diameter and height) with an outgoing cylindrical tube of 40 mm length (inner diameter of 4 mm and thickness of 2 mm). The system possesses two electrodes. Possible excitation frequencies are

31 kHz and 13.56 MHz, and peak-to-peak voltages are 2 kV–12 kV. One electrode is located outside the conical base, and the other surrounds the tube and can be varied in position. The thruster was operated in three different voltage modes—only kHz, mixed kHz + rf, and only rf. Phase resolved optical emission and laser absorption spectroscopy showed similar behavior in the singly kHz and rf driven modes (1.4 eV–3.3 eV electron temperature, electron density variations by two orders of magnitude), while the mixed mode showed only small variations in plasma parameters with an intermediate electron temperature (2.2 eV). This interesting result indicates that the frequency of operation may play an important role in compromising between costs and performance, especially since frequency generators in the low frequency range are simpler in their design.

Another possibility of generating thrust with the help of EP without a neutralizer is to accelerate the entire plasma. Three concepts appear promising here: the magnetoplasma dynamic thruster (MPDT), the helicon thruster (HELT), and the ECR thruster (ECRT). The MPDT and HELT were discussed in detail by Ahedo.<sup>223</sup> Magnetic nozzle expansion in an ECRT was recently suggested by Cannat and co-workers from ONERA.<sup>224</sup> They introduced an electrodeless ECR plasma thruster with coaxial geometry, providing thrusts in the order of 1 mN with 16% total thruster efficiency [see Eq. (12)] and a specific impulse of about 1000 s using xenon as the propellant. Figure 11 shows the coaxial thruster design together with an ion beam profile and ion energy measurement. A test campaign of a low-power version of such an ECRT was carried out in the JUMBO space simulation facility at JLU. The goal of this campaign was the analysis of thruster performance parameters (thrust, plasma potential, ion energy, and beam structure) as a function of residual gas pressure. The JUMBO facility (diameter of 2.6 m and length of 5.5 m) provides pumping speeds for Xe in the order of  $150\,000 \text{ l s}^{-1}$  and base pressures below  $2.0 \times 10^{-7}$  mbar. Thrust measurements were performed using a double-armed inverted pendulum thrust balance with sub-mN resolution. It employs an interferometer for optical measurements of the balance displacement, voice coil actuators driven by a PID-controller for compensating the thrust, and a passive eddy current break for sensitivity adaptation. The background pressure inside the vacuum chamber was adjusted by injecting a well-defined xenon mass flow. The ECRT provides ion energies of about 288 eV. The energy measurement was carried out with a parallel-plate analyzer (PPA). The inlet opening of the PPA has been aligned with the symmetry axis of the thruster. The ion beam divergence angle (half angle) is about  $31.45^\circ$  and mainly determined by the diverging field of the magnetic nozzle. The results from the residual Xe pressure measurements are shown in Fig. 11. Both the thrust and the thruster potential increase when the residual gas pressure decreases. Thrust measurements at ONERA and JLU show the same trend but show an offset to each other, which may be caused by different residual gas distributions inside the vacuum facilities. These facility effects are known in the community but not sufficiently investigated yet.<sup>225</sup> Mainly engines with open structures are susceptible to these effects (e.g., HETs) and less so the GIEs because they exhibit a mechanical barrier for gas backflow into the plasma. The facility effect of the ECR thruster is less pronounced in the measurements of the thruster potential. More about handling facility effects can be found in Secs. IV D and IV E.

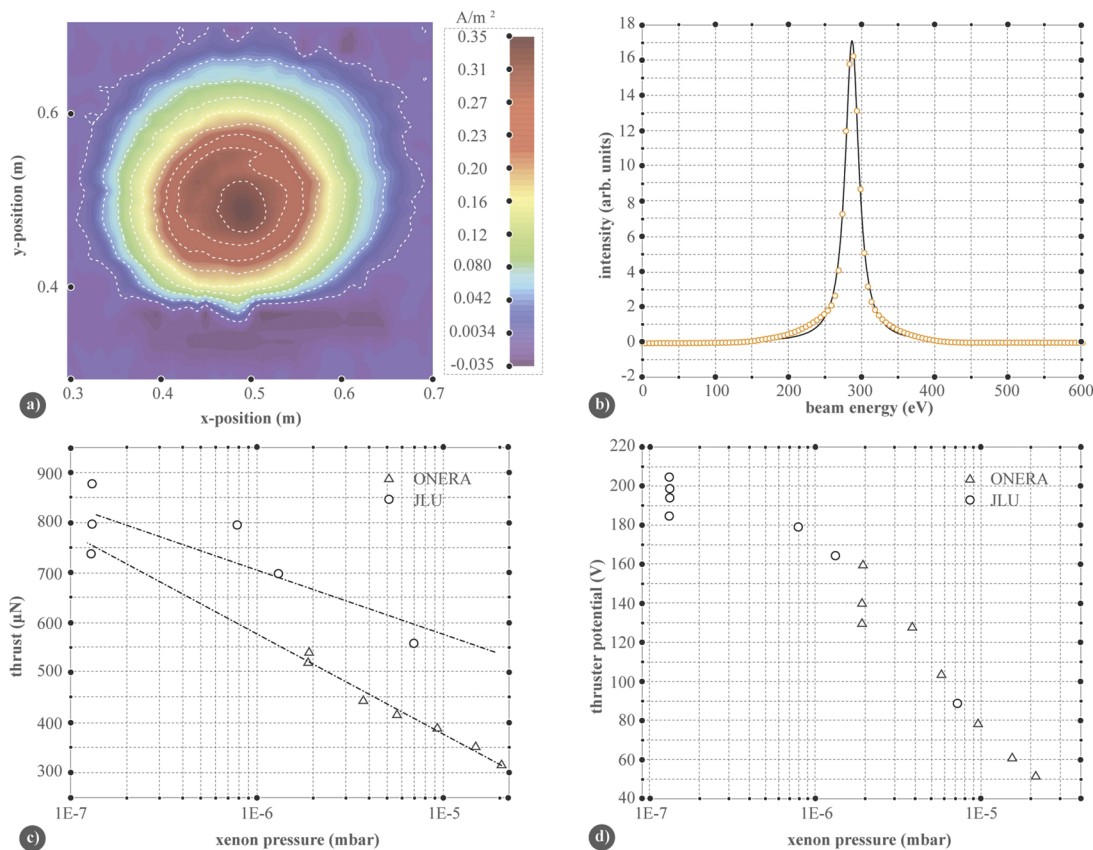


**FIG. 11.** (a) Ion beam profiles and (b) ion beam energies have been measured at JLU's space simulation test facility with an array of 53 Faraday-cups and a parallel-plate analyzer (PPA) (aligned to the symmetry axis of the thruster) for comparison with previous data from ONERA's test facility. The investigated ECR thruster was a low-power version (24 W) using a 2.45 GHz microwave input at 1 SCCM xenon mass flow. Comparison of measurements of (c) thrust and (d) thruster potential of ONERA's ECR thruster at two different test facilities. The graphs illustrate that careful diagnostics of the thruster's properties is indispensable for ensuring its suitability for use in space. Beam profile measurements allow one to assess the threat to the satellite posed by direct ion impingement. In particular, in the case of a magnetic nozzle, such as the one used in the ECR thruster, high divergence angles of the plume may arise. Since the ECR thruster does not employ an accelerator electrode, the energy measurement provides important information about the thruster's efficiency. Furthermore, thrust measurements are essential for assessing the thruster's performance. Measuring the thruster potential provides important information for evaluating thruster simulations. Comparative measurements at different facilities reveal facility effects that need to be accounted for in order to reliably predict the thruster's performance in space on the basis of terrestrial testing.

In addition to the ejection of neutral particles or the entire plasma, there are concepts that separate the process of extracting positive and negative charges from a plasma in time such as the PEGASES concept, the NEPTUNE concept, or ambipolar schemes employed in the case of miniaturized electrospray emitters running on ionic liquids, discussed in Sec. IV F. The PEGASES concept provides plasma propulsion using electronegative gases (F, Cl, Br, and I).<sup>226</sup> The rf driven discharge is divided into a plasma core and an ion-ion region by using a magnetic filter. Electrons are confined to the core region and cooled by collisions, which increases the efficiency of electron attachment to electronegative neutrals. The filter is transparent for positive and negative charged ions, which will constitute the ion-ion plasma. When an alternating voltage is applied to the grid system, particles of both charge signs are extracted alternately in time, providing charge neutrality on average. An alternating

grid voltage is also used by the NEPTUNE thruster, providing permanent extraction of ions and periodic extraction of electrons from a rf-biased two-grid system.<sup>227</sup> Ion beam energies up to 400 eV have been demonstrated with the NEPTUNE concept. Due to the alternating emission of ions and electrons, there is no limitation of ion beam density by the Child-Langmuir law, which is a clear advantage compared to classical GIEs with an external neutralizer. Nevertheless, long-term stability and lifetime have to be demonstrated for both the PEGASES and NEPTUNE concepts.

#### D. Modeling

Theoretical modeling of EP systems is an important tool for understanding the underlying physical processes, on the one hand, and for accelerating development processes, on the other hand. The

choice of the model used depends on the question at hand. The range of models and the underlying assumptions are widespread. For example, the PIC method can yield understanding at the particle level, i.e., on the microscopic scale, whereas global models treat the plasma in a heuristic statistical way. It is inherent to theoretical models that they approximate a physical system using a mathematical description based on a set of assumptions. To understand a physical system and its “true nature,” one needs to combine experiments and theoretical modeling, in particular, in order to validate the model and its assumptions against experimental results. Only such a validation will give a model a predictive power, which can be used to optimize EP devices and to speed up qualification. While some theoretical frameworks can directly derive an analytical solution, the majority must rely on computer simulations. Typically, numerical approaches are used to solve real-life problems, as the underlying mathematical description is usually nonlinear and rather complex. In this section, we will focus on PIC modeling used for describing the plasma properties inside RITs or the impact of the plume of an operating thruster on its test environment.

In general, a plasma is characterized by parameters such as gas pressure, plasma density, and electron temperature.<sup>228</sup> The Debye length,  $\lambda_D$ , is the length scale associated with Coulomb shielding of the plasma, and the Debye number is a parameter given by the average number of electrons in a Debye sphere,  $N_D = (4/3)\pi\lambda_D^3 n$ , where  $n$  is the number density. For  $N_D \gg 1$ , collective electrostatic interactions from all other particles in the Debye sphere dominate over binary collisions, and such a plasma is called weakly coupled plasma, whereas a plasma with  $N_D \ll 1$  is known as strongly coupled plasma. Figure 12 shows a variety of plasmas observed in the universe ranging from the laboratory plasma via atmospheric plasma to space plasma, according to their plasma parameters. It can be seen that the plasma states differ in the particle densities, given in Fig. 12 as electron density (which is equal to the ion density) and the electron temperature (which assuming an equilibrium state yields the kinetic energy distribution of the electrons as a Maxwell distribution). Plasmas in ion thrusters are in a somewhat intermediate range in terms of particle densities and electron temperature and can be considered as low-temperature plasmas.

Computer simulations of plasmas can be based either on kinetic or on fluid descriptions.<sup>229</sup> Fluid simulations use a magnetohydrodynamic (MHD) equation, with assumed transport coefficients characterizing macroscopic quantities such as density and temperature. Such fluid simulations have been employed successfully for the analysis of Tokamak plasma and ECR ion sources in the past.<sup>230,231</sup> In contrast, the kinetic description is more detailed because each species, i.e., ions, electrons, and neutrals in the plasma, is treated as a collection of particles with individual positions and velocities in the presence of an external electromagnetic field. Since the pioneering work in the 1960s by Dawson and others, involving few thousand of particles only at that time, the kinetic codes have evolved and modern codes can treat now  $10^6$ – $10^{12}$  particles using powerful computers.<sup>232,233</sup> Kinetic simulation has proved very successful for solving problems in which particle distributions deviate from a Maxwellian distribution due to stochastic heating, wave-particle resonances, or trapping. Another commonly used approach is the hybrid model in which some species, typically ions, are described using a kinetic approach and others (electrons) are described using a fluid approach.<sup>234–236</sup> In inductively

coupled plasmas at low pressures, when the electron mean free path is comparable to the lateral dimensions of the discharge vessel, kinetic effects come into play, and the electron distribution function may become substantially non-Maxwellian.<sup>237</sup> Therefore, it becomes necessary to develop an entirely particle-based simulation tool for the understanding of plasma properties in such situations, e.g., those of a propellant plasma inside the discharge vessel of ion thrusters.

The PIC method is based on calculating the trajectories of the particles inside the plasma. Thereby, one discretizes the underlying partial differential equations in time  $\Delta t$  and space  $\Delta x$ . On the latter grid, the electromagnetic fields are evaluated, whereas the particles themselves can have any position in space. A single computational cycle, i.e., time step, of the PIC algorithm comprises the following routines: a particle mover, interpolation of charge and current source terms on the grid, computation of the fields on grid points, and, finally, interpolation of the fields from the grid to the particle locations. Two important conditions needed to be satisfied regarding time step and grid size are

$$\Delta t < 2\omega_{pe}^{-1},$$

$$\Delta x < 3.4\lambda_D,$$

where  $\omega_{pe}$  is the plasma frequency.<sup>238</sup> Monte Carlo collision (MCC) methods have been developed to simulate binary collisions, e.g., elastic collisions between charged and neutral particles. In the widely used binary collision model, particles are grouped according to their cell locations and then paired randomly, and finally, they collide.<sup>239</sup> Mostly, the collision model uses either a direct Monte Carlo scheme or a null-collision scheme, which is a little faster.<sup>240,241</sup> By including the MCC method in the code, one can account for important aspects inside the plasma such as the production of new ions and electrons, energy losses, and heating mechanisms. The interaction of the ions with electromagnetic forces and with the neutral gas can be described with the DSMC method for inter-particle collisions. The DSMC technique is a stochastic particle-based method for the simulation of rarified gas flow problems developed by Bird.<sup>242</sup> Figure 12(b) shows the ranges of characteristic plasma parameters where MHD, hybrid, and PIC modeling are used.

As a typical example, we will discuss the modeling of the plasma inside a RIT. The modeling can be divided into electromagnetic field generation, plasma production, multi-species dynamics, and ion extraction. Some software packages exist, which can be used to simulate either of these tasks individually or combined to solve the problem at hand. XPDP1-XOOPIC is a popular PIC open-source code for devices with plasma confined in the planar, cylindrical, or spherical geometry.<sup>243</sup> Accounting for the external circuit and the neutral gas interaction is possible in 2D and 3D. COMSOL is a commercial package that can be used to simulate plasma in a given ion thruster geometry along with the neutral gas flow.<sup>244</sup> Traditionally codes such as IGUN, IBSimu, and KOBRA3D are used to design ion extraction systems and beamlet formations.<sup>138,140,245</sup> The newly designed dsmcFOAM + software can be used in combination with these packages for the plume simulation of ion thrusters.<sup>152</sup>

Typical RF thrusters operate at frequencies in the range from 0.5 MHz to 5 MHz. The electric and magnetic fields are concentrated



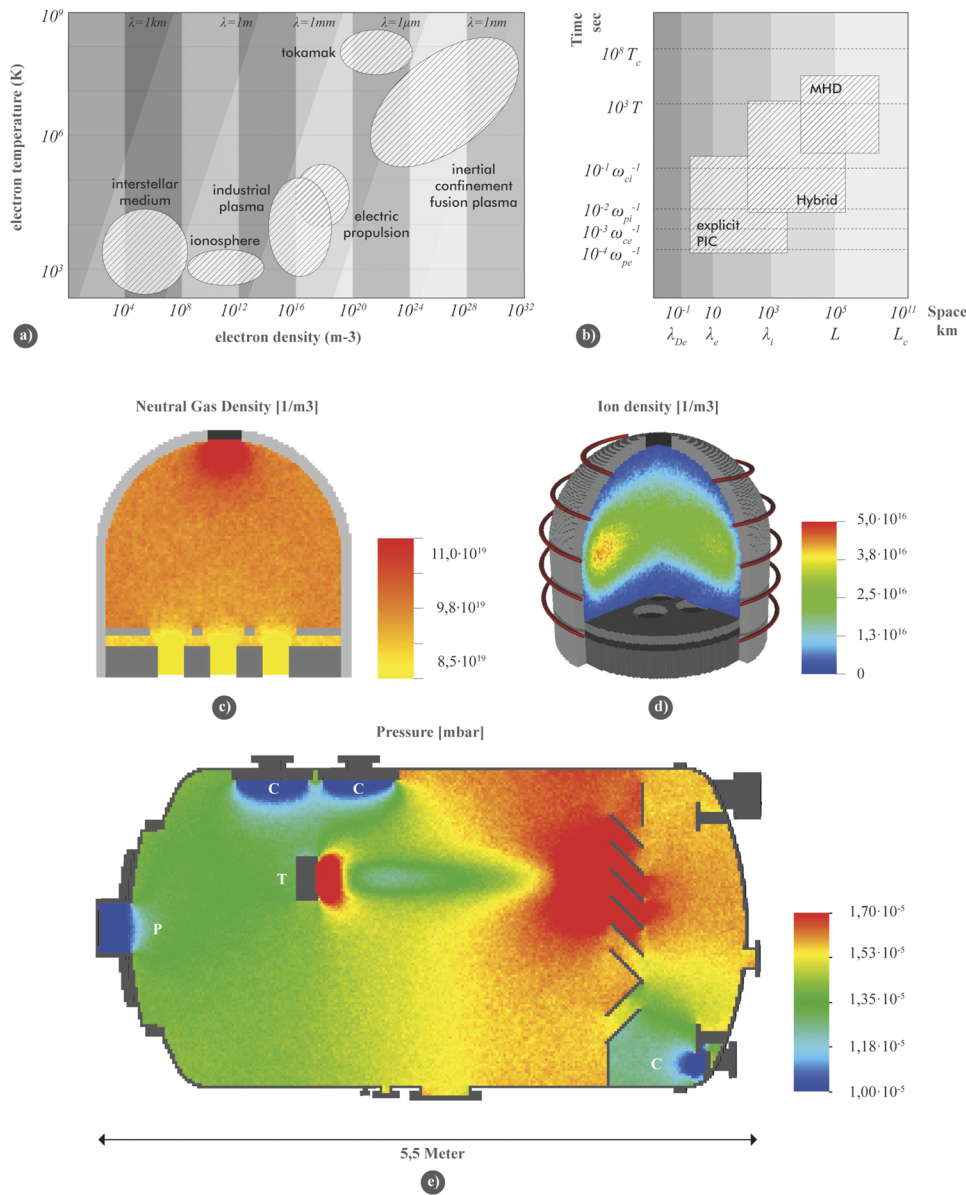


**FIG. 12.** (a) Different types of plasmas characterized by temperature and electron density. (b) Scope of application of different models. Simulations for the RIT-1.0 thruster on two different scales and scenarios. (c) The DSMC simulation of neutral gas density distribution in the small thruster. (d) Induced plasma using the given neutral gas densities. The CAD model depicts the coils, discharge chamber, and extraction grid. (e) Neutral gas distribution in a large vacuum chamber used at the JLU test facility (P: turbo pump, C: cryogenic pump, and T: thruster). The tilted lines downstream the plume direction depict the chevron-type beam dump.

in a thin skin layer at the outer edge of the plasma. The electron temperature  $T_e$  is not spatially uniform due to the presence of the skin layer. The highest electron temperature occurs inside the skin layer next to the wall and drops exponentially toward the center axis of the cylindrical or semispherical discharge vessel. Nevertheless, the plasma density  $n$  is highest at the center of the discharge.<sup>246</sup> Given a typical plasma density in the order of  $10^{17} m^{-3}$ , the time step needs to be in the order of  $10^{-11} s$  and the grid size as small as 0.1 mm. Assuming a small thruster ( $\mu$ RIT 1.0) with a diameter of 1 cm or a volume of about  $10^{-6} m^3$  requires for a proper description  $10^6$  grid points where information on electromagnetic fields along with charge and current densities has to be stored. Additionally, about  $10^9$

particle positions and velocities need to be continuously updated at every time step for each species. This clearly shows that the existing packages cannot be used for extensive plasma simulations on desktop computers unless significant simplifications of the plasma description are made, e.g., in terms of the maximum number of particles used or spatial resolution of the grid. To overcome such limitations, various research groups have invested in the development of dedicated particle-based codes to design and optimize ion thrusters and their components. The RF-plasma simulation and ion extraction grid lifetime were investigated for gridded ion thrusters.<sup>142,248</sup> ISOLDE is a code developed for 3D electromagnetic PIC simulations of the neutralization of the ion thruster beam and of the solar

wind interaction with the neutralized thruster beam.<sup>248</sup> Other PIC based packages such as oIOM are developed to investigate HEMP based ion thrusters.<sup>249–251</sup> Furthermore, a multiscale modeling of thruster-plumes using a 3D PIC method was developed<sup>252–254</sup> and the plume simulation using modern graphics processing unit (GPU) computing has been discussed.<sup>255</sup> More recently, additional extensive tools such as Smilei and PICLas have been introduced to simulate the plasma with multiple ion species along with neutral gas distribution.<sup>256,257</sup>

We at JLU designed PlasmaPIC for modeling RITs.<sup>258</sup> Apart from describing inductively coupled plasmas, the code can also be used for a wide range of low-pressure low-temperature plasmas. It is an object-oriented code written in C++. PlasmaPIC is a fully three-dimensional software. It is suitable for describing plasmas in electrostatic as well as electrodynamic fields. A unique characteristic of PlasmaPIC is the incorporated massive parallelization of all program routines, which makes the code highly efficient. PlasmaPIC also distinguishes itself by the possibility of handling arbitrary geometries confining the particles described, i.e., discharge vessels of various geometries or test chambers with defined locations of the pumps. The MCC module within PlasmaPIC assumes a neutral gas of a known particle density distribution as a background gas. Elastic scattering, excitation, and ionization are considered in electron-neutral collisions. In the case of ion-neutral collision, only the elastic collisions are accounted for in PlasmaPIC. Assuming a hard-sphere model, all collisions can be described by a uniform and isotropic scattering in the center of mass frame. The special but in the context of GIEs very important type of elastic CEX scattering in ion-neutral collisions is treated explicitly in PlasmaPIC. Cross sections for the scattering processes were taken from the plasma simulation tool Xoopic. For the modeling of an inductively coupled plasma of a RIT, a common approach is to separate Maxwell equations into an electrostatic and an electrodynamic part. The electrical fields from both parts are then added following the superposition of fields. Dirichlet boundary conditions are incorporated at the boundaries.

For the MCC module, a description of the neutral gas distribution is required. For this purpose, a DSMC module is implemented into PlasmaPIC. It can describe neutral gas densities in arbitrarily shaped vessels. Thereby, initially, the neutral gas density is calculated, and then, the plasma is simulated based on this density. However, the plasma simulation considers the neutral gas distribution as constant in time. Thus, it is assumed that the influence of the plasma on the neutral gas is negligible. If this assumption does not hold, the neutral gas simulation and the plasma simulation have to be iterated self-consistently to account for the influence on each other. Using this technique, neutral gas densities and its influence in vacuum test facilities can also be calculated.

We performed a simulation of a Xe-plasma inside a RIT-1 using PlasmaPIC on 384 CPU cores over 225 rf-cycles. A realistic neutral gas density of  $8.5 \cdot 10^{19} \text{ m}^{-3}$  over  $45 \mu\text{s}$  was assumed. Figure 12(c) shows the neutral gas distribution in the ion thruster derived using the DSMC module. This gas distribution is then used as input distribution for MCC module for the calculation of binary collisions. Figure 12(d) depicts a cut-computer aided design (CAD) model of the ion thruster along with the RF coils that couple energy into the plasma. The ion density distribution after a stable plasma condition is reached is shown inside the plasma vessel. Recently, a multigrid solver was integrated along with the load balancing

method, which boosts the capacity of the code to simulate even a RIT-2.5 in a reasonable period of time using available computational resources.<sup>259</sup>

It should be noted that PlasmaPIC can also be used to calculate realistic spatial distributions of the background pressure in vacuum test facilities with operating thrusters. Figure 12(e) shows the neutral gas distribution inside the JUMBO vacuum test facility simulated using the DSMC module alone. Such simulations after validation of the model are of major interest when extrapolating from thruster performance in the test facility to that under real space conditions. The background pressure and the interaction of the plume with the walls of the test chamber may have a severe impact on the performance of the thruster, e.g., higher background pressure between the grids makes CEX more likely leading to stronger grid erosion or the back flow of propellant gas into the thruster via the grid raises the pressure inside the vessel above that expected due to the nominal mass flow of the propellant (see also the discussion of the ECR thruster's performance in Sec. IV C).

## E. Test facilities and standardization

The development and qualification of ion engines are linked to suitable vacuum test facilities. These must provide optimum operating conditions for the thrusters to be tested in the sense of creating a working environment as close as possible to that in space. While off-the-shelf solutions for test facilities, which can be supplied by commercial suppliers, are often suitable for smaller engines, test facilities for engine classes with power outputs in the kW range are typically individual products. To our knowledge, major vacuum suppliers can cover test chambers for thrusters up to the power range of  $\sim 5 \text{ kW}$  as individually customized solutions. The costs for such a test facility represent a major financial hurdle, especially, for SMEs. User fees can be in the order of several thousand US dollars per test day, which is justified considering the high operating costs of such systems. The size of such test facilities scales with the power class of the engines. Medium-sized test facilities such as the JUMBO facility at JLU (diameter: 2.6 m, length: 5.5 m, and pumping speed for xenon: 150 000 l/s) are ideal for engines up to about 5 kW, especially assuming GIEs. HETs with comparable power can already be above the limit here, since they exhibit a higher propellant consumption than GIEs. More powerful engines can be operated in such systems for short periods of time, but then under poorer vacuum conditions, making long-term tests impossible as the test conditions deviate too much from that in space. Due to the high acquisition and maintenance costs of EP test facilities for engines in the high power range, adequate test facilities are only available in small numbers. Invigorito and co-workers provided a list of major test facilities, mainly located in US, Italy, Germany, The Netherlands, and France.<sup>260</sup> In the following, some general remarks on the requirements for a test facility and their possible realization shall be made. Three aspects should be considered as crucial: pumping speed, energy dissipation, and vacuum quality.

Larger engines (5 kW class) require continuously a certain amount of propellant (usually xenon), which can easily be in the range of 50 SCCM–100 SCCM. Based on a working pressure of better than  $1 \times 10^{-5} \text{ mbar}$ , a pumping speed of the vacuum system of 160 000 l/s would be necessary for a propellant mass flow of 100 SCCM. It is obvious that this can only be achieved either

with very large oil diffusion pumps or cryogenic vacuum pumps. Since oil diffusion pumps produce an unavoidable oil mist in the vacuum system, it is advisable to rely on cryogenic pumping systems for vacuum quality. Due to the vapor pressure of xenon, temperatures of the cryogenic surfaces of less than 50 K must be guaranteed. When designing the cooling surface, care must be taken to ensure that it is sufficiently large to achieve the required high pumping speed and that the heat input radiated from the warm part of the vacuum system and from the thruster can also be sufficiently dissipated by the cold heads. A pre-cooling of the surroundings of the cryogenic surfaces based on LN<sub>2</sub> panels is a possibility to reduce the heat input but may have a negative influence on the effective total area for xenon pumping. Another possibility is to shield the cryogenic surface facing the chamber wall with multiple layers of Mylar foil. However, the total area available is also reduced here. When designing these cold surfaces with the aid of simulation tools, it must be taken into account that the emissivity of the cold surface can change significantly due to freezing of xenon. This goes along with a severe reduction in the pumping speed depending on the amount of xenon ice bound to the cold surface and charging of the Xe ice surface, which may affect the thruster plume and, as a consequence, also the performance of the thruster. The behavior is similar to H<sub>2</sub>O ice.<sup>263</sup> This also implies that not only the pumping speed of the pumps employed must be optimized but also their geometric arrangement inside the vacuum test facility. The geometric arrangement will also determine the spatial background pressure distribution within the vacuum facility, in particular, in front of the thruster. This has a direct impact on the thruster's performance as it determines the backflow of the neutral propellant into the thruster and, in the case of GIEs, also the number of CEX processes occurring in the space between the grids that are mainly responsible for grid erosion. Furthermore, the magnitude of the background pressure will also affect the plume profile due to scattering processes between expelled ions and neutrals. Thus, plume diagnostics may yield results that do not directly reflect the behavior in space. It is worth noting again that PIC modeling, as described in Sec. IV D, may considerably contribute to optimizing test facilities and establishing comparability between different facilities. If such an understanding is obtained and the PIC models are fully validated, the comparison of experimental test results in a facility with theoretical simulations can be used directly for extrapolating to the thruster's performance in space. This may considerably contribute to speeding up space qualification and lead to shorter development cycles and, thus, a shorter cradle-to-market time.

In the case of a thruster in the power class of 5 kW and above, this power is almost exclusively converted into beam power, which is released in the form of a directed plume of fast charged particles. When hitting, e.g., the chamber wall or an upstream catcher, material will be sputtered and distributed within the chamber volume. It has turned out to be favorable to use special collection systems, so called beam dumps, for accommodating the plume energy. Beam dumps typically possess graphite surfaces, which are water-cooled. The beam power is converted into heat on the graphite and then dissipated by the cooling system. The graphite ensures a minimal sputtering of material due to its low sputter yield. Two possible implementations of a so-called beam dump are shown in Figs. 13(a) and 13(b). For the design of the beam dump of the JUMBO facility, we investigated different types of graphite prior to its construction,

in terms of sputter rates and porosity. However, the differences in sputter rate were rather small so that the densest material was chosen as it exhibits the smallest effective surface area. This implies that there are less adatoms on the graphite, which leads to shorter pump-down times of the system. Due to an inclination of the graphite panel surfaces relative to the ion beam direction, the sputter yield is somewhat larger than for perpendicular impingement (see also Sec. IV J). However, chevron-type arrangement of the graphite panels relative to each other can give the sputtering products a preferential direction toward the area behind the beam dump, where the sputter products and the propellant atoms can be pumped off with appropriate pump systems. This chevron-like arrangement of the graphite panels also avoids the building up of a high propellant pressure in front of the beam dump, which may affect the plume as described above.

Sputter products can settle on surfaces in the form of flakes [cf. Fig. 13(c)] and lead to short circuits or other problems. A detailed analysis of backspattering on thruster testing is given by van Noord and Soulas and with a stronger focus on various beam dump geometries using a DSMC-PIC code by Zheng and co-workers.<sup>264,265</sup> In addition to the vacuum system, the EP test facility provides a number of typical diagnostic tools for analyzing the thruster or the ion beam. In the test setup shown in Fig. 13(d), the most important diagnostic tools are integrated on a suitable positioning unit. Beam current measurements can be performed with the help of a Faraday probe, a retarding potential analyzer (RPA) gives access to the ion accelerating potential, and an  $E \times B$ -probe (Wien filter) measures the velocity distribution of the ions. Optical instruments facilitate visual inspection of the thruster; for instance, they allow for an *in situ* inspection of erosion effects. A pyrometer and an infrared camera give access to thruster temperatures, and a thermal probe measures the power deposition per surface unit. The whole setup was developed in the framework of the Advanced Electric Propulsion Diagnostics (AEPD) project funded by ESA as a first step toward standardized diagnostics tools. In the project, the diagnostics system has been used to characterize two different thrusters (a HET and a GIE) in two different test facilities and to compare the results in order to assess the susceptibility of the two types of thrusters to facility effects. It turned out that the GIE is less susceptible to facility effects than the HET, the reason being the grid system of the GIE. It separates very efficiently the regions of plasma generation and thrust generation and makes the plasma generation less prone to interaction of the plume with the facility walls. More details about the setup and the results of the test campaign can be found in the publications by Bundesmann and co-workers.<sup>262,266,267</sup>

Standardization of test conditions is a hot topic in the EP community. Test facilities worldwide vary in size, vacuum pumping systems, beam dumps, and diagnostics used. It is self-evident that measurement methods must be referenced to a common standard, but certain effects, such as the backspattering of material or the interaction between the plume and the chamber, cannot be standardized. Supporting tools such as reliable DSMC and PIC simulations will turn out helpful but need to be fully validated for this purpose. In addition, these test facilities must be tailored to their intended use. Facilities for development tests require a high degree of flexibility. For this purpose, they must be able to quickly generate a suitable vacuum and facilitate a quick return to atmospheric pressure in order to guarantee a high throughput of test articles. Facilities for



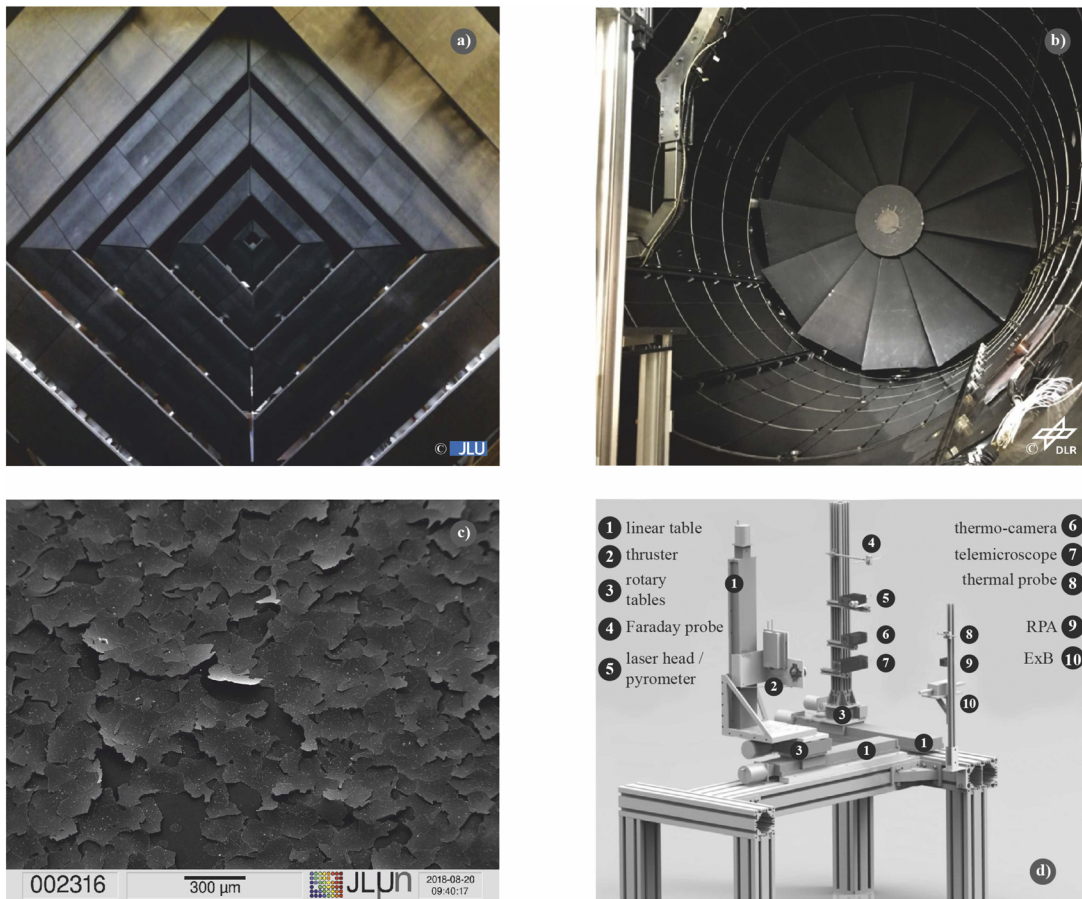


**FIG. 13.** (a) Pyramidal arrangement of water-cooled graphite surfaces in the JUMBO test facility (diameter: 2.6 m) in Giessen, inclined toward the direction of the jet. (b) Carbon beam dump in the STG-ET vacuum facility (diameter: 5.0 m) in Göttingen, Germany. The angle of inclination of the surfaces can be adjusted flexibly. In addition, the surface of the rear part of the system is also lined with graphite on the cylinder barrel, which is particularly advantageous for very divergent ion beams.<sup>261</sup> (c) SEM picture of a witness plate (2 in. silicon wafer) inside the JUMBO test facility behind the thruster after an endurance test of a high power ion engine. (d) AEPD platform developed in the frame of an ESA project toward standardization of test procedures.<sup>262</sup> Reprinted with permission from Bundesmann *et al.*, *Eur. Phys. J. D.* **70**(10), 212 (2016). Copyright 2016 Springer Nature.

lifetime tests must have a low rate of backspattered particles, i.e., a very high vacuum quality. Currently, the space agencies worldwide are still somewhat reluctant to define binding standards for EP testing. As the task of standardization is fully in line with the scope of the metrology institutes (NIST, PTB, and NPL), they may at least contribute to solving this issue in the near future. Already today, there are a number of publications dealing with this subject and defining useful practices for a number of procedures such as measuring thrusts, measuring pressures, calculating pumping speeds, flow control, and various types of diagnostics.<sup>268–274</sup>

## F. Miniaturization

There are several driving forces behind the miniaturization of propulsion systems and, consequently, different approaches to miniaturization (cf. Fig. 14), all covered by the loosely defined term

micropropulsion. We will concentrate on miniaturized EP in the following and omit the miniaturization of single components (e.g., valves, sensors, or actuators) of otherwise conventionally scaled EP systems.<sup>275</sup>

- As satellites in the 100 kg class become more common, especially as parts of megaconstellations, smaller variants of established propulsion systems are needed.<sup>279</sup>
- Science missions that require very precise thrust control, low thrust noise, and small impulse bits, e.g., LISA-like missions<sup>280</sup> or gravity missions such as NGGM, may also find their needs met by scaled-down variants of existing propulsion systems such as RITs.<sup>281,282</sup>
- For satellites of the 1 kg class, such as CubeSats,<sup>283,284</sup> the scaling-down of existing systems may be insufficient. One can either use systems that are inherently small or systems

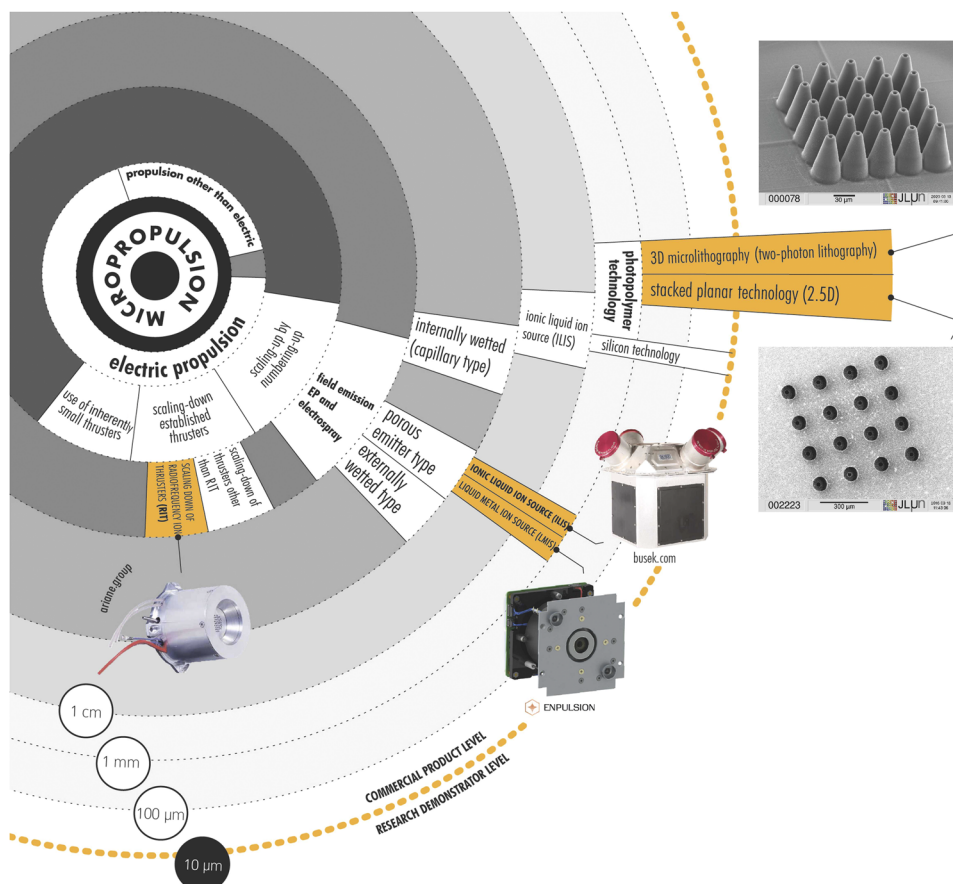


**FIG. 14.** Areas and concepts of electric space propulsion miniaturization, with emphasis on the fields covered in this paper, and selected examples of commercially available miniaturized propulsion systems. The labels 1 cm–10  $\mu\text{m}$  denote the sizes of the individual emitters employed. Images from ENPULSION,<sup>276</sup> BUSEK,<sup>277</sup> and ArianeGroup<sup>278</sup> used with permission.

that scale favorably upon miniaturization. In the latter case, which we shall consider micropropulsion in the narrower sense, methods from the technology of microelectromechanical systems (MEMS), which in turn were derived from microelectronics fabrication technologies, are used to fabricate very small emitters (microemitters), from which thrusters of an appropriate thrust level are then constructed by assembly of a sufficiently high number of microthrusters into arrays. This approach is known as “scaling-up by numbering-up.”

FEEP or electrospray propulsion is a concept that is well suited for the scaling-up by the numbering-up approach. The propellant, liquid metal in the case of FEEP or an ionic liquid in the case of electrospray emitters (also known as colloid emitters), is drawn from the reservoir by electrostatic forces. An electric field applied between the extraction electrode and the propellant [cf. Fig. 15(a)] leads to the formation of a Taylor cone at the orifice of the propellant feed line, and in the resulting strong local electric field, droplets or, ideally, ions are extracted from the propellant and accelerated by the extraction voltage, delivering thrust. More complex ion optics, involving several electrodes at different potentials, are possible. In MEMS technology, the extraction electrode does not have to be an external one,

since it is possible to integrate the extraction electrode by methods such as lithography, evaporation coating, and electroforming.<sup>285</sup>

A few words on the scalability of other conventional ion thruster concepts in comparison to the FEEP concept seem appropriate here, i.e., the HET, the GIE, the HEMPT, or the ECR concepts introduced in Sec. III A. All concepts including the FEEP concept have in common that ions are generated in a medium and then accelerated by an electrostatic field in order to generate thrust. In the case of the HET or GIE, the medium is a low-temperature plasma more or less confined in a vessel from which the ions are extracted. In particular, in the case of GIEs, the zones of plasma generation and ion acceleration are clearly separated. The corresponding separating boundary is somewhat washed out in HET, HEMPT, and cathodeless ECR thrusters. Equation (14) has already addressed aspects of the scaling of RITs. It is found that with the decrease in radius  $R$  of the plasma vessel, keeping up a plasma becomes inherently more difficult. The reasons are manifold and basically two effects stand out: First, the mean-free path of the electrons between elastic scattering events has to be considerably shorter than the diameter  $2R$  of the plasma vessel, which is hard to fulfill on miniaturization. Second, energy losses due to the interactions of the electrons and ions with the walls of the plasma vessel increase on miniaturization. Assuming a dominance of the surface losses, one may crudely say that the

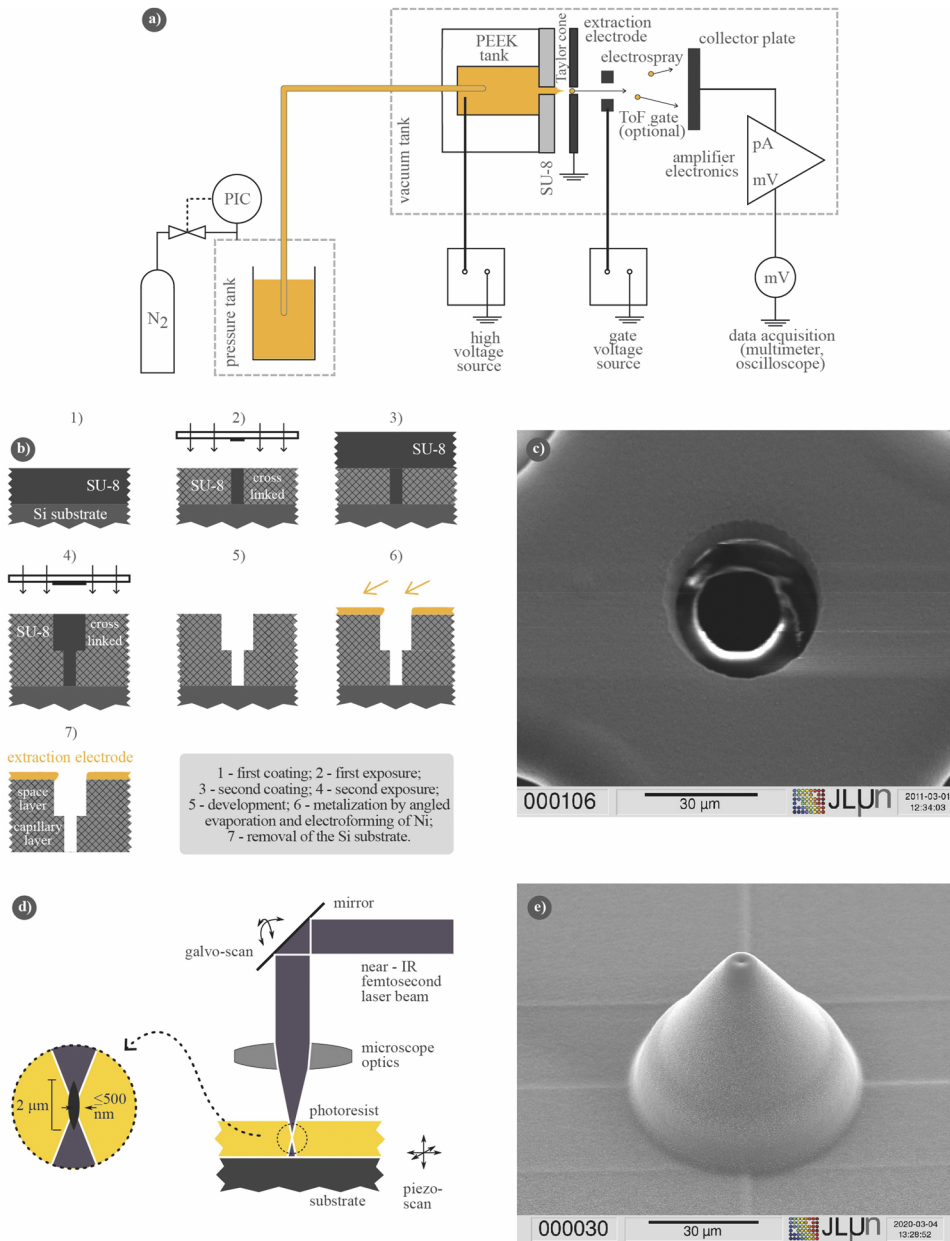


**FIG. 15.** (a) Schematic drawing of an electrospray emitter and the test setup for its electrical characterization, including a switchable gate for time-of-flight (ToF) measurements. Note the active propellant feed system driven by a controlled nitrogen pressure in the ionic liquid storage vacuum tank on the left hand side. (b) Process flow with stacked layers made by planar photolithography for the integrated fabrication of the capillary layer and spacer (extraction electrode support) layer, and SEM micrograph of a structure made this way. (c) Single emitter prepared by stacked plasma technology. (d) Illustration of the principle of two-photon microlithography. (e) SU-8 "volcano type" microemitter structure written using two-photon microlithography with a Nanoscribe PPGT in galvo mode.

efficiency is inversely proportional to the surface-to-volume ratio. Thus, if  $R$  is scaled by a factor  $\alpha$ , the efficiency also scales with  $\alpha$ . Considering that miniaturization implies changing the thruster sizes from the mm to the  $\mu\text{m}$ -scale, i.e., by several orders of magnitude, the RIT concept is not miniaturizable. Similar considerations hold for HET, HEMPT, ECR, and all other thrusters relying on a plasma confined by walls for ion generation. In contrast, ions in the FEPP concept are extracted out of the Taylor cone formed in the polarized liquid propellant. In particular, the voltage  $U_{\text{ext}}$ , where extraction of charged droplets and finally ions out of the Taylor cone occurs, scales

with the radius  $R$  of the capillary and the distance  $d$  of the extraction electrode as follows:<sup>286</sup>

$$U_{\text{ext}} \propto \sqrt{R} \ln\left(\frac{d}{R}\right). \quad (24)$$

It is reasonable to assume that  $d$  and  $R$  scale with the same scaling factor  $\alpha$  on miniaturization, and the ion current density extracted at  $U_{\text{ext}}$  is independent of  $\alpha$ . Noting that the same current  $I$  is realized by scaling the number of emitters  $N \propto \alpha^{-2}$ , one finds that the power  $P = U_{\text{ext}}I$  required for extracting the ion current  $I$  scales with  $\sqrt{\alpha}$ ,



and thus, the efficiency favorably scales with  $\alpha^{-1/2}$ . In addition, the FEEP concept is ideal for “scaling up by numbering up” due to the compactness of a single emitter, which is nothing but a simple capillary filled with liquid propellant (i.e., an integrated propellant reservoir) and an extraction electrode.

A key engineering challenge in achieving stable operations both for FEEP with liquid metal ion sources (LMISs) and for electrospray with ionic liquid ion sources (ILISs) is to provide for a sufficiently high fluidic resistance that the propellant experiences between the reservoir and the extraction orifice.<sup>287,288</sup> Since this is rather difficult to realize with externally wetted electrodes and difficult with internally wetted electrodes (see below), the first commercially successful thrusters were based on porous emitter materials, brought into shape by conventional machining techniques. Prominent examples for LMISs are the crown emitters from ENPULSION (Austria),<sup>276,289</sup> which use liquid indium as the propellant, and ILIS propulsion systems have been brought to the space market by BUSEK<sup>277</sup> (US). For ILIS systems, the activities of Alta in Europe with its Slit-FEEP system should also be mentioned.<sup>290</sup> It should be noted that the former still requires conventional neutralizer technology because only positive metal ions can be extracted from the liquid metal. In contrast, the ionic liquid consists of both anions and cations. Thus, neutralization when operating a field emission thruster with ionic liquids can be done in the so-called ambipolar mode. Two ways may be anticipated. Dependent on the grounding scheme, emitters with positive and negative polarity may operate in parallel, or the polarity of the individual emitter may be reversed repeatedly. In any case, this not only prevents the decomposition of the ionic liquid but most importantly eliminates the need for a separate neutralizer that unipolar EP always requires. Since neutralizers add to the complexity of the system and consume energy, while not delivering thrust, ionic liquid electrospray with a suitably chosen ionic liquid may have a competitive advantage in overall energy consumption, in particular, as both extracted anions and cations significantly contribute to the total thrust.

The fabrication of internally wetted ILIS emitters has been demonstrated by a number of institutions, such as MIT<sup>291,292</sup> in the US or the MicroThrust consortium<sup>287</sup> in Europe. These emitters were usually fabricated using methods and materials from silicon-based MEMS technologies, namely, photolithography, thin film deposition processes, and anisotropic etching of silicon by various methods. Silicon technology has the potential for a very large packing density of up to  $4 \times 10^6$  microemitters/cm<sup>2</sup>.<sup>293</sup> At such small geometric dimensions, however, the aspect ratio of the fluid-bearing structures is rather limited, and hence, it is difficult to achieve a sufficiently high fluidic resistance.

As an alternative to the silicon technology approach, the fabrication of microemitters from photostructurable polymers by conventional (planar) photolithography has been demonstrated.<sup>285,294</sup> The epoxy polymer SU-8<sup>295,296</sup> is a good candidate for such a process since it is very stable under harsh conditions that can be expected in space. SU-8 is a negative tone resist, that is, the exposed portions cross-link and remain after a development step. By combining multiple resist coating and exposure steps with a single final development step,<sup>297</sup> it is possible to stack SU-8 layers, although no undercut structures can be fabricated by this method.

Figures 15(b) and 15(c) show the process flow for fabricating a stacked layer electrospray emitter and a scanning electron

micrograph (SEM) of a structure realized this way, respectively. The accuracy of the positioning is given by the overlay precision of the mask aligner used for the photolithographic steps and is in the order of very few micrometers. When a third resist coating and an exposure step are included, the stacked layer technique can, for example, be used to create an extra trench between the propellant feed capillary and the surrounding extraction electrode support structures. Such a trench should mitigate the problem of unwanted wetting of the SU-8 surface by the ionic liquid,<sup>285</sup> which can lead to failure of individual microemitters or, if electrical shorts are created, even to the destruction of emitters. Another way of mitigating wetting is a treatment of the surface by sputter coating with PTFE or by covering it with a hydrophobic nanoparticle layer.<sup>285</sup>

An active propellant feed system, as depicted in Fig. 15(a), is essential for achieving emission from devices made by stacked planar photolithography.<sup>298</sup> The results on the DC characterization as well as on the characterization of the emission by time-of-flight (ToF) methods have been reported previously.<sup>299</sup>

The concept of realizing the core components of the electrospray emitters in an all-photolithography technique is even more powerful when employing two-photon lithography,<sup>300</sup> a 3D microlithography (even sub-micrometer lithography) method, instead of planar lithography.<sup>301,302</sup> The principle of two-photon lithography is illustrated in Fig. 15(d). A femtosecond laser with a wavelength of about 800 nm is used as photon source in the two-photon lithography apparatus. The laser beam is focused inside the resist layer using an inverted microscope system. Single-photon absorption cannot occur in the resist material, but two-photon absorption is possible. If the number of two-photon absorption processes that have occurred in a particular spot of the resist is above a certain threshold, the photochemical reaction of the resist is triggered. The probability of the two-photon process to occur is highest in the focus of the laser spot. Thus, the laser spot in conjunction with the dwell time at a certain position defines the volume element (voxel) where the resist is converted by the photochemical reaction. The lateral size of the voxel can be on the order of or less than the wavelength of the laser light, depending on the specific configuration. In the vertical dimension, the voxel extends over a distance on the order of a micrometer or a few micrometers. The laser focus can be scanned through a resist film or a resist puddle on a substrate to write micro- or even nanostructures. Two-photon lithography as a serial writing technique is thus inherently slower than planar photolithography but is free of the restrictions of planar lithography and may yield almost any shape in three dimensions.

The second generation of the two-photon lithography apparatus provides fast scanning of the laser beam by means of galvo mirrors in the microscope light path (“galvo mode”). This scanning method has cut the time needed to write structures by about two orders of magnitude compared to the first generation of instrumentation where scanning of the laser focus through the resist was achieved by moving the sample by means of piezoactuators. Several hours for writing a single emitter demonstrator structure have become a few minutes now.<sup>303</sup> As an example, the bottom image of Fig. 15(e) shows a microemitter. This structure was written in about four hours in galvo mode including a  $4 \times 4$  mm<sup>2</sup> base plate for mounting in the test setup.

The structure depicted in Fig. 15 was written in the “air gap” configuration into SU-8 resist on silicon dies pre-coated (before



dicing) with SU-8 resist. This configuration is marketed by Nano-scribe as the maskless lithography process, intended as a two-dimensional direct write laser method. However, it is also well suited for the creation of three-dimensional microemitter structures. We also chose SU-8 as resist material in the 3D lithography because of its robustness against harsh environments such as high-energy radiation in space. SU-8 is very suitable for high aspect ratio microlithography but was originally designed for 2D lithography. Thus, it remains to be seen whether it offers the same stability of the structures obtained by 3D lithography than more specialized resists. In any case, the high degree of design freedom offered by two-photon microlithography in combination with the prospect of high aspect ratios may be the key to tailoring the fluidic structures of the emitter in order to achieve sufficiently high fluidic resistance, which is mandatory for stable operation of FEEP (see also Fig. 14). The optimization of processing, trading-off resolution, and surface quality against writing speed, among others, is the subject of ongoing development work.

### G. Space electronics

The functioning and quality of an EP system depend to a large degree on its specialized electronics. In particular, such space electronics needs to be reliable and power efficient to the extreme as maintenance is not possible in space and the power available for specific tasks on the satellite, such as running a thruster, is more restricted than in the case of terrestrial applications. The heart of the electronics of an EP system is the so-called power-control unit (PCU), which distributes power to the ion thruster module. Typically, the PCU comprises a number of DC–DC converters, e.g., for low voltage (LV) and high voltage (HV) supplies of the grid system in the case of GIES, as well as DC–AC inverters, e.g., for rf-generation in the case of RITs or the AC power bus. Digital control electronics is based on  $\mu$ -controllers and/or field-programmable gate arrays (FPGAs). The PCU hosts the application software and performs thrust control as well as monitoring and failure detection functions.<sup>304</sup>

Details of the layout of the electronics required depend on the thruster type. For example, small DC input voltages (28 V up to 100 V) need to be converted into medium DC output voltages (300 V) in the case of HETs for ionization and acceleration of the ions.<sup>305</sup> In the case of GIEs, two DC–DC converters for PHV (about 2 kV) and NHV (typically below  $|-500|$  V) are needed for extraction of the ion plume. In addition, RITs require also a suitable RFG for supplying an AC-voltage in the range between 500 kHz and 5 MHz to ionize the propellant. The AC-voltage is provided as the output of a DC–AC inverter. In the following, we discuss the design and control of DC–DC and DC–AC converters used for ion engines. In this context, we will focus on concepts employing MOS-transistors for achieving high efficiency. This is crucial for two reasons: first, the power output of solar cells and batteries on the satellite is limited and, second, power loss at the converter stage complicates thermal management.

In the case of the RFG, the MOS-transistors of the DC–AC converter operate as ON/OFF switches and are periodically turned on and off within a switching cycle  $T_S$ . The value, size, and weight of passive filter components (inductors and capacitors) decrease with the increase in switching frequency  $f_S$ . From this vantage point, high

switching frequencies are advantageous. On the other hand, due to the fixed energy cost per switching cycle, power loss will linearly rise with  $f_S$  and therefore decrease converter efficiency. In order to minimize the size of passive components while at the same time avoiding high switching losses, soft switching techniques [zero voltage switching (ZVS) and zero current switching (ZCS)] are applied. In case of ZVS, transistor turn-on is performed, while the voltage across the switch is equal to zero. Turn-off is referred to as ZCS if the transistor current is zero at the switching instant. Compared to conventional pulse width modulation techniques, soft switching requires more advanced control strategies.

Due to its high output frequency in the lower MHz range, the RFG is realized as a resonant circuit inverter based on either a half-bridge or a full-bridge design given in the insets of Figs. 16(a) and 16(c), respectively. In the case of a full-bridge RFG,  $T_1$ ,  $T_4$  and  $T_2$ ,  $T_3$ , respectively, are turned on/off simultaneously [Fig. 16(b)]. For a half-bridge design,  $T_1$  and  $T_2$  are turned on alternately for half a switching cycle, connecting  $v_{H1}$  to either  $v_{in}$  or ground [Fig. 16(c)]. Hence,  $v_{out}$  is a pulsed voltage for a half-bridge design but a pure AC voltage for a full-bridge RFG,

$$\text{half-bridge RFG: } v_{out,HB} = v_{H1}, \quad (25)$$

$$\text{full-bridge RFG: } v_{out,FB} = v_{H1} - v_{H2}. \quad (26)$$

Hence, the rms value of  $v_{out,FB}$  is twice as high as  $v_{out,HB}$ . As a consequence, when using a full-bridge RFG, the number of turns of the thruster coil can be doubled, leading to half the coil current  $i_{th,FB}$ ,

$$i_{th,FB} = 0.5i_{th,HB}. \quad (27)$$

For both half-bridge and full-bridge RFGs, the phase angle  $\varphi$  between voltage and current is close to  $90^\circ$ .

The converter load needs to form a resonant circuit to enable low-loss switching. Since the thruster coil—assisted by the plasma—forms an ohmic-inductive load, this can be achieved by adding a series capacitor  $C_{res}$ . The square wave voltage  $v_{out}$  is fed to this resonant circuit, which acts as a low pass filter.<sup>306</sup> Its resonant frequency is somewhere between 500 kHz and 5 MHz and should be manually adapted to the thruster's size by changing the capacitance: the bigger the thruster diameter, the lower the resonance frequency  $f_0$ . The resulting current  $i_{th}$  supplied to the thruster is sinusoidal with low harmonic distortion.<sup>307</sup> As the output power of resonant converters is highest for  $f_S \approx f_0$ , the switching frequency is chosen equal to  $f_0$ . Switching losses are minimized when switching instants are placed near the zero crossings of  $i_{th}$ . Changes of the plasma load affect both the equivalent series resistance  $R_{th}$  and inductance  $L_{th}$  and therefore influence the resonance frequency  $f_0$ . Hence, both switching frequency and switching instants must be adjusted continuously. Digital control algorithms are realized using an FPGA.<sup>308–310</sup> A comparison of RFGs with different circuit design and adapted coil winding was started by Junker *et al.*<sup>311,312</sup> In order to take advantage of the doubled output voltage of the full-bridge RFG, the number of turns of the induction coil was doubled compared to the half-bridge operated thruster.

Figure 16(a) also shows performance mappings of the half-bridge and full-bridge topology. Especially at small flow rates, the full-bridge RFG requires less input power  $P_{DC}$ . Since the ohmic losses inside the RFG and along the transmission line are proportional to the rms current  $I_{th}^2$ , the conduction losses are considerably

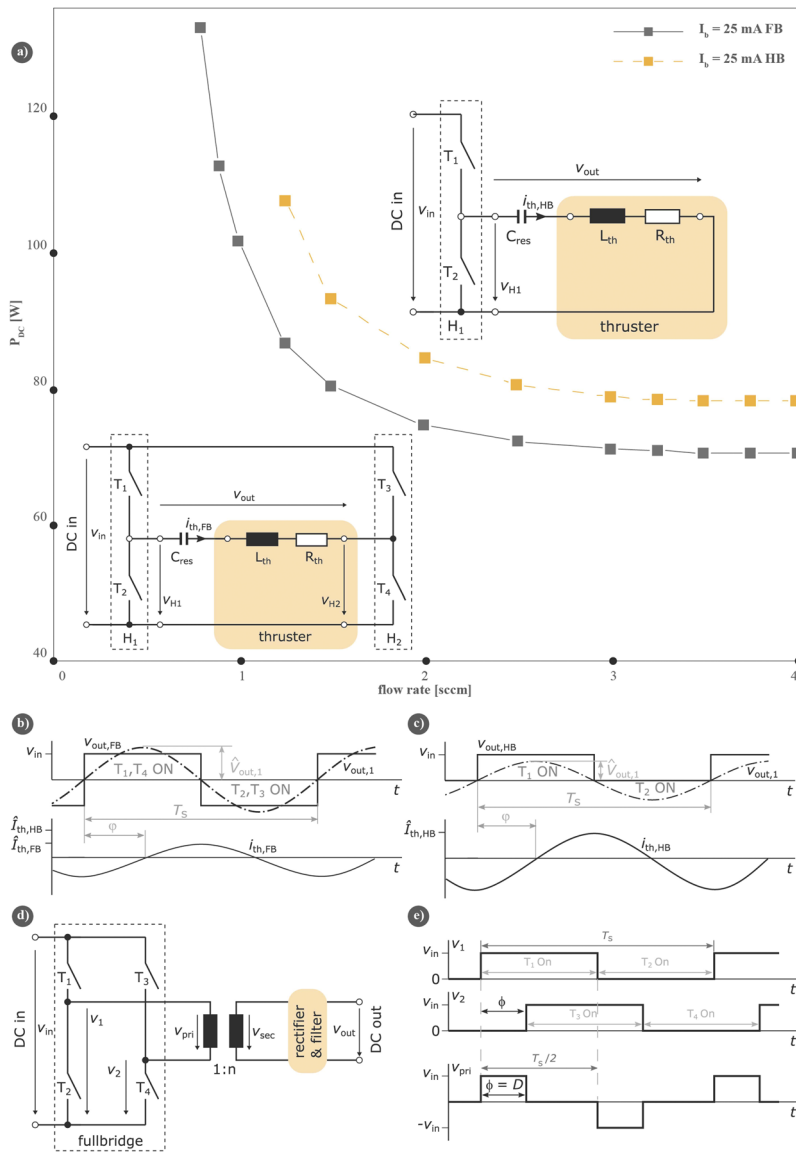


**FIG. 16.** (a) Two performance mappings of a RIT-type ion source operated with xenon at a constant extracted ion current of 25 mA using two different RFG architectures. In the case of the red curve, a half-bridge circuit configuration was used, and in the case of the black curve, a full-bridge circuit configuration was used. Both circuit diagrams are shown as insets. It should be noted that the full-bridge design consists of two half-bridges H1 and H2. The resonant circuit is formed with the thruster described by impedance  $L_{th}$  and resistor  $R_{th}$  representing the plasma and coil resistance. Output waveforms of square wave voltage  $v_{out}$ , fundamental component  $v_{out,1}$ , as well as coil current  $i_{th}$  for (b) full-bridge RFG and (c) half-bridge RFG. (d) Schematic design of full-bridge DC–DC converter comprised of 2 half-bridges with transistors T1, T2 and T3, T4; transformer; rectifier; and filter. (e) Phase shift  $\phi$ , time courses of  $v_1$  and  $v_2$ , and resulting transformer primary voltage  $v_{pri} = f(\phi)$ .

decreased due to the reduced coil current for the full-bridge circuit, which is advantageous, especially when operating at higher mass flows.

A schematic representation of a DC–DC converter is given in Fig. 16(d). Transistors T1, T2 and T3, T4, respectively, are turned on for  $T_S/2$  generating square wave voltages  $v_{H1}$  and  $v_{H2}$ . In contrast to the full-bridge RFG, the turn-on of T3 (T4) is delayed compared to the turn-on of T1 (T2) by phase angle  $\phi$ . Hence, a rectangular primary AC-voltage  $v_{pri}$  is generated, where  $\phi$  assumes the role of duty cycle  $D$  in converter equations. Its frequency is equal to the switching frequency  $f_S = 1/T_S$  of the transistors, whereas its rms value  $V_{pri}$  can be controlled by adapting the phase-shift  $\phi$  and hence  $D$ ,

$$V_{pri} = v_{in} \sqrt{2D}. \quad (28)$$

A high-frequency transformer increases the primary rms value to the required voltage level. Subsequently, the secondary AC voltage  $v_{sec}$  is rectified and filtered to form the HV DC output.<sup>313,314</sup> Moreover, full ZVS operation can only be achieved in a limited load and input-voltage range, unless auxiliary circuits are added.<sup>313,314</sup> Based on Fig. 16, a variety of modified circuit configurations and control algorithms have been reported.<sup>315–320</sup> Current research activities try to shift soft switching limits and use observer based methods to control secondary output voltage and current.<sup>321,322</sup>

## H. Electromagnetic compatibility

Due to the rapidly increasing use of HETs, GIEs, and newly developed thruster concepts as well as the high density of electronic

systems on a satellite ranging from communication electronics to the electronics of the propellant system, aspects of EMC are becoming increasingly important. Apart from the established systems, which have certainly proven their compatibility through successful use, aspects of EMC concern the novel EP concepts. All system components of an EP systems as well as all operational modes must be taken into account in a comprehensive EMC analysis. In the course of fast and economic development cycles, it is desirable to fall back on EMC investigations already in early stages of the development of electrical components for EP systems, since in later development stages, the availability of test possibilities decreases, but the costs to be incurred

increase reciprocally.<sup>324</sup> EMC issues as they concern the electromagnetic interaction between satellite system components are of great relevance for all satellite orbits.

To give an idea of the complexity of EMC issues on a satellite, Fig. 17(a) shows how system components may act as potential electromagnetic noise sources (RFG, PSCU, cables, plasma, etc.) and noise sinks (satellite components, beam current sensor, etc.). In order to ensure a flawless, reliable function of both the engine and the satellite system components, the potential electromagnetic interactions (coupling mechanisms) must be known and the strength of the rf interference currents as well as the emitted electromagnetic

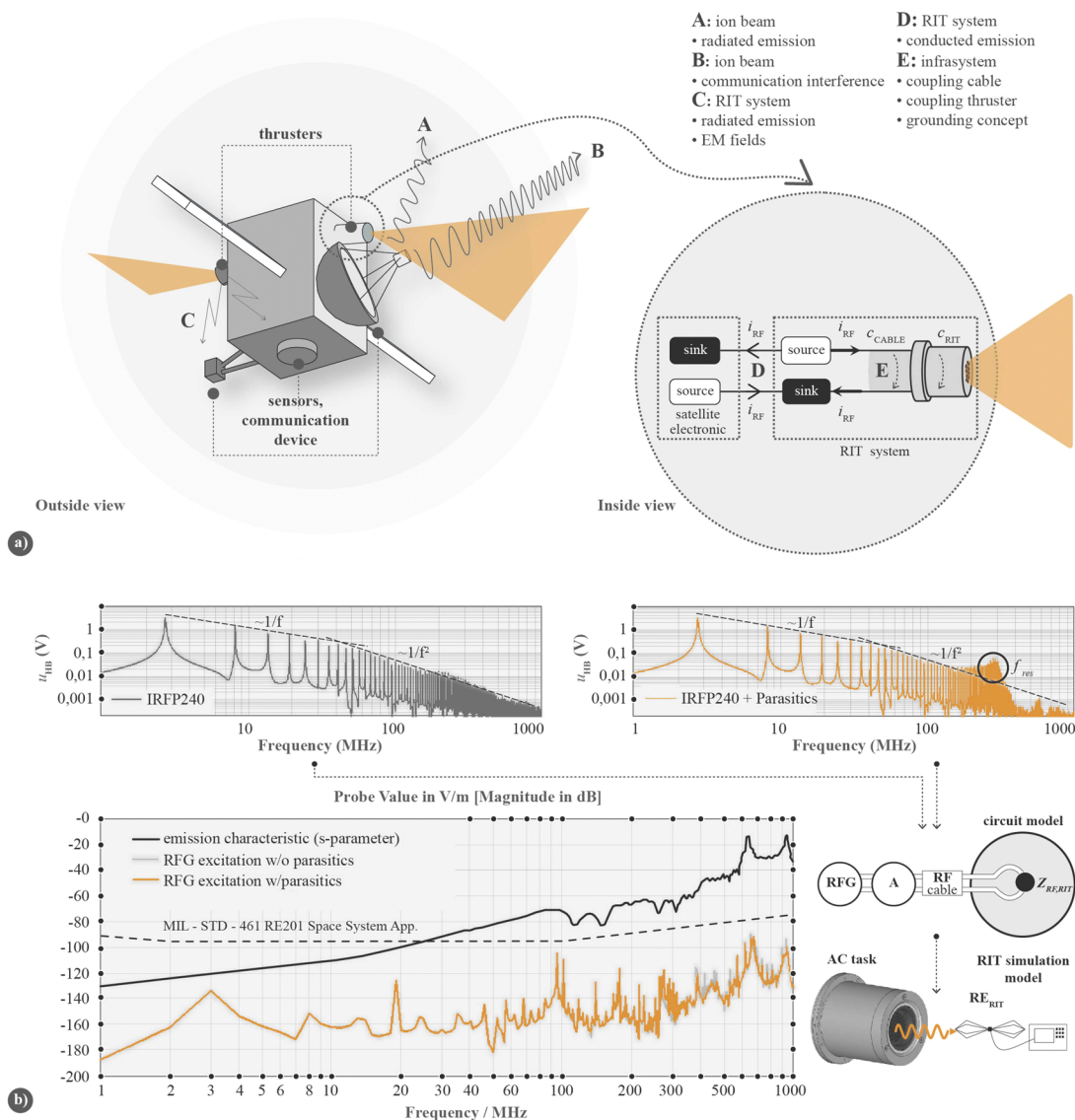


**FIG. 17.** (a) Schematic image of different sources of EMC perturbations on a satellite. (b) Electromagnetic interference analysis model and real emission spectrum of a radio frequency ion thruster.<sup>323</sup>

fields must be limited. For example, rf line currents may cause faulty sensor readings or may radiate electromagnetic fields via the coupling paths given by cables and parasitic capacitances, which act as antennas. The investigations of the interactions are usually first carried out with the help of 3D simulation models. First, the transfer function between interference sources and interference sinks is determined by simulation with a defined broadband rf input signal (a Gaussian pulse in the ns range). To determine the emission values, a real input signal is then used that originates from the electrical circuit simulation of the real engine system. By comparing the simulation results with measurements, the model can be optimized and generalized. The measured values shown in Fig. 17(b) were determined in a gigahertz transverse electromagnetic (GTEM) cell without an ignited plasma or beam extraction.

Specifically for European space applications, the European Cooperation for Space Standardization (ECSS), a standardization committee of the European Space Agency (ESA), has set up a catalog of specifications and requirements concerning EMC any space component should obey (current version as of February 7, 2020: ECSS-E-ST-20-07C Rev. 1). In a best case scenario, those guidelines would be followed starting very early in the development process of each individual component. The catalog is partly derived from and mainly based on the US standard MIL-STD 461. There are, however, some differences that are essentially due to the fact that the ECSS has strictly been developed for space environments, whereas the MIL-STD is not restricted to space, i.e., it can be understood as a more general standard and independent of the surroundings of the device-under-test (DUT). Both standards use the same nomenclature for categorization of the various test procedures, which correspond to the different coupling mechanisms. There are four main categories, which are each equipped with different experimental setups, limits, and testing procedures: (i) conducted emissions (CEs), (ii) radiated emissions (REs), (iii) conducted susceptibility (CS), and (iv) radiated susceptibility (RS). Each of those categories falls into sub-categories, distinguishing between electric and magnetic coupling (capacitive and inductive for the “conducted” cases). Depending on whether MIL or ECSS is referred to, those sub-categories differ by acceptable voltage, current, and power magnitude limits (or in the case of radiated emissions/susceptibility electric and magnetic field magnitudes at a given distance) and frequency limits. Typically, the magnitude limits for space applications are lower than those for terrestrial applications because the environment in space is electromagnetically cleaner, which intrinsically leads to less interference/compatibility issues. Frequency limits are also lower because of the free space loss in space. On Earth, where comparably short distances for radiated signaling are given, higher bandwidths, i.e., frequencies, are used to increase the possible bit rate. In space, however, higher frequencies are subject to higher free space loss  $a_{fs} = \frac{4\pi d^2 f}{c_0}$ , where the distance between sending and receiving antennas is  $d$ , the frequency is  $f$ , and the speed of light in vacuum is  $c_0 \approx 3 \times 10^8$  m/s. Hence, lower frequencies are chosen for space applications to avoid higher power consumption of the feed systems onboard the satellites.

Although there are standardized measurement procedures for electronic devices on spacecrafts in space, i.e., MIL-STD 461 and ECSS-E-ST-20-07C, these cannot be directly applied to electric thrusters in operation. The reason is that standard EMC test environments are rf shielded (semi)anechoic chambers, which typically

do not provide a vacuum environment. The latter is, however, essential for operating an electric thruster. Thus, dedicated test facilities need to be developed for this purpose. Vacuum systems for EP testing are usually large and therefore would require even larger anechoic test chambers, if they were to be integrated as a complete unit. Such an approach would be very expensive and unprofitable in the development phase of an engine. Furthermore, metallic vacuum chambers and vacuum pumps should be avoided in the test environment as they will falsify EMC measurements. The former reflect the electromagnetic radiation and the latter themselves emit radiation or allow external radiation to enter the test environment. Thus, the part of the vacuum system of the test facility where the operating thruster is located must be made of an electromagnetically transparent material, which is surrounded by the anechoic chamber.

A simplified EMC test setup, which was used to characterize the T5 ion thruster for the ARTEMIS satellite in the 2000s, is shown in Fig. 18(a). The DUT was placed on top and inside a cylindrical glass vacuum chamber of 40 cm in diameter and 1 m in length. The chamber was equipped with a turbomolecular pump on the bottom side. Furthermore, the chamber was located inside an anechoic chamber, and the antennas for EMC measurement were placed around the glass cylinder. This approach is certainly interesting for initial preliminary investigations but is certainly not ideal as the turbo pump was located within the test environment and was influencing the measurements. In addition, the vacuum conditions did not correspond to the conditions in space, so the characteristics at the nominal operating point in space were differing from those under test conditions. Figure 18(b) depicts exemplarily a state-of-the-art standard EMC test environment for operating EP systems. The interconnection of the EM transparent test chamber with a big vacuum facility facilitates measurements under more realistic vacuum conditions. Furthermore, the vacuum system is not located inside the anechoic chamber. However, the interface between the EM transparent test chamber and metal vacuum facility is still not EM-tight in this arrangement. Thus, electromagnetic radiation from the pumping system or even from outside the vacuum tank via its rubber seals may still leak into the test environment where the EP system is located and interfere with the EMC measurements. To prevent this issue, a special design of the vacuum system is built and tested at JLU [cf. Fig. 18(c)]. The issue of leakage via the interface between the vacuum tank and the test chamber is addressed by dividing the vacuum chamber into two parts. The first part connected to the anechoic chamber has no flanges or other weak points where electromagnetic radiation from the outside may enter. The second part holds the standard vacuum system with a large number of flanges for pumps, etc. Both parts are separated from each other by an EMC-tight partition wall consisting of panels of honeycomb structures. The partition wall does not allow electromagnetic radiation to pass but is transparent to gas particles. This allows us to establish vacuum conditions suitable for thruster operation in the first part of the vacuum chamber without violating the required damping conditions for external electromagnetic radiation.

## I. Radiation hardness

Radiation hardness of the electronic equipment concerns the interaction of satellite electronic components with high-energy



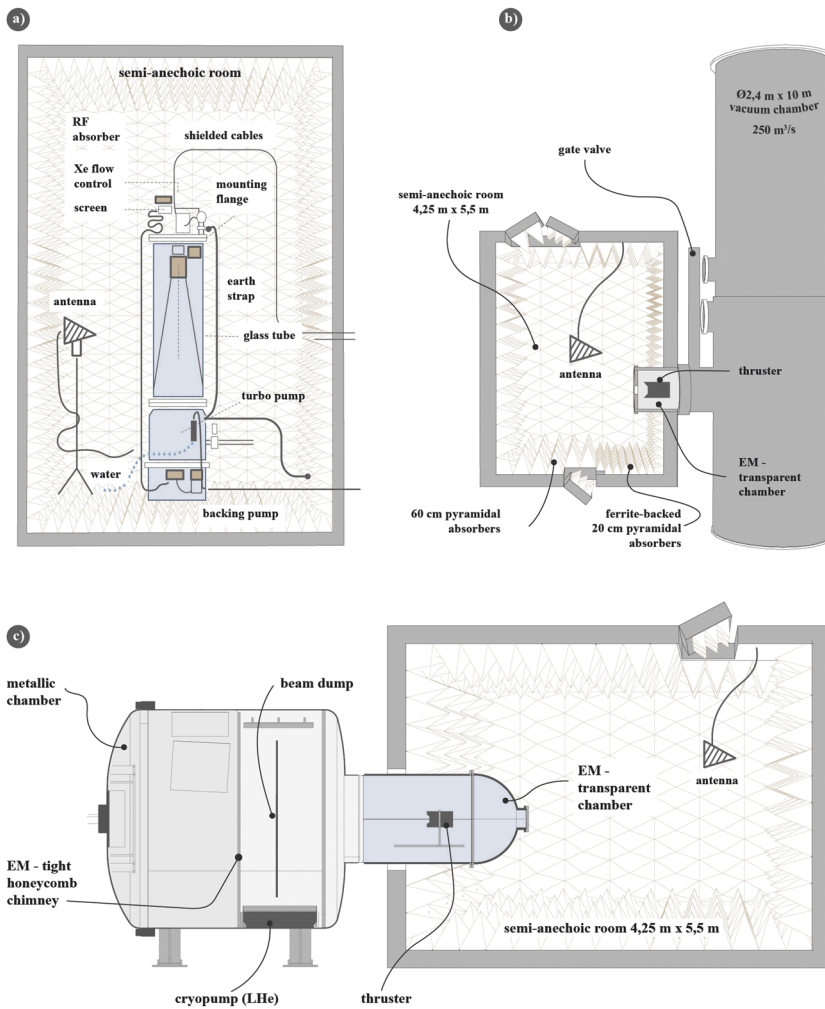


**FIG. 18.** (a) EMC test stand of DASA/MBB for testing the T5 ion thruster for the ARTEMIS satellite (figure based on Arbatskiy *et al.*).<sup>325</sup> (b) Test facility for EMC studies at The Aerospace Corporation (CA, USA).<sup>326</sup> (c) Conceptual drawing of the EMC test facility currently under construction at Giessen University. The vacuum chamber will be 3 m in length and 2.5 m in diameter, and the transparent cylinder will be 1.25 m in length and 1.0 m in diameter. The transparent cylinder part is located inside the adjacent anechoic chamber. The LHe cryogenic pump is an optional device and fulfills EMC requirements. It is the only vacuum pump on the EMC-side of the test chamber. All other pumps are located beyond a partition wall built of EM radiation tight honeycomb panels, which are transparent to gas particles.

particles or hard radiation coming from external sources such as the sun due to coronal mass ejections (CMEs) (cf. Fig. 19). The magnitude of these effects and the severeness of radiation hardness issues vary for the different types of orbits. It is of particular importance in EOR of satellites to GEO as this involves long sojourn times of the satellite in the Van Allen belts. We will address both issues in this section.

In addition, the functionality of a satellite, especially of its electronic components, may be severely affected by the interaction with hard radiation. For instance, EOR requires the satellites to pass slowly through the Van Allen belts, which leads to further challenges. The Van Allen belts, discovered in 1959 by the Explorer I and Explorer III missions, are regions of intense cosmic radiation (e.g., 10 MeV protons and 0.5 MeV electrons on average) [cf. Fig. 19(b)].<sup>18</sup> Thus, EMC investigations up to zettahertz range may become of interest, i.e., far beyond the standard range of a few GHz of EMC testing. In addition, the long retention times of satellites and their electronic components in the Van Allen belts

during EOR lead to high doses of high-energy particle radiation. This cosmic radiation comprises a solar component, which consists of mostly protons and a smaller fraction of lighter nuclei with kinetic energies of up to 1 GeV, and an isotropic component originating from galactic sources consisting of highly energetic photons, protons, as well as light and heavy nuclei up to uranium with energies of up to  $10^{20}$  eV.<sup>328</sup> The flux of the soft component is coupled to the solar activity cycle and shows fluctuations over one or more orders of magnitude (cf. Fig. 19).<sup>329</sup> The solar cycle has a period of roughly 11 years. Figure 19 shows the correlation between the number of sunspots and CMEs. The envelope of the number of sunspots was smoothed over 5 months. The number of CMEs per month is smoothed over a period of 13 months. Clearly visible is the correlation between the sunspot number and the number of eruptive protuberances. The CME data are from LASCO (Large Angle Spectrometric Coronagraph), a detection system on the SOHO satellite. LASCO data are automatically analyzed according to CME events using the CACTUS software.<sup>330,331</sup> The Earth's

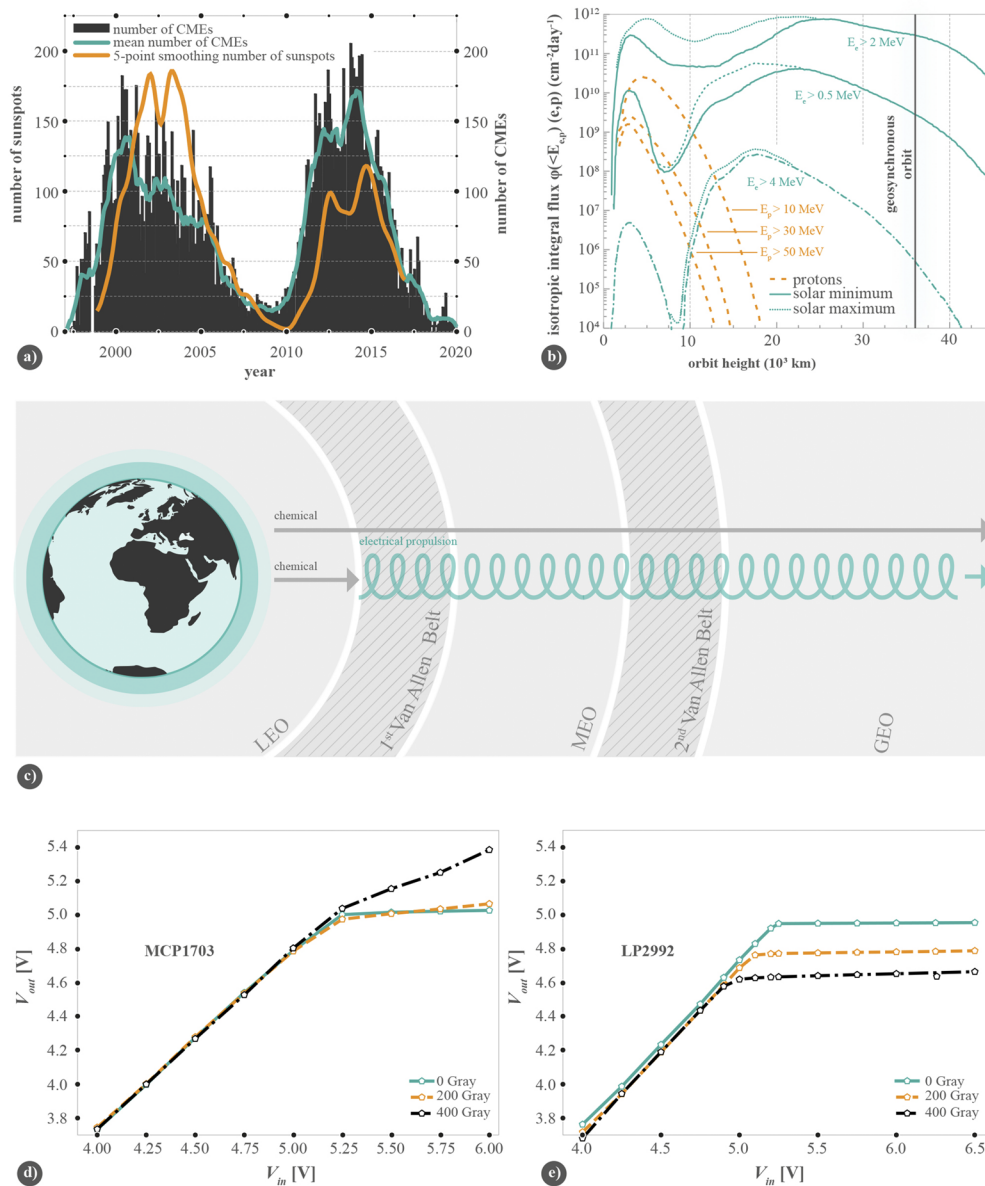


**FIG. 19.** (a) Correlation between sunspots and CMEs. (b) Integral flow of electrons and protons as a function of the distance to the earth in the equatorial plane (data taken from Ref. 327). The two maxima of the fluxes are called the two Van Allen radiation belts. (c) LEO, MEO, and GEO are basically separated by the two Van Allen radiation belts, the lower one between 3000 km and 6000 km above the Earth's surface mainly consists of 0.5 MeV electron particle radiation, and the outer one about 25 000 km from the Earth's surface consists of 10 MeV protons. Traditionally, GEO satellites were brought into orbit using a chemical rocket only, and significant cost savings are achieved by EOR, i.e., performing an orbit transfer from, e.g., LEO to GEO by EP. The drawback is the longer dwell time of the satellite in the Van Allen belts, leading to a higher exposure to high energy radiation. [(d) and (e)] Output vs input voltage of two commercially available LDO linear voltage regulators (5 V nominal regulation voltage and 150 mA load current) at different TID irradiation levels of a  $^{60}\text{Co}$  gamma source. MCP1703 (Microchip) displays the expected functionality up to 200 Gy TID but shows unacceptable regulation behavior for a TID dose of 400 Gy potentially harming devices supplied by the regulator from overvoltage. The LP2992 (Texas Instruments), on the other hand, shows a decrease in regulation voltage with the increase in TID but always provides an output within safe levels for the load. Note that the voltage drop and thus the power dissipation also increase with the increase in dose, which should be considered in the thermal design of the system.

atmosphere constitutes an effective shield for this primary cosmic radiation; however, its effects have to be considered in space applications, in particular, in the outer satellite orbits or deep space missions.

Radiation effects that arise in space include total ionizing dose (TID) and non-ionizing energy loss (NIEL) effects, single event effects (SEEs), radiation interference with structural parts (payloads and shielding parts), as well as effects on biological systems.

Depending on the type and energy range of the radiation and types of the exposed elements, one or more of those effects may dominate and lead to potential degradation or malfunction of space systems. Linear and analog devices, such as amplifiers, are predominantly affected by charge build-up due to TID. The function of devices that rely on high carrier mobilities due to good crystalline quality (such as reverse biased semiconductor junctions in, e.g., particle sensors or solar cells) is strongly affected by the damage of the crystal lattice due to displacements of atoms as a result of NIEL.<sup>332</sup> Digital electronic devices consisting of switching transistors are subject to SEE, which induces single bit errors due to single event upset (SEU) and transient (SET), latch-up (SEL), or even burn-out (SEB) of such cells. SEU and SET are considered “soft” errors and therefore mitigable, while SEL and SEB phenomena cause irreversible modifications of electronic structures.<sup>333</sup>

For the radiation tolerance qualification of electronic components in space systems, two approaches are taken:

- (i) The mitigation of detrimental effects induced by radiation on a system by its design. The choice of the foundry process, doping concentration, and distribution of the semiconductor bulk, passivation and choice of contact materials, as well as device packaging may improve the device’s performance notably. In addition, the functional sections in designs of digital circuitry in FPGAs (such as registers) may be tripled against single-event effects. Their outputs are then evaluated with a 2-out-of-3 majority decoder. Furthermore, all registers should have additional CRC bits for error detection and recovery, whereas counters should be laid out Gray-encoded. State machines can be hardened by assuring a lock-up-free behavior in case an invalid state is generated by SEE.<sup>334</sup>
- (ii) The qualification of components by accelerated and non-accelerated irradiation tests in comparable radiation fields. The latter is the method of choice for the qualification of custom-off-the-shelf (COTS) components, which marks a popular approach in modern space system designs.<sup>335,336</sup> All major space agencies maintain databases with test results of COTS component irradiations, such as NASA/GSFC.<sup>337</sup>

Test standards for predicting and measuring single event effects in electronic devices are advised in several standards, e.g., JESD89, JESD234, and ECSS-E-10-x.<sup>338–341</sup> However, the qualification of displacement damage in crystal lattices and the effects of TID are much harder to predict and depend on the specific design technology, the choice of semiconductor resistivity and doping distributions, as well as thicknesses of passivation layers and other surrounding passive materials, such as packaging, alloys of pads, and contacts. In general, all employed components should undergo accelerated irradiation tests for selected samples at least once per fabrication lot under well defined conditions (i.e., particle spectrum and doses/fluences). An example of such a TID characterization of COTS linear voltage regulators is given in Fig. 19.

The space radiation environment for characterization and qualification of radiation hardness of components can be simulated at JLU in several ways. A  $^{60}\text{Co}$ - $\gamma$ -source with a dose rate of about 30 Gy/h (at 1 m distance) and a neutron source as well as access to several German and trans-national proton and heavy-ion accelerator facilities are available for this purpose. These sources are routinely

used for the development and qualification of radiation-hard electronics for high-energy physics experiments, e.g., for the PANDA project.<sup>342,343</sup>

## J. SC/EP interaction

A major issue of spacecraft EP interaction is related to the interaction of the neutralized ion plume with parts of the thruster itself,<sup>129,344–352</sup> other components of the spacecraft,<sup>353–355</sup> other spacecrafts in the case of debris removal employing EP for momentum transfer,<sup>92</sup> or with parts of the test facility in the case of terrestrial testing.<sup>265,356</sup> One has to distinguish between the damage induced by material sputtering by the ion beam itself and effects due to the deposition of either the propellant itself or its sputter products on surfaces of the spacecraft. Examples of internal sputter damage are grid erosion in the case of RIT and Kaufman-type engines<sup>345,347,348</sup> or channel erosion in the case of Hall thrusters.<sup>344,346,349</sup> External erosion of other components may occur in the case of solar panels.<sup>355</sup> Deposition of material may occur when propellants, other than noble gases, such as iodine (which is employed as an alternative to xenon in the case of ion thrusters), or indium and cesium metal (which are employed as propellants in FEEP)s condensate on the surfaces of the spacecraft.<sup>357</sup>

Sputtering of materials by ion beams has been widely studied in terms of impinging projectile ions and target materials covering a wide range of projectile energies ranging from a few eV to MeV.<sup>361</sup> The underlying microscopic processes taking place depend on the species involved in the sputter process and determine the degree of physical and chemical effects occurring. Physical sputtering takes place solely by momentum transfer from the impinging projectiles to the target atoms and plays a role for all target materials and incident particles with energies above a certain threshold of about 100 eV. Chemical erosion is initiated by chemical reactions between thermalized neutral species from the gas phase with surface atoms. In contrast, chemical sputtering is a process where the ion bombardment promotes a chemical reaction between the projectile and target atoms, producing new chemical species that are weakly bound to the surface and hence are easily desorbed into the gas phase.<sup>362</sup> Such chemical processes may play an additional role, when employing a chemically reactive propellant such as iodine or when reactive material is sputtered off by impinging ions of the plume and deposited elsewhere.

The foremost effect of sputtering is the removal of the target material. It is characterized by the sputtering rate  $R$  given as an etch depth  $\Delta h$  per sputtering time  $\Delta t$  in units of nm/s. Obviously, the sputtering rate not only depends on the atomic or ionic species involved as the projectile and target but also on the ion energy and the geometry of the experiment. The underlying microscopic mechanisms are shown in Fig. 20(a).<sup>358,367,368</sup> Physical sputtering is caused by the momentum and energy transfer of the projectile ions to the target atoms in the top atomic layers of the material. Three regimes of sputtering by elastic collisions need to be distinguished, which occur with the increase in projectile energy:

- (i) the single knock-on regime where the projectile in a first scattering event is redirected toward the surface where it transfers recoil energy to an atom close to the surface [Fig. 20(b)]. This energy is sufficient to overcome the surface binding energy  $U_0$  of this atom.

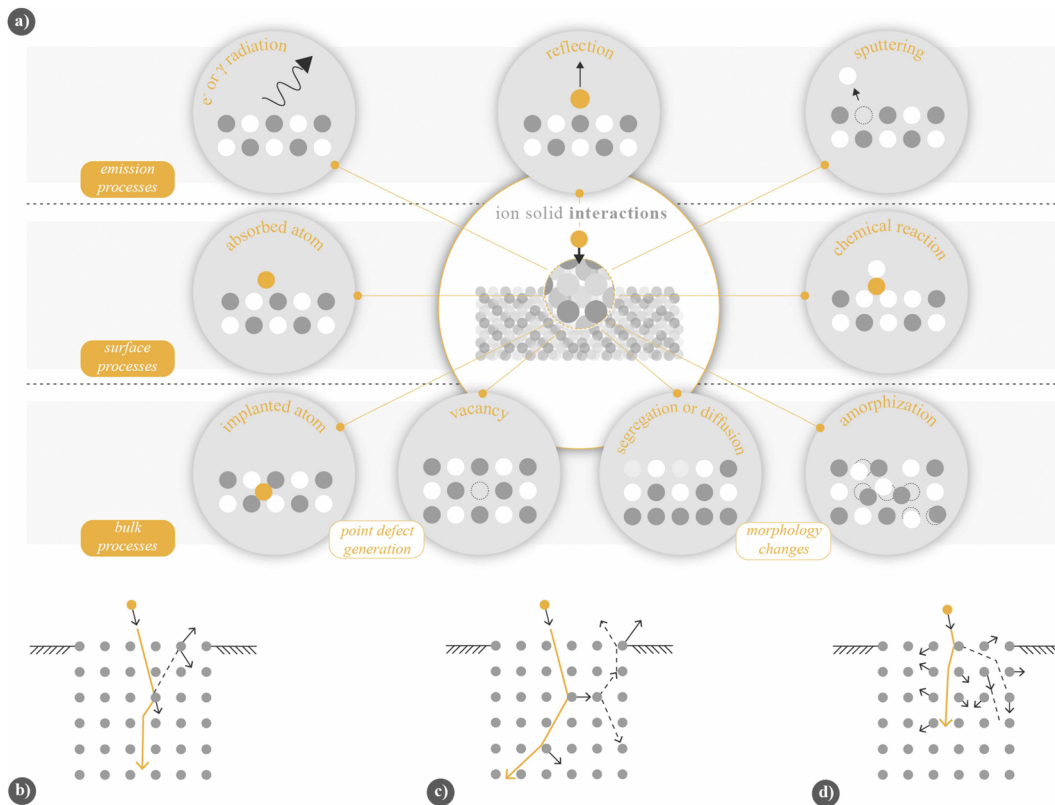


**FIG. 20.** (a) Possible interactions of an ion beam with matter. Three regimes of sputtering by elastic collisions: (b) single-knock-on regime, (c) linear cascade regime, and (d) spike regime.

- (ii) the linear cascade regime where atoms in the interior are knocked off their equilibrium positions and possess enough energy to generate a recoil cascade, leading to the ejection of some of the atoms from the surface. The density of recoil atoms is sufficiently low; therefore, knock-on collisions dominate, and collisions between moving atoms are infrequent [Fig. 20(c)].
- (iii) At even higher projectile energies in the so-called spike regime, the density of recoil atoms is so high that the majority of atoms in the impact volume is in motion and no longer bound [Fig. 20(d)]. However, it should be noted that some of the energy of the projectile ion striking the surface is lost to the creation of secondary electrons (electronic energy loss) in addition to sputtered target atoms (nuclear energy loss).

The ion energies in the plume of ion thrusters (except for some FEEPs) are typically smaller than 5 keV ( $RIT \leq 2$  keV,  $HET \leq 700$  eV, and  $FEEP \leq 10$  keV) and mainly cause sputtering in the single knock-on regime or in the linear cascade regime; thus, secondary recoils make up most of the sputtered material. These dependencies are more accurately described by introducing the sputtering yield  $Y$  as the number of target atoms sputtered per incident ion.<sup>358,369</sup> In regimes of interest in the context of ion thrusters, the number of

recoils and, thus, the sputter yield are proportional to the amount of nuclear energy deposited per unit depth. Both types of collisions involved, ion–atom as well as atom–atom, require accounting for screening effects in the scattering event. As different degrees of approximation can be made when calculating the corresponding scattering cross sections, somewhat different expressions for the sputtering yield can be found in the literature.<sup>370</sup> However, for low projectile energies ( $E < 5$  keV), the sputtering yield  $Y$  is linear in ion energy  $E$ .<sup>358,371,372</sup> At very low ion energies ( $E < 1$  keV), some authors say that  $Y$  is proportional to  $\sqrt{E}$ .<sup>372</sup> Seah gave the following simplified equation for the total sputtering yield for ion energies  $E < 1$  keV for a monoatomic target,

$$Y = \frac{3}{4\pi^2} \frac{4M_t M_p}{(M_t + M_p)^2} \cdot \beta \cdot \frac{E}{U_0}, \quad (29)$$

where  $M_p$  and  $M_t$  denote the atomic masses of the projectile ion and the target atoms, respectively. The parameter  $\beta$  is a function of mass ratio  $M_t/M_p$  and the geometry of the experiment. This simplified equation reveals two major dependencies of  $Y$ , which should hold as a rule of thumb. First,  $Y$  is proportional to the energy transfer factor  $\gamma = \frac{4M_t M_p}{(M_t + M_p)^2}$  of the elastic collision between the projectile ion and the target atom, which is largest for equal masses. Second,  $Y$  is inversely



proportional to the surface binding energy  $U_0$ , i.e., the more loosely bound the target atoms are, the higher the yield is. For metals,  $U_0$  corresponds to a first approximation to the heat of sublimation. This dependence is reflected in the sputtering yields found for the different monoatomic targets in collision with low energy ions ( $E < 1$  keV), as shown in Fig. 21(a), at normal incidence ( $\theta = 0^\circ$ ).<sup>373</sup> The data of Rosenberg and Wehner among many others also reveal the linear dependence of the sputter yield on ion energy for  $E < 1$  keV. It should be noted that the threshold of sputtering can be very low, a few electron volts only, and will strongly depend on the morphology of the surface.<sup>374</sup> In general, the sputtering yield is somewhat higher for rough surfaces than for flat ones at  $\theta = 0^\circ$  and vice versa for large angles  $\theta > 45^\circ$ .<sup>375</sup> Furthermore, for high ion beam energies, the primary ions penetrate deeper into the sample; correspondingly, less of their energy is deposited close to the surface, and sputtering yield  $Y$  increases less than linearly with  $E$  or even decreases again.<sup>376</sup> The total sputtering yield  $Y$  is also a function of the angle of incidence  $\theta$  referenced with respect to the sample normal in the case of

amorphous or polycrystalline materials, which are quasi-isotropic on the mesoscopic scale, as follows:

$$Y(\theta) = Y(0) \cdot (\cos \theta)^{-f} \cdot \exp \left[ f(1 - (\cos \theta)^{-f}) \cdot \cos \theta_{\text{opt}} \right], \quad (30)$$

where  $f$  is a function of mass ratio ( $M_t/M_p$ ) and  $\theta_{\text{opt}}$  is the optimum incidence angle.<sup>359,369</sup> Typical values of  $f$  lie in the range between 0.7 and 2.5.<sup>358</sup> The exponent  $f$  is independent of ion energy for  $E > 1$  keV. At ion energies below 1 keV, the exponent  $f$  is inversely proportional to the surface binding energy  $U_0$ .<sup>377</sup> As an example, Figs. 21(b) and 21(c) show the energy and angular dependence of the sputtering yield of Mo under incident Xe ions with energies comparable to those of Xe in the plume of ion thrusters.<sup>359</sup> The data suggest that a linear description of  $Y(E)$  is indeed reasonable for Xe ions with ion energies between 100 eV and 1 keV. Furthermore, the  $Y(\theta)$ -curves at constant  $E$  follow Eq. (30) up to a maximum angle  $\theta_{\text{opt}}$  and then drop to zero, approaching grazing incidence. It should be noted that the angular dependence of the sputtering yield

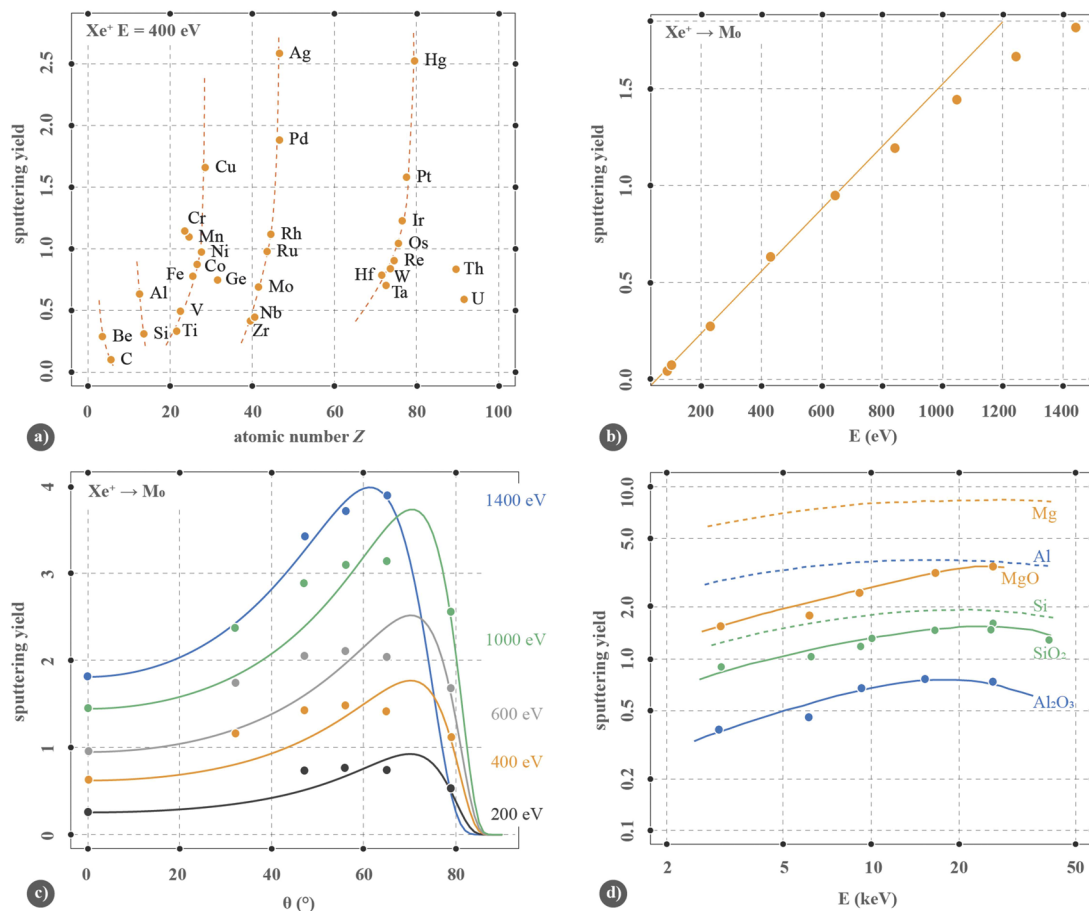


**FIG. 21.** (a) Experimentally determined sputter yields for 400 eV  $\text{Xe}^+$  ions bombarding target material of different atomic numbers at normal incidence (data taken from Ref. 358). (b) Energy dependence of the sputter yield of Mo for  $\text{Xe}^+$  ions at normal incidence (data taken from Ref. 359). (c) Dependence of the sputter yield on the incidence angle of the  $\text{Xe}^+$  ions for various ion energies. The curves are fitted using Eq. (30) (data taken from Ref. 359). (d) Sputtering yields of Si, Al, Mg, and their corresponding oxides as a function of sputtering energy (data taken from Ref. 360).

$Y(\theta)$  may be significantly different in the case of single-crystalline materials. The reason is the occurrence of ion channeling within the crystalline structure, i.e., at certain angles  $\theta$ , the ions can travel parallel to specific crystalline directions, for incidence parallel to crystal planes and/or low index crystal axes, without hitting surface atoms. The energy deposited near the surface decreases substantially when channeling occurs, reducing the sputtering yield significantly.<sup>378–380</sup> Channeling effects are the largest at high ion energies. Furthermore, when sputtering multicomponent samples, the sputtering yield of one component is often larger than those of the other components. The stoichiometry of the material in the vicinity of the surface is altered as a consequence. This phenomenon is denoted as differential or preferential sputtering.<sup>381,382</sup> In the case of binary materials  $A_nB_m$ , the observed surface enrichment of the one component often may be deduced by simply considering the ratio of the sputtering yields of two elemental compounds expressed in terms of their atomic masses and surface binding energies,

$$\frac{Y_A}{Y_B} = \frac{n}{m} \left( \frac{M_B}{M_A} \right)^{2k} \left( \frac{U_{0B}}{U_{0A}} \right)^{1-2k}, \quad (31)$$

where  $0 < k < 0.2$ .<sup>369,382</sup> It is clear that the sputtering yield of element A is favored if  $M_A < M_B$  or  $U_{0A} < U_{0B}$ . Tables listing the differential sputtering yields of multicomponent samples can be found in the literature.<sup>367,382</sup> Figure 21(d) demonstrates that the situation is not quite that simple: Typically, preferential sputtering of binary metal oxides such as  $Al_2O_3$ ,  $SiO_2$ , or  $MgO$  by noble gas ions in vacuum leads to a reduction of the material, i.e., preferential sputtering of oxygen; nevertheless, the sputtering yields of Al, Si, and Mg are higher than those of the corresponding oxides.<sup>383</sup> This behavior is related to differences in bonding, e.g., a metallic bond in Al or Mg and a covalent bond in Si, in contrast to an ionic bond in the corresponding oxide.

Another feature of ion beam sputtering is the alteration of the surface morphology or microstructure, and this holds for monoatomic samples as well as multicomponent samples. Many examples show that the surface morphology arising in the etching process depends on the properties of the ion beam, e.g., its energy and angle of incidence, as well as on the target material, e.g., crystal orientation or defect structure.<sup>367,369,384,385</sup> The knowledge of the energy and angular distribution of the sputtered atoms is of great importance as it may lead to unwanted material deposition of absorbing layers on satellite components such as solar panels, reducing their efficiency or of conducting layers, leading to short circuits of electronics. The spectral distributions in terms of the (polar) emission angle and the (kinetic) emission energy of sputtered species reflect, to some degree, the atomistic processes occurring during the dissipation of the projectile ion's energy in the solid and the sputtering event. Therefore, they differ for the single knock-on regime [Fig. 20(b)] and the linear cascade regime [Fig. 20(c)]. Furthermore, energy and angular distribution depend on the target material, e.g., whether it is isotropic as in the case of polycrystalline or amorphous material or the density of atoms varies for different spatial directions as in the case of single crystals. Already, the first measurements of energy spectra of the sputtered material revealed the athermal nature of the sputtering process.<sup>386–388</sup> Generally, the sputtered flux consists of various different species. In addition to neutral and ionized atoms, clusters of a few atoms and molecules in the case of

alloy targets as well as excited atoms may be present. The energy and angular distributions of these sputtered species will differ sometimes considerably.

Nevertheless, the model of Sigmund developed for the linear cascade regime and isotropic target media yields some microscopic insight.<sup>389</sup> If an atom with kinetic energy  $E_{int}$  involved in the linear cascade process approaches the surface from within the target under an angle of incidence  $\theta_{int}$  to the surface normal and the fraction of its kinetic energy originating from its velocity component perpendicular to the surface is larger than the surface binding energy  $U_0$ , then the atom is emitted [see also Fig. 22(a)]. The energy  $E_{em}$  of the emitted atom and the emission angle  $\theta_{em}$  with respect to the surface normal are given by

$$E_{em} = E_{int} - U_0, \quad (32)$$

$$E_{em} \cos^2 \theta_{em} = E_{int} \cos^2 \theta_{int} - U_0. \quad (33)$$

The differential sputtering yield of atoms sputtered with emission energy  $E_{em}$  into the solid angle  $\Omega$  around the polar emission angle  $\theta_{em}$  then reads

$$\frac{\partial^3 Y}{\partial E \partial \Omega^2} \propto Y(E, \theta) \cdot \frac{E_{em}}{(E_{em} + U_0)^{3-2m}} \cdot \cos \theta_{em}, \quad (34)$$

where  $Y(E, \theta)$  is defined above and  $m$  characterizes the interatomic potential  $V(r)$  used in the description of the atomic collisions. The energy distribution

$$F(E_{em}) = \frac{E_{em}}{(E_{em} + U_0)^{3-2m}} \quad (35)$$

peaks at  $E_{em, peak} = U_0/(2(1 - m))$ . For  $m = 0$ , it holds  $E_{em, peak} = U_0/2$  and the distribution tails off with  $E_{em}^{-2}$ . Usually fitting of measured energy distributions  $F(E_{em})$  to experimental data yields  $m > 0$ . Similarly, one tends to fit the measured angular dependence of the sputtering yield  $\frac{\partial Y}{\partial \Omega}$  to a  $\cos^m \theta_{em}$ -functional dependence with  $y$ -values frequently larger than 1.

Figure 22 also depicts typical measured spectral distributions as a function of emission energy and emission angle. Graph (b) depicts the energy spectra of neutral Ag atoms and higher cluster  $Ag_n$  sputtered from a polycrystalline Ag target, employing 5 keV  $Ar^+$  ions impinging under  $\theta = 45^\circ$  to the surface normal.<sup>363</sup> The relative scaling of the experimental curves was arbitrarily selected for clarity. The dotted lines are power law fits to the tail of the distributions and reveal that it deviates from the  $E_{em}^{-2}$  expectation. Furthermore, the steeper the tailing off, the larger the clusters. However, all energy distributions exhibit almost the same  $E_{em, peak}$ , yielding an  $U_0$  of about 2.2 eV. It should be noted that the emission energies of almost all Ag clusters are below 100 meV. This indeed confirms that the main danger of the sputtered material lies in the deposition of material and not additional sputtering. Figures 22(c) and 22(d) show polar diagrams of the differential sputtering yield of amorphous Si and polycrystalline Au, respectively.<sup>364</sup> The measurements were performed with 1 keV  $Ar^+$  ions at normal incidence ( $\theta = 0^\circ$ ) and oblique incidence ( $\theta = 45^\circ$ ). Typical features are revealed. At normal incidence, the differential sputtering yield of amorphous Si follows as anticipated the cosine-behavior quite well and shows the specular behavior when going to oblique incidence. In contrast to the data of polycrystalline gold with a preferential (220) orientation, it exhibits additional features due to channeling effects. The channeling effects

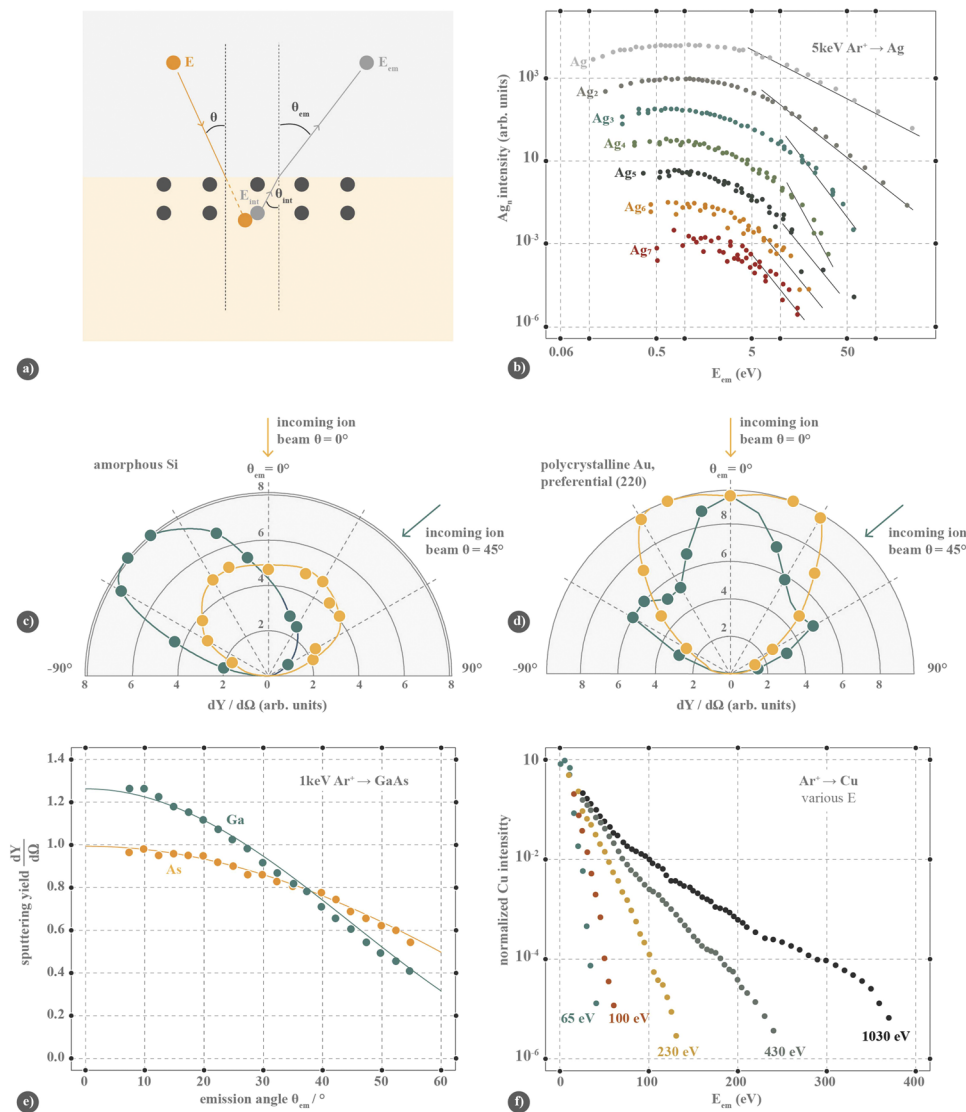


**FIG. 22.** (a) Scheme of a projectile ion of energy  $E$  hitting the surface under incident angle  $\theta$  to the surface normal. It dislocates an ion of energy  $E_{\text{int}}$  in the interior of the solid, which approaches the surface under an angle  $\theta_{\text{int}}$  to the normal. The sputtered ion overcomes the surface barrier and is emitted with energy  $E_{\text{em}}$  under an angle  $\theta_{\text{em}}$ . (b) Kinetic energy distributions of neutral Ag atoms and  $\text{Ag}_n$  clusters sputtered from a polycrystalline silver target by 5 keV  $\text{Ar}^+$  ions (data taken from Ref. 363). Polar diagrams of the angular distributions of sputtered atoms by bombardment with 1 keV  $\text{Ar}^+$  ions at normal incidence and under  $45^\circ$  incidence angle (c) from a polycrystalline Si target and (d) a polycrystalline Au target with preferential (220) orientation parallel to the surface normal (data taken from Ref. 364). (e) Polar angular distribution of Ga and As atoms sputtered from a crystalline GaAs surface using 1 keV  $\text{Ar}^+$  ions at normal incidence (data taken from Ref. 365). (f) Emission-angle integrated energy spectra of neutral Cu atoms sputtered from elemental Cu by normal-incidence  $\text{Ar}^+$  ions of the indicated energies (data are taken from Ref. 366).

are even more pronounced in the case of single crystalline targets underlining again the importance of the sample morphology in the sputtering process.<sup>390,391</sup> In the case of alloys, the situation becomes even more complex, as shown in Fig. 22(e), where the angular distributions of the atomic species of Ga and As are plotted, which result from the sputtering of a (100) single crystalline GaAs with 1 keV  $\text{Ar}^+$  ions at normal incidence.<sup>365</sup> The differential sputtering yields of both atomic species exhibit a  $\cos^\gamma$ -dependence with  $\gamma = 2$  and 1 for Ga and As, respectively. At first sight surprisingly, no features due to channeling are visible. The reason is that the surface region of the crystalline GaAs becomes amorphous under ion bombardment. This structural phase change is accompanied by segregation effects, which lead to the difference in  $\gamma$ -values.

In the single knock-on regime, i. e., at low bombarding energies, the energy and angular distributions of emitted species may

change drastically as compared to the linear-cascade case. While under the conditions of linear collision cascades, energy spectra are typically found to agree roughly with the theoretical predictions, this is no longer the case at very low impact energies. In energy spectra recorded under such conditions, the peak of the energy spectra tends to shift to lower energies and the width of the distribution becomes narrower, as shown in Fig. 22(f). With the decrease in  $\text{Ar}^+$  impact energy, the emission curves exhibit a steeper decline, and the steepness is related to the maximum energy an  $\text{Ar}^+$  ion can transfer to a sputtered Cu atom for a given  $\text{Ar}^+$  energy. The falloff is roughly exponential over a wide emission-energy range.

If a target is bombarded with chemically reactive species, possible chemical reactions have to be taken into account and one talks of chemical sputtering. The impact is not *a priori* clear.<sup>392</sup> On the one hand, chemical reactions between the target and projectile atoms

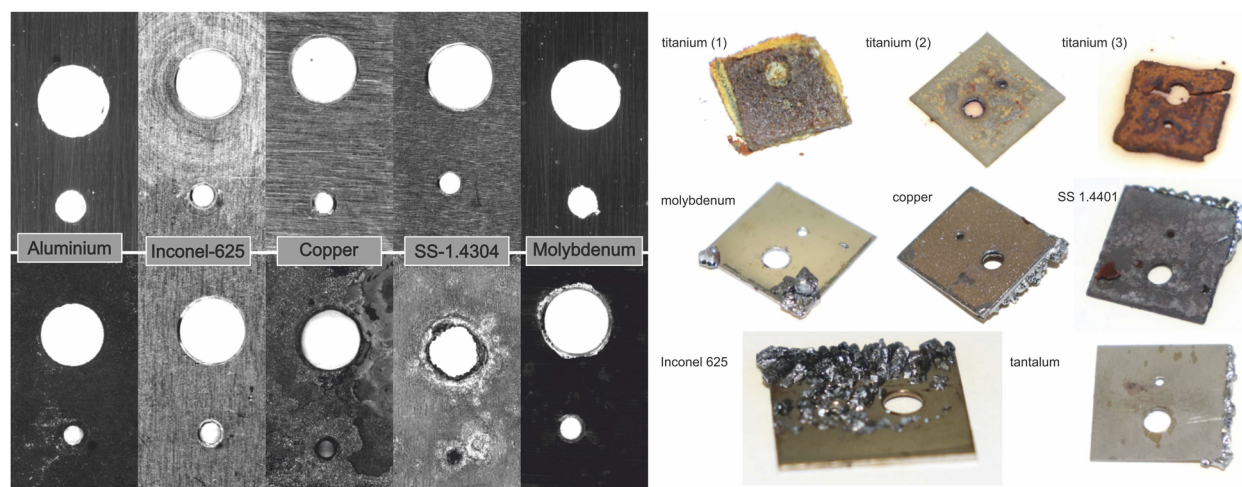


**FIG. 23.** Material samples that were exposed to iodine under atmospheric pressure. For this purpose, resublimated iodine (a few grams, purity > 99%) together with a metal sample ( $10 \times 10 \times 1 \text{ mm}^3$ ) was placed in a lockable glass vessel. The black-and-white photographs refer to samples that were exposed to iodine for several months at room temperature (upper row before exposure and lower row after exposure); the colored pictures show samples that were exposed to iodine at about  $80^\circ\text{C}$  for a few days (all after exposure). Holes of 0.5 mm and 2 mm diameter were drilled into the samples. As expected, there is a strong visual change in aluminum and copper, but the influence on the degradation of the holes was less pronounced than expected. Unexpected was the behavior of titanium; here, a strong growth of a layer on the surface was observed. Titanium (1) shows the sample after removal from the iodine atmosphere, titanium (2) shows the original sample after removal of this layer, and titanium (3) shows the grown layer (backside). Together with the titanium iodide compounds found in the mass spectrum of the ion beam when using a titanium grid, it can be clearly stated that titanium is conceivably unfavorable for iodine-powered engines. There are also clear differences among the stainless steels, 1.4304 shows clear signs of corrosion in the area of the drill holes, while 1.4401 was attacked less strongly—although not negligibly. Inconel 625 shows surprisingly a significant growth of iodine on its surface. This effect has been seen in other samples partly at the edges, but almost not in the planar part. All samples originating from the plate material were obtained from Goodfellow.

may lead to product species that are more loosely bound to the surface and more easily removed by the impinging ions, i.e., the sputtering yield of the target material is enhanced. In cases where the newly formed compounds possess a stronger bonding to the surface, a decrease in the sputtering yield compared with that of the original target is observed. Similar effects may also occur when bombarding the target with non-reactive ions in a reactive gas atmosphere. The chemical erosion process does not only depend on the ion–target–atom combination but also on the ion fluxes and energies. Only if the number of reactive atoms arriving at the surface is comparable or larger than the number of atoms removed by sputtering, a compound layer can be formed and chemical sputtering plays a role. In such a situation, a chemically transformed layer arises due to recoil implantation and cascade mixing or diffusion [see also Fig. 20(a)].<sup>393–395</sup> In semiconductor technology, the strong selectivity of the chemical erosion process is actively used for etching and structuring of surface patterns.<sup>396,397</sup> When using chemically reactive iodine as the propellant, chemical effects are clearly anticipated and material issues due to the reactivity of iodine need to be addressed. An example was already given in Fig. 9(d), where titanium-iodine species are formed during operation of a RIT with titanium grids. When operating thrusters on satellites with iodine over a longer period of time, the corrosiveness of the propellant cannot be ignored. An atmosphere of iodine will build up around the satellite and will be in contact with the materials used, giving rise to chemical reactions. Such material issues need to be clarified and will lead to adaption of the thruster design. Besides chemical sputtering, also chemical reactions with iodine deposited onto various parts of the satellite may

occur. The chemical reaction issue is clearly illustrated by the photographs in Fig. 23. They show material samples that were in contact with iodine during a period of time of several months at room temperature or several days at about  $80^\circ$ . The material samples are plate material ( $10 \times 10 \times 1 \text{ mm}^3$ ) with two holes of different sizes (0.5 mm and 2 mm in diameter). As expected, the corrosion behavior differs from sample to sample. Such tests or more complicated variants need to be performed with all kinds of space materials to establish their compatibility with iodine.

## V. OUTLOOK

The increased use of EP systems in space goes hand in hand with the desire of having cost-effective satellite systems available. Like any other technology entering or even driving a commercial market, EP will have to undergo ever faster development and production cycles in the coming years, and reliable standards for comparing different EP systems need to be established. Corresponding routine procedures for the testing of EP systems need to be developed. Modeling has the potential to accelerate development processes and establish comparability between test systems. New EP concepts will compete with established EP systems. Examples of current challenges arising in the field of EP are aspects of EMC and radiation hardness, which must be considered during all development stages. Furthermore, material aspects come to the fore, e. g., due to the use of chemically reactive propellants or in neutralizer development. Already these few examples demonstrate that it is necessary to establish broad interdisciplinary research networks. Only such



networks will be able to successfully address the various research challenges popping up when fully exploiting the potential of EP in space mission scenarios and, thus, are essential for guaranteeing the success of EP as enabling technology now and in the future.

## ACKNOWLEDGMENTS

This work was supported by the Federal Ministry for Economic Affairs and Energy under Contract Nos. 50RS1502, 50RS1709, 50RK1948, 50RS1707, and 50RM1530 and in the framework of the MINOTOR project, the NEMESIS project, and the iFACT project that have received funding from the European Union's Horizon 2020 research and innovation programme under Grant Agreements Nos. 730028, 870506, and 870336. Furthermore, EU regional funding via the EFRE scheme of the State of Hesse is gratefully acknowledged. The authors are also grateful for seed funding by the Research Campus of Central Hessen (RCCH) and for co-funding in frame of the funding scheme "Forschung für die Praxis 2018" of the Hessian Ministry of Higher Education, Research and the Arts. The authors would also like to thank Elisa Monte for her active support in creating the figures.

## DATA AVAILABILITY

The data that support the findings of this study are available from the corresponding author upon reasonable request. References for all other datasets are given in the text.

## REFERENCES

- <sup>1</sup>D. Sagath, A. Papadimitriou, M. Adriaensen, and C. Giannopapa, "Space strategy and governance of ESA small member states," *Acta Astronaut.* **142**, 112–120 (2018).
- <sup>2</sup>J. Kauffmann, The ESA SME initiative, [http://wirtschaft.rvsnr.de/fileadmin/user\\_upload/VERANSTALTUNGEN/Business\\_with\\_ESA/Kauffmann\\_ESA\\_SME\\_Initiative.pdf](http://wirtschaft.rvsnr.de/fileadmin/user_upload/VERANSTALTUNGEN/Business_with_ESA/Kauffmann_ESA_SME_Initiative.pdf).
- <sup>3</sup>I. Tchalakov, "The new space entrepreneurship and its techno-economic networks," *Int. J. Actor-Network Theory Technol. Innovation* **7**(1), 43–63 (2015).
- <sup>4</sup>D. Bhattacharjee, W. Aqeel, I. N. Bozkurt, A. Aguirre, B. Chandrasekaran, P. B. Godfrey, G. Laughlin, B. Maggs, and A. Singla, "Gearing up for the 21st century space race," in *HotNets'18: Proceedings of the 17th ACM Workshop on Hot Topics in Networks* (ACM Press, 2018).
- <sup>5</sup>J.-P. Boeuf, "Tutorial: Physics and modeling of Hall thrusters," *J. Appl. Phys.* **121**(1), 011101 (2017).
- <sup>6</sup>D. M. Goebel and I. Katz, *Fundamentals of Electric Propulsion: Ion and Hall Thrusters* (John Wiley & Sons, 2008).
- <sup>7</sup>E. Y. Choueiri, "Fundamental difference between the two Hall thruster variants," *Phys. Plasmas* **8**(11), 5025–5033 (2001).
- <sup>8</sup>Y. Ding, H. Fan, D. Ma *et al.*, "Extending service life of hall thrusters: Recent progress and future challenges," *Rev. Mod. Plasma Phys.* **3**, 15 (2019).
- <sup>9</sup>K. E. Ciolkovskij, *Ausserhalb der Erde* (Heyne Verlag, 1977).
- <sup>10</sup>H. Oberth, *Die Rakete zu den Planetenräumen* (Oldenbourg Wissensch.Vlg, 2015), URL: [https://www.ebook.de/de/product/28888763/hermann\\_oberth\\_die\\_rakete\\_zu\\_den\\_planetenraeumen.html](https://www.ebook.de/de/product/28888763/hermann_oberth_die_rakete_zu_den_planetenraeumen.html).
- <sup>11</sup>J. D. Hunley, "The enigma of Robert H. Goddard," *Technol. Cult.* **36**(2), 327 (1995).
- <sup>12</sup>R. H. Goddard, "A method of reaching extreme altitudes," *Nature* **105**(2652), 809–811 (1920).
- <sup>13</sup>J. T. Andrews, *Red Cosmos: K. E. Tsiolkovskii, Grandfather of Soviet Rocketry*, Centennial of Flight Series (Texas A&M University Press, 2009).
- <sup>14</sup>L. Garrigues and P. Coche, "Electric propulsion: Comparisons between different concepts," *Plasma Phys. Controlled Fusion* **53**(12), 124011 (2011).
- <sup>15</sup>M. J. Neufeld, "Wernher von Braun, the SS, and concentration camp labor: Questions of moral, political, and criminal responsibility," *Ger. Stud. Rev.* **25**(1), 57 (2002).
- <sup>16</sup>K. Dannenberg and E. Stuhlinger, "Rocket center peenemünde: Personal memories," *Acta Astronaut.* **34**, 385–395 (1994).
- <sup>17</sup>R. G. Koman, "Man on the Moon: The U.S. space program as a cold war maneuver," *OAH Mag. Hist.* **8**(2), 42–50 (1994).
- <sup>18</sup>J. A. Van Allen and L. A. Frank, "Radiation around the earth to a radial distance of 107,400 km," *Nature* **183**, 430 (1959).
- <sup>19</sup>E. Y. Choueiri, "A critical history of electric propulsion: The first 50 years (1906–1956)," *J. Propul. Power* **20**(2), 193–203 (2004).
- <sup>20</sup>R. Moloney, A. Lucca Fabris, D. Staab, A. Frey, A. Garbayo, and L. Shadbolt, "Space travel, electric propulsion and science fiction," in 77th World Science Fiction Convention, Dublin, Ireland, 2019.
- <sup>21</sup>R. H. Goddard, "Method of and means for producing electrified jets of gas," U.S. patent 1,363,037 (21 December 1920).
- <sup>22</sup>L. R. Shepherd and A. V. Cleaver, "The atomic rocket. I," *J. Brit. Interplanet. Soc.* **7**, 9 (1948).
- <sup>23</sup>L. R. Shepherd and A. V. Cleaver, "The atomic rocket. II," *J. Brit. Interplanet. Soc.* **7**, 11 (1948).
- <sup>24</sup>L. R. Shepherd and A. V. Cleaver, "The atomic rocket. III," *J. Brit. Interplanet. Soc.* **8**, 1 (1949).
- <sup>25</sup>L. R. Shepherd and A. V. Cleaver, "The atomic rocket. IV," *J. Brit. Interplanet. Soc.* **8**, 3 (1949).
- <sup>26</sup>E. Stuhlinger, *Ion Propulsion for Space Flight*, McGraw-Hill Series in Missile and Space Technology (McGraw-Hill, 1964).
- <sup>27</sup>H. R. Kaufman, "An ion rocket with an electron-bombardment ion source," NASA Technical Note TN D-585, 1961, p. 1.
- <sup>28</sup>H. R. Kaufman, *Technology of Electron-Bombardment Ion Thrusters*, Advances in Electronics and Electron Physics Vol. 36 (Academic Press, 1975), pp. 265–373.
- <sup>29</sup>H. R. Kaufman, "Origin of the electron-bombardment ion thruster," *J. Spacecr. Rockets* **18**(4), 289–292 (1981).
- <sup>30</sup>H. Löb, "Ein elektrostatisches raketentriebwerk mit hochfrequenzionenquelle," *Acta Astronaut.* **1**, 49 (1962).
- <sup>31</sup>H. Löb and J. Freisinger, *Ionenraketen* (Vieweg, 1967).
- <sup>32</sup>A. I. Morozov, "The conceptual development of stationary plasma thrusters," *Plasma Phys. Rep.* **29**(3), 235–250 (2003).
- <sup>33</sup>A. W. Bett, F. Dimroth, G. Stollwerck, and O. V. Sulima, "III-V compounds for solar cell applications," *Appl. Phys. A* **69**(2), 119–129 (1999).
- <sup>34</sup>T. Takamoto, H. Washio, and H. Juso, "Application of InGaP/GaAs/InGaAs triple junction solar cells to space use and concentrator photovoltaic," in *2014 IEEE 40th Photovoltaic Specialist Conference (PVSC)* (IEEE, 2014).
- <sup>35</sup>*Chemical Rocket Propulsion*, edited by L. T. De Luca, T. Shimada, V. P. Sinditskii, and M. Calabro (Springer International Publishing, 2017).
- <sup>36</sup>R. G. Jahn, *Physics of Electric Propulsion* (Dover Publications Inc., 2006).
- <sup>37</sup>D. Schmitt and L. Laurent, "59th International Astronautical Congress—Glasgow 2008: Session D2.1.6—Launch vehicles in service or in development, Ariane 5—Program status," *Acta Astronaut.* **66**(5–6), 871–882 (2010).
- <sup>38</sup>D. R. Lev, I. G. Mikellides, D. Pedrini, D. M. Goebel, B. A. Jorns, and M. S. McDonald, "Recent progress in research and development of hollow cathodes for electric propulsion," *Rev. Mod. Plasma Phys.* **3**(1), 6 (2019).
- <sup>39</sup>J. Sovey, V. Rawlin, and M. Patterson, "A synopsis of ion propulsion development projects in the United States: SERT I to deep space 1," in 35th Joint Propulsion Conference and Exhibit, June 1999.
- <sup>40</sup>N. N. Antropov, G. A. Popov, and M. N. Kazeev, "Ablative pulsed plasma thruster R&D in Russia since the beginning of the 90s," in 33rd International Electric Propulsion Conference, Washington, DC, USA, 2013, IEPC-2013-68.
- <sup>41</sup>R. L. Burton, "Pulsed plasma thrusters," in *Encyclopedia of Aerospace Engineering*, edited by R. Blockley and W. Shyy (Wiley, 2010).
- <sup>42</sup>R. M. Meyers, S. R. Oleson, M. McGuire, J. Meckel, and J. R. Cassady, "Pulsed plasma thruster technology for small satellite missions," in 9th AIAA/Utah State University Conference on Small Satellites, 1995.

- <sup>43</sup>B. Hendrickx, "A history of soviet/Russian meteorological satellites," *Space Chron.*: JBIS 57, 56–102 (2004).
- <sup>44</sup>S. P. Hughes, R. H. Qureshi, S. D. Cooley, and J. J. Parker, "Verification and validation of the general mission analysis tool (GMAT)," in AIAA/AAS Astrodynamics Specialist Conference, August 2014.
- <sup>45</sup>R. R. Stephenson, "Electric propulsion development and application in the United States," in 24th International Electric Propulsion Conference, Moscow, Russia, 1995, IEPC-1995-01.
- <sup>46</sup>D. Lev, R. M. Myers, K. M. Lemmer, J. Kolbeck, H. Koizumi, and K. Polzin, "The technological and commercial expansion of electric propulsion," *Acta Astronaut.* 159, 213–227 (2019).
- <sup>47</sup>T. P. Garrison, M. Ince, J. Pizzicardi, and P. A. Swan, "Systems engineering trades for the IRIDIUM constellation," *J. Spacecr. Rockets* 34(5), 675–680 (1997).
- <sup>48</sup>R. Killinger, R. Kukies, M. Surauer, L. van Holtz, and A. Tomasetto, "Orbit raising with ion propulsion on ESA's ARTEMIS satellite," in 38th AIAA/ASME/SAE/ASEE Joint Propulsion Conference and Exhibit, Indianapolis, IN, USA, 7–10 July 2002.
- <sup>49</sup>R. Killinger, R. Kukies, M. Surauer, A. Tomasetto, and L. van Holtz, "ARTEMIS orbit raising inflight experience with ion propulsion," *Acta Astronaut.* 53(4–10), 607–621 (2003).
- <sup>50</sup>European Space Agency, Telecom—Artes 4.0 programme—Electra, <https://artes.esa.int/electra>.
- <sup>51</sup>D. Lev, R. M. Myers, K. M. Lemmer, J. Kolbeck, M. Keidar, H. Koizumi, H. Liang, D. Yu, T. Schönherr, J. Gonzalez del Amo, W. Choe, R. Albertoni, A. Hoskins, S. Yan, W. Hart, R. R. Hofer, I. Funaki, A. Lovtsov, K. Polzin, A. Olshanskii, and O. Duchemin, "The technological and commercial expansion of electric propulsion in the past 24 years," in 35th International Electric Propulsion Conference, Atlanta, GA, USA, 2017, IEPC-2017-242.
- <sup>52</sup>G. D. Racca, A. Marini, L. Stagnaro, J. van Dooren, L. di Napoli, B. H. Foing, R. Lumb, J. Volp, J. Brinkmann, R. Grünagel, D. Estublier, E. Tremolizzo, M. McKay, O. Camino, J. Schoemaekers, M. Hechler, M. Khan, P. Rathsmann, G. Andersson, K. Anflo, S. Berge, P. Bodin, A. Edfors, A. Hussain, J. Kugelberg, N. Larsson, B. Ljung, L. Meijer, A. Mörtzell, T. Nordebäck, S. Persson, and F. Sjöberg, "SMART-1 mission description and development status," *Planet. Space Sci.* 50(14), 1323–1337 (2002).
- <sup>53</sup>J. Kugelberg, P. Bodin, S. Persson, and P. Rathsmann, "Accommodating electric propulsion on SMART-1," *Acta Astronaut.* 55(2), 121–130 (2004).
- <sup>54</sup>C. R. Koppel, F. Marchandise, M. Prioul, D. Estublier, and F. Darnon, "The SMART-1 electric propulsion subsystem around the moon: In flight experience," in 41st AIAA/ASME/ASEE Joint Propulsion Conference and Exhibit, Tucson, AZ, USA, 2005.
- <sup>55</sup>D. M. Di Cara and D. Estublier, "Smart-1: An analysis of flight data," *Acta Astronaut.* 57(2), 250–256 (2005).
- <sup>56</sup>J. A. Johannessen, G. Balmino, C. Le Provost, R. Rummel, R. Sabadini, H. Sunkel, C. C. Tscherning, P. Visser, P. Woodworth, C. Hughes, P. Legrand, N. Sneeuw, F. Perosanz, M. Aguirre-Martinez, H. Rebhan, and M. Drinkwater, "The European gravity field and steady-state ocean circulation explorer satellite mission: Its impact on geophysics," *Surv. Geophys.* 24(4), 339–386 (2003).
- <sup>57</sup>N. Wallace, P. Jameson, C. Saunders, M. Fehring, C. Edwards, and R. Floberghagen, "The GOCE ion propulsion assembly—Lessons learnt from the first 22 month of flight operations," in 32nd International Electric Propulsion Conference, Wiesbaden, Germany, 2011, IEPC-2011-327.
- <sup>58</sup>M. D. Rayman, P. Varghese, D. H. Lehman, and L. L. Livesay, "Results from the deep space 1 technology validation mission," *Acta Astronaut.* 47(2), 475–487 (2000).
- <sup>59</sup>M. D. Rayman, "The successful conclusion of the deep space 1 mission," *Space Technol.* 23(2–3), 185 (2003).
- <sup>60</sup>M. D. Rayman, T. C. Fraschetti, C. A. Raymond, and C. T. Russell, "Dawn: A mission in development for exploration of main belt asteroids vesta and ceres," *Acta Astronaut.* 58(11), 605–616 (2006).
- <sup>61</sup>C. Garner, M. Rayman, J. Brophy, and S. Mikes, "In-flight operation of the Dawn ion propulsion system through the preparations for escape from Vesta," in 48th AIAA/ASME/SAE/ASEE Joint Propulsion Conference and Exhibit, Atlanta, GA, USA, 2012.
- <sup>62</sup>H. Kuninaka, K. Nishiyama, Y. Shimizu, and K. Toki, "Flight status of cathodeless microwave discharge ion engines onboard HAYABUSA asteroid explorer," in 40th AIAA/ASME/SAE/ASEE Joint Propulsion Conference and Exhibit, Fort Lauderdale, FL, USA, 2004.
- <sup>63</sup>H. Kuninaka, K. Nishiyama, I. Funaki, T. Yamada, Y. Shimizu, and J. i. Kawaguchi, "Powered flight of electron cyclotron resonance ion engines on Hayabusa explorer," *J. Propul. Power* 23(3), 544–551 (2007).
- <sup>64</sup>H. Kuninaka, K. Nishiyama, Y. Shimizu, I. Funaki, H. Koizumi, S. Hosoda, and D. Nakata, "Hayabusa asteroid explorer powered by ion engines on the way to earth," in 31st International Electric Propulsion Conference (University of Michigan, Ann Arbor, MI, USA, 2009), IEPC-2009-267.
- <sup>65</sup>Y. Tsuda, M. Yoshikawa, M. Abe, H. Minamino, and S. Nakazawa, "System design of the Hayabusa 2—Asteroid sample return mission to 1999 JU3," *Acta Astronaut.* 91, 356–362 (2013).
- <sup>66</sup>J. Benkhoff, J. van Casteren, H. Hayakawa, M. Fujimoto, H. Laakso, M. Novara, P. Ferri, H. R. Middleton, and R. Ziethe, "BepiColombo—comprehensive exploration of Mercury: Mission overview and science goals," *Planet. Space Sci.* 58(1), 2–20 (2010).
- <sup>67</sup>O. Sutherland, D. Stramaccioni, J. Benkhoff, N. Wallace, D. Feili, A. Rocchi, and R. Jehn, "BepiColombo: ESA's interplanetary electric propulsion mission to mercury," in 36th International Electric Propulsion Conference, Vienna, Austria, 2019, IEPC-2019-824.
- <sup>68</sup>J. Snyder, D. M. Goebel, R. R. Hofer, J. E. Polk, N. C. Wallace, and H. Simpson, "Performance evaluation of the T6 ion engine," *J. Propul. Power* 28(2), 371–379 (2012).
- <sup>69</sup>P. Amaro-Seoane, H. Audley, S. Babak, J. Baker, E. Barausse, P. Bender, E. Berti, P. Binetruy, M. Born, D. Bortoluzzi, J. Camp, C. Caprini, V. Cardoso, M. Colpi, J. Conklin, N. Cornish, C. Cutler, K. Danzmann, R. Dolesi, L. Ferraioli, V. Ferroni, E. Fitzsimons, J. Gair, L. G. Bote, D. Giardini, F. Gibert, C. Grimaldi, H. Halloin, G. Heinzel, T. Hertog, M. Hewitson, K. Holley-Bockelmann, D. Hollington, M. Hueller, H. Inchauspe, P. Jetzer, N. Karnesis, C. Killow, A. Klein, B. Klipstein, N. Korsakova, S. L. Larson, J. Livas, I. Lloro, N. Man, D. Mance, J. Martino, I. Mateos, K. McKenzie, S. T. McWilliams, C. Miller, G. Mueller, G. Nardini, G. Nelemans, M. Nofrarias, A. Petiteau, P. Pivato, E. Plagnol, E. Porter, J. Reiche, D. Robertson, N. Robertson, E. Rossi, G. Russano, B. Schutz, A. Sesana, D. Shoemaker, J. Slutsky, C. F. Sopuerta, T. Sumner, N. Tamanini, I. Thorpe, M. Troebbs, M. Vallisneri, A. Vecchio, D. Vetrugno, S. Vitale, M. Volonteri, G. Wanner, H. Ward, P. Wass, W. Weber, and J. Ziem, "Laser interferometer space antenna," [arXiv:1702.00786](https://arxiv.org/abs/1702.00786) [astro-ph.IM] (2017).
- <sup>70</sup>P. Abbott *et al.* (LIGO Scientific Collaboration and Virgo Collaboration), "Observation of gravitational waves from a binary black hole merger," *Phys. Rev. Lett.* 116(6), 061102 (2016).
- <sup>71</sup>M. Armano *et al.*, "Sub-Femto-gFree fall for space-based gravitational wave observatories: LISA pathfinder results," *Phys. Rev. Lett.* 116(23), 231101 (2016).
- <sup>72</sup>S. Cesare and G. Sechi, "Next generation gravity mission," in *Distributed Space Missions for Earth System Monitoring*, Space Technology Library, edited by M. D'Errico (Springer, New York, NY, 2012).
- <sup>73</sup>M. Smirnova, A. Mingo, J. Schein, P. Smirnov, E. Bosch, and L. Massotti, "Test campaign on the novel variable isp radio frequency mini ion engine," in 36th International Electric Propulsion Conference, Vienna, Austria, 2019, IEPC-2019-A-574.
- <sup>74</sup>H. J. Leiter, D. Lauer, P. Bauer, M. Berger, and M. Rath, "The Ariane group electric propulsion program 2019–2020," in 36th International Electric Propulsion Conference, Vienna, Austria, 2019.
- <sup>75</sup>S. A. Feuerborn, D. A. Neary, and J. M. Perkins, "Finding a way: Boeing's all electric propulsion satellite," in 49th AIAA/ASME/SAE/ASEE Joint Propulsion Conference, San Jose, CA, USA, July 2013.
- <sup>76</sup>S. Mazouffre and L. Grimaud, "Characteristics and performances of a 100-W Hall thruster for microspacecraft," *IEEE Trans. Plasma Sci.* 46(2), 330–337 (2018).
- <sup>77</sup>D. M. Goebel, M. Martinez-Lavin, T. A. Bond, and A. M. King, "Performance of the XIPS electric propulsion in on-orbit station keeping of the Boeing 702 spacecraft," in 38th AIAA/ASME/SAE/ASEE Joint Propulsion Conference and Exhibit, Indianapolis, IN, USA, 7–10 July 2002.
- <sup>78</sup>D. Minoli, *Innovations in Satellite Communication and Satellite Technology*, 1st ed. (Wiley, 2015).

- <sup>79</sup>E. Rezugina, A. Demairé, A. Edfors, B. Andersson, P. Rathsmann, E. Lamoureux, F. Sjöberg, and M. De Tata, "All EP platform: Mission design challenges and subsystem design opportunities," in 33rd International Electric Propulsion Conference, Washington, DC, USA, 2013, IEPC-2013-93.
- <sup>80</sup>W. A. Hanson, "Satellite internet in the mobile age," *New Space* **4**(3), 138–152 (2016).
- <sup>81</sup>I. del Portillo, B. G. Cameron, and E. F. Crawley, "A technical comparison of three low earth orbit satellite constellation systems to provide global broadband," *Acta Astronaut.* **159**, 123–135 (2019).
- <sup>82</sup>F. Cichocki, M. Merino, E. Ahedo, M. Smirnova, A. Mingo, and M. Dobkevicius, "Electric propulsion subsystem optimization for ion beam shepherd missions," *J. Propul. Power* **33**(2), 370–378 (2017).
- <sup>83</sup>B. Bastida Virgili, J. C. Dolado, H. G. Lewis, J. Radtke, H. Krag, B. Revelin, C. Cazaux, C. Colombo, R. Crowther, and M. Metz, "Risk to space sustainability from large constellations of satellites," *Acta Astronaut.* **126**, 154–162 (2016).
- <sup>84</sup>S. Le May, S. Gehly, B. A. Carter, and S. Flegel, "Space debris collision probability analysis for proposed global broadband constellations," *Acta Astronaut.* **151**, 445–455 (2018).
- <sup>85</sup>D. L. Oltrogge, S. Alfano, C. Law, A. Cacioni, and T. S. Kelso, "A comprehensive assessment of collision likelihood in Geosynchronous Earth Orbit," *Acta Astronaut.* **147**, 316 (2018).
- <sup>86</sup>D. J. Kessler and B. G. Cour-Palais, "Collision frequency of artificial satellites: The creation of a debris belt," *J. Geophys. Res.* **83**(A6), 2637, <https://doi.org/10.1029/ja083ia06p02637> (1978).
- <sup>87</sup>D. J. Kessler, "Collisional cascading: The limits of population growth in low earth orbit," *Adv. Space Res.* **11**(12), 63–66 (1991).
- <sup>88</sup>J.-C. Liou and N. L. Johnson, "A sensitivity study of the effectiveness of active debris removal in LEO," *Acta Astronaut.* **64**(2–3), 236–243 (2009).
- <sup>89</sup>C. Bombardelli and J. Peláez, "Ion beam shepherd for contactless space debris removal," *J. Guid., Control, Dyn.* **34**(3), 916–920 (2011).
- <sup>90</sup>A. Alpatov, F. Cichocki, A. Fokov, S. Khoroshylov, M. Merino, and A. Zakrzhevskii, "Determination of the force transmitted by an ion thruster plasma plume to an orbital object," *Acta Astronaut.* **119**, 241–251 (2016).
- <sup>91</sup>A. Alpatov, S. Khoroshylov, and C. Bombardelli, "Relative control of an ion beam shepherd satellite using the impulse compensation thruster," *Acta Astronaut.* **151**, 543–554 (2018).
- <sup>92</sup>F. Cichocki, M. Merino, and E. Ahedo, "Spacecraft-plasma-debris interaction in an ion beam shepherd mission," *Acta Astronaut.* **146**, 216–227 (2018).
- <sup>93</sup>M. Merino, E. Ahedo, C. Bombardelli, H. Urrutxua, and J. Peláez, "Ion beam shepherd satellite for space debris removal," in *Progress in Propulsion Physics* (EDP Sciences, 2013).
- <sup>94</sup>C. Bombardelli, H. Urrutxua, M. Merino, J. Peláez, and E. Ahedo, "The ion beam shepherd: A new concept for asteroid deflection," *Acta Astronaut.* **90**(1), 98–102 (2013).
- <sup>95</sup>I. Adamovich, S. D. Baalrud, A. Bogaerts, P. J. Bruggeman, M. Cappelli, V. Colombo, U. Czarnetzki, U. Ebert, J. G. Eden, P. Favia, D. B. Graves, S. Hamaguchi, G. Hieftje, M. Hori, I. D. Kaganovich, U. Kortshagen, M. J. Kushner, N. J. Mason, S. Mazouffre, S. M. Thagard, H.-R. Metelmann, A. Mizuno, E. Moreau, A. B. Murphy, B. A. Niemira, G. S. Oehrlein, Z. L. Petrovic, L. C. Pitchford, Y.-K. Pu, S. Rauf, O. Sakai, S. Samukawa, S. Starikovskaia, J. Tennyson, K. Terashima, M. M. Turner, M. C. M. van de Sanden, and A. Vardelle, "The 2017 Plasma Roadmap: Low temperature plasma science and technology," *J. Phys. D: Appl. Phys.* **50**(32), 323001 (2017).
- <sup>96</sup>H. Elsner, "Noble gases: Supply really critical?," German Mineral Resources Agency (DERA) at the Federal Institute for Geosciences and Natural Resources (BGR), 2018.
- <sup>97</sup>M. Martinez-Sanchez and J. E. Pollard, "Spacecraft electric propulsion—an overview," *J. Propul. Power* **14**(5), 688–699 (1998).
- <sup>98</sup>M. Gollor, E. Bourguignon, G. Glorieux, N. Wagner, J. Palencia, P. Galantini, W. Dechent, A. Franke, U. Schwab, and G. Tuccio, "Electric propulsion electronics activities in Europe 2016," in 52nd AIAA/SAE/ASEE Joint Propulsion Conference, Salt Lake City, UT, USA, 2016.
- <sup>99</sup>S. Mazouffre, "Electric propulsion for satellites and spacecraft: Established technologies and novel approaches," *Plasma Sources Sci. Technol.* **25**(3), 033002 (2016).
- <sup>100</sup>D. R. Lev, G. D. Emsellem, and A. K. Hallock, "The rise of the electric age for satellite propulsion," *New Space* **5**(1), 4–14 (2017).
- <sup>101</sup>I. Levchenko, S. Xu, S. Mazouffre, D. Lev, D. Pedrini, D. Goebel, L. Garrigues, F. Taccogna, and K. Bazaka, "Perspectives, frontiers, and new horizons for plasma-based space electric propulsion," *Phys. Plasmas* **27**(2), 020601 (2020).
- <sup>102</sup>K. Matyash, R. Schneider, A. Mutzke, O. Kalentev, F. Taccogna, N. Koch, and M. Schirra, "Comparison of SPT and HEMP thruster concepts from kinetic simulations," in 31st International Electric Propulsion Conference, Michigan, USA, 2009, IEPC-2009-159.
- <sup>103</sup>G. Kornfeld, N. Koch, and G. Coustou, "The highly efficient multistage plasma (HEMP) thruster, a new electric propulsion concept derived from tube technology," in 4th IEEE International Vacuum Electronics Conference (IEEE, 2003).
- <sup>104</sup>K. Takahashi, "Helicon-type radiofrequency plasma thrusters and magnetic plasma nozzles," *Rev. Mod. Plasma Phys.* **3**(3) (2019).
- <sup>105</sup>A. Hoskins, "Resistojets and arcjets," in *Encyclopedia of Aerospace Engineering*, edited by R. Blockley and W. Shyy (Wiley, 2010).
- <sup>106</sup>B. Wollenhaupt, Q. H. Le, and G. Herdrich, "Overview of thermal arcjet thruster development," *Aircr. Eng. Aerosp. Technol.* **90**(2), 280–301 (2018).
- <sup>107</sup>N. Koch, H.-P. Harmann, and G. Kornfeld, "First test results of the 1 to 15 kW coaxial HEMP 30250 thruster," in 41st AIAA/ASME/SAE/ASEE Joint Propulsion Conference and Exhibit, Tucson, AZ, USA, July 2005.
- <sup>108</sup>G. Kornfeld, N. Koch, H.-P. Harmann, P. Micheli, H. Meusemann, and E. Gengembre, "High power HEMP-thruster module, status and results of a DLR and ESA development program," in 42nd AIAA/ASME/SAE/ASEE Joint Propulsion Conference and Exhibit, Sacramento, CA, USA, July 2006.
- <sup>109</sup>M. Andrenucci, "Magnetoplasmadynamic thrusters," in *Encyclopedia of Aerospace Engineering*, edited by R. Blockley and W. Shyy (Wiley, 2010).
- <sup>110</sup>K. D. Diamant, J. E. Pollard, R. B. Cohen, Y. Raitses, and N. J. Fisch, "Segmented electrode Hall thruster," *J. Propul. Power* **22**(6), 1396–1401 (2006).
- <sup>111</sup>K. Kuriki and M. Inutake, "Super-Alfvénic flow and collision free shock wave in a plasma wind tunnel," *Phys. Fluids* **17**(1), 92–99 (1974).
- <sup>112</sup>M. Zuin, R. Cavazzana, E. Martines, G. Serianni, V. Antoni, M. Bagatin, M. Andrenucci, F. Paganucci, and P. Rossetti, "Kink instability in applied-field magneto-plasma-dynamic thrusters," *Phys. Rev. Lett.* **92**, 225003 (2004).
- <sup>113</sup>M. Peukert and B. Wollenhaupt, "OHV-System's view on electric propulsion needs," in Presentation, EPIC Workshop, Brussels, Belgium, 2014.
- <sup>114</sup>B. Wollenhaupt, M. Peukert, and R. Gabrielli, "Comparison of mission needs with available electric propulsion technologies," in Space Propulsion Conference, Rome, Italy, 2016.
- <sup>115</sup>G. P. Sutton and O. Biblarz, *Rocket Propulsion Elements* (John Wiley & Sons, 2017).
- <sup>116</sup>V. Murashko, A. Koryakin, A. Nyatin, V. Kim, G. Popov, A. Romashko, Y. Yermoshkin, V. Petrushevich, O. Goshkov, A. Koretyev, V. Garkusha, A. Semkin, and S. Tverdokhlebov, "State of the art prospects of electric propulsion in Russia," in 28th International Electric Propulsion Conference, Toulouse, France, 2003, IEPC-2003-340.
- <sup>117</sup>A. S. Koroteev, A. S. Lovtsov, V. A. Muravlev, M. Y. Selivanov, and A. A. Shagayda, "Development of ion thruster IT-500," *Eur. Phys. J. D* **71**, 120 (2017).
- <sup>118</sup>A. Rezaeiha and T. Schönherr, "Analysis of effective parameters on ablative PPT performance," *Aircr. Eng. Aerosp. Technol.* **84**(4), 231 (2012).
- <sup>119</sup>B. J. Sausser, R. R. Reilly, and A. J. Shenhar, "Why projects fail? How contingency theory can provide new insights—A comparative analysis of NASA's mars climate orbiter loss," *Int. J. Proj. Manage.* **27**(7), 665–679 (2009).
- <sup>120</sup>S. W. Greenwood, "Definition of specific impulse," *J. Spacecr. Rockets* **12**(1), 62 (1975).
- <sup>121</sup>A. Africano, "Comment on 'Definition of specific impulse'," *J. Spacecr. Rockets* **12**(9), 0576a (1975).
- <sup>122</sup>R. Walker, C. Bramanti, O. Sutherland, R. Boswell, C. Charles, D. Fearn, J. Del Amo, P. Frigor, and M. Orlandi, "Initial experiments on a dual-stage 4-grid ion thruster for very high specific impulse and power," in 42nd AIAA/ASME/SAE/ASEE Joint Propulsion Conference and Exhibit, Sacramento, CA, USA, July 2006.
- <sup>123</sup>C. Bramanti, D. Izzo, T. Samaraee, R. Walker, and D. Fearn, "Very high delta-V missions to the edge of the solar system and beyond enabled by the dual-stage 4-grid ion thruster concept," *Acta Astronaut.* **64**(7–8), 735–744 (2009).



- <sup>124</sup>J. Freisinger, K. Groh, J. Krempel-Hesse, J. M. Krumeich, H. W. Löb, A. Scharmann, and H. W. Velten, "Non-propulsive application of the RF-ion thruster for material processing with reactive gases," in *Proceedings of the 20th Electric Propulsion Conference (AIAA/DGLR/JSASS, Germany, 1988)*, p. 665.
- <sup>125</sup>V. Godyak, "Ferromagnetic enhanced inductive plasma sources," *J. Phys. D* **46**(28), 283001 (2013).
- <sup>126</sup>M. Becker, M. Gies, A. Polity, S. Chatterjee, and P. J. Klar, "Materials processing using radio-frequency ion-sources: Ion-beam sputter-deposition and surface treatment," *Rev. Sci. Instrum.* **90**(2), 023901 (2019).
- <sup>127</sup>H. W. Löb, K. H. Schartner, S. Weis, D. Feili, and B. K. Meyer, "Development of RIT-microthrusters," in 55th IAF-Congress, Vancouver, 2004, IAC-04S.4.04.
- <sup>128</sup>I. A. Kotelnikov and V. T. Astrelin, "Theory of a plasma emitter of positive ions," *Phys.-Usp.* **58**(7), 701–718 (2015).
- <sup>129</sup>M. Sangregorio, K. Xie, N. Wang, N. Guo, and Z. Zhang, "Ion engine grids: Function, main parameters, issues, configurations, geometries, materials and fabrication methods," *Chin. J. Aeronaut.* **31**(8), 1635–1649 (2018).
- <sup>130</sup>V. Kim, "Main physical features and processes determining the performance of stationary plasma thrusters," *J. Propul. Power* **14**(5), 736–743 (1998).
- <sup>131</sup>R. Killinger, H. Bassner, J. Müller, and R. Kukies, "RITA ion propulsion for ARTEMIS lifetime test results," in 36th AIAA/ASME/SAE/ASEE Joint Propulsion Conference and Exhibit, Huntsville, AL, USA, 2000.
- <sup>132</sup>R. Killinger, H. Bassner, R. Kukies, and H. Leiter, "Results of the 15000 hours lifetime test for the RITA ion propulsion on ESA's ARTEMIS satellite," in 27th International Electric Propulsion Conference, Pasadena, CA, USA, 2001, IEPC-2001-082.
- <sup>133</sup>G. Aston, H. R. Kaufman, and P. J. Wilbur, "Ion beam divergence characteristics of two-grid accelerator systems," *AIAA J.* **16**(5), 516–524 (1978).
- <sup>134</sup>G. Aston and H. R. Kaufman, "Ion beam divergence characteristics of three-grid accelerator systems," *AIAA J.* **17**(1), 64–70 (1979).
- <sup>135</sup>P. Spädtke and D. Ivens, "The use of micro-computers in the simulation of ion beam optics," *Vacuum* **39**(11–12), 1043–1046 (1989).
- <sup>136</sup>J. C. Whitson, J. Smith, and J. H. Whealton, "Calculations involving ion beam source," *J. Comput. Phys.* **28**(3), 408–415 (1978).
- <sup>137</sup>P. Spädtke, "Modeling ion beam extraction from different types of ion sources," *Rev. Sci. Instrum.* **89**(8), 081101 (2018).
- <sup>138</sup>R. Becker and W. B. Herrmannsfeldt, "IGUN: A program for the simulation of positive ion extraction including magnetic fields," *Rev. Sci. Instrum.* **63**(4), 2756–2758 (1992).
- <sup>139</sup>P. Spädtke, KOBRA3-INP User Manual, 2013.
- <sup>140</sup>T. Kalvas, O. Tarvainen, T. Ropponen, O. Steczkiewicz, J. Ärje, and H. Clark, "IBSIMU: A three-dimensional simulation software for charged particle optics," *Rev. Sci. Instrum.* **81**(2), 02B703 (2010).
- <sup>141</sup>K. Hanke, S. Heising, G. Probert, and R. Scrivens, "Comparison of simulation codes for the beam dynamics of low-energy ions," *Rev. Sci. Instrum.* **73**(2), 783–785 (2002).
- <sup>142</sup>M. Tartz, E. Hartmann, and H. Neumann, "Validated simulation of the ion extraction grid lifetime," *Rev. Sci. Instrum.* **79**(2), 02B905 (2008).
- <sup>143</sup>Z. Lingwei, L. Yu, L. Juan, G. Zuo, J. Haocheng, W. Haixing, and T. Haibin, "Numerical simulation of characteristics of CEX ions in ion thruster optical system," *Chin. J. Aeronaut.* **23**(1), 15–21 (2010).
- <sup>144</sup>T. Miyasaka, T. Kobayashi, and K. Asato, "Characteristics of ions impacting grid surfaces in an ion engine," *Vacuum* **85**(5), 585–590 (2010).
- <sup>145</sup>M. Nakano, "Sensitivity analysis of the effects of doubly charged ions on ion acceleration grid erosion," *Trans. Jpn. Soc. Aeronaut. Space Sci.* **55**(6), 364–372 (2012).
- <sup>146</sup>A. Shagayda, V. Nikitin, and D. Tomilin, "Three-dimensional analysis of ion optics with misalignments of apertures," *Vacuum* **123**, 140–150 (2016).
- <sup>147</sup>I. Katz, I. G. Mikellides, R. Wirz, J. R. Anderson, and D. M. Goebel, "Ion thruster life models," in 41st AIAA/ASME/SAE/ASEE Joint Propulsion Conference and Exhibit, Tucson, AZ, 2005.
- <sup>148</sup>H. Watanabe, M. Nakano, Y. Kajimura, I. Funaki, and R. Takaki, "Numerical life qualification of ion thruster's ion optics using the JIEDI tool," in 49th AIAA/ASME/SAE/ASEE Joint Propulsion Conference, San Jose, CA, USA, July 2013.
- <sup>149</sup>J. Wang, J. Polk, J. Brophy, and I. Katz, "Three-dimensional particle simulations of ion-optics plasma flow and grid erosion," *J. Propul. Power* **19**(6), 1192–1199 (2003).
- <sup>150</sup>S. J. Plimpton, S. G. Moore, A. Borner, A. K. Staggs, T. P. Koehler, J. R. Torczynski, and M. A. Gallis, "Direct simulation Monte Carlo on petaflop supercomputers and beyond," *Phys. Fluids* **31**(8), 086101 (2019).
- <sup>151</sup>T. J. Scanlon, E. Roohi, C. White, M. Darbandi, and J. M. Reese, "An open source, parallel DSMC code for rarefied gas flows in arbitrary geometries," *Comput. Fluids* **39**(10), 2078–2089 (2010).
- <sup>152</sup>C. White, M. K. Borg, T. J. Scanlon, S. M. Longshaw, B. John, D. R. Emerson, and J. M. Reese, "dsmcFoam+An OpenFOAM based direct simulation Monte Carlo solver," *Comput. Phys. Commun.* **224**, 22–43 (2018).
- <sup>153</sup>X. He and L.-S. Luo, "Theory of the lattice Boltzmann method: From the Boltzmann equation to the lattice Boltzmann equation," *Phys. Rev. E* **56**(6), 6811–6817 (1997).
- <sup>154</sup>P. Clausing, "The flow of highly rarefied gases through tubes of arbitrary length," *J. Vac. Sci. Technol.* **8**(5), 636–646 (1971).
- <sup>155</sup>D. M. Goebel, "Ion source discharge performance and stability," *Phys. Fluids* **25**(6), 1093–1102 (1982).
- <sup>156</sup>D. M. Goebel, R. E. Wirz, and I. Katz, "Analytical ion thruster discharge performance model," *J. Propul. Power* **23**(5), 1055–1067 (2007).
- <sup>157</sup>D. M. Goebel, "Analytical discharge model for RF ion thrusters," *IEEE Trans. Plasma Sci.* **36**(5), 2111–2121 (2008).
- <sup>158</sup>P. Chabert, J. A. Monreal, J. Bredin, L. Popelier, and A. Aanesland, "Global model of a gridded-ion thruster powered by a radiofrequency inductive coil," *Phys. Plasmas* **19**(7), 073512 (2012).
- <sup>159</sup>M. Dobkevicius and D. Feili, "Multiphysics model for radio-frequency gridded ion thruster performance," *J. Propul. Power* **33**(4), 939–953 (2017).
- <sup>160</sup>C. Volkmar and U. Ricklefs, "Implementation and verification of a hybrid performance and impedance model of gridded radio-frequency ion thrusters," *Eur. Phys. J. D* **69**(10), 227 (2015).
- <sup>161</sup>A. Reeh, U. Probst, and P. J. Klar, "Global model of a radio-frequency ion thruster based on a holistic treatment of electron and ion density profiles," *Eur. Phys. J. D* **73**, 232 (2019).
- <sup>162</sup>Q. T. D. Pham and J. Shin, "Better prediction of the performance of a radio-frequency ion thruster," *J. Korean Phys. Soc.* **76**(2), 137–144 (2020).
- <sup>163</sup>R. Henrich and C. Heiliger, "Investigation of the plasma in a RIT using PIC modelling," in 35th International Electric Propulsion Conference, Atlanta, GA, USA, 2017, IEPC-2017-518.
- <sup>164</sup>D. M. Goebel, R. M. Watkins, and K. K. Jameson, "LaB<sub>6</sub> hollow cathodes for ion and Hall thrusters," *J. Propul. Power* **23**(3), 552–558 (2007).
- <sup>165</sup>Y.-K. Kim and M. E. Rudd, "Binary-encounter-dipole model for electron-impact ionization," *Phys. Rev. A* **50**(5), 3954–3967 (1994).
- <sup>166</sup>R. F. Boivin and S. K. Srivastava, "Electron-impact ionization of Mg," *J. Phys. B: At., Mol. Opt. Phys.* **31**, 2381–2394 (1998).
- <sup>167</sup>Y. Itikawa and N. Mason, "Cross sections for electron collisions with water molecules," *J. Phys. Chem. Ref. Data* **34**, 1–22 (2005).
- <sup>168</sup>R. Rejoub, B. G. Lindsay, and R. F. Stebbings, "Determination of the absolute partial and total cross sections for electron-impact ionization of the rare gases," *Phys. Rev. A* **65**(4), 042713 (2002).
- <sup>169</sup>H. C. Straub, P. Renault, B. G. Lindsay, K. A. Smith, and R. F. Stebbings, "Absolute partial cross sections for electron-impact ionization of H<sub>2</sub>, N<sub>2</sub>, and O<sub>2</sub> from threshold to 1000 eV," *Phys. Rev. A* **54**(3), 2146–2153 (1996).
- <sup>170</sup>National Institute of Standards and Technology, "Electron-Impact cross sections for ionization and excitation," <https://physics.nist.gov/PhysRefData/Ionization/molTable.html>.
- <sup>171</sup>K. Holste, W. Gärtner, D. Zschätzsch, S. Scharmann, P. Köhler, P. Dietz, and P. J. Klar, "Performance of an iodine-fueled radio-frequency ion-thruster," *Eur. Phys. J. D* **72**(1), 9 (2018).
- <sup>172</sup>N. Fazio, S. B. Gabriel, and I. O. Golosnoy, *Alternative Propellants for Gridded Ion Engines* (Space Propulsion Conference, Sevilla, Spain, 2018).
- <sup>173</sup>P. Tisdall, E. Dyer, C. Ryan, V. Garcia, and A. Demairé, "Initial investigation of alternative propellants for use with a low-power cylindrical Hall thruster," in Space Propulsion 2018 Conference, Sevilla, Spain, 2018.



- <sup>174</sup>P. Dietz, W. Gärtner, Q. Koch, P. E. Köhler, Y. Teng, P. R. Schreiner, K. Holste, and P. J. Klar, "Molecular propellants for ion thrusters," *Plasma Sources Sci. Technol.* **28**(8), 084001 (2019).
- <sup>175</sup>N. Fazio, S. B. Gabriel, I. O. Golosnoy, and B. Wollenhaupt, "Mission cost for gridded ion engines using alternative propellants," in 36th International Electric Propulsion Conference, Vienna, Austria, 2019.
- <sup>176</sup>B. A. Arkhipov, A. I. Koryakin, V. M. Murashko, A. N. Nesterenko, I. A. Khoromsky, V. Kim, V. I. Kozlov, G. A. Popov, and A. I. Skrylnikov, "The results of testing and effectiveness of the Kr-Xe mixture application in SPT," in 27th International Electric Propulsion Conference, Pasadena, CA, USA, 2001, IEPC-2001-064.
- <sup>177</sup>J. Anderson and D. Fitzgerald, "Fullerene propellant research for electric propulsion," in 32nd Joint Propulsion Conference and Exhibit, 1996.
- <sup>178</sup>C. A. Scharlemann, "Theoretical and experimental investigation of C<sub>60</sub>-propellant for ion propulsion," *Acta Astronaut.* **51**(12), 865–872 (2002).
- <sup>179</sup>A. Kieckhafer and L. B. King, "Energetics of propellant options for high-power Hall thrusters," *J. Propul. Power* **23**(1), 21–26 (2007).
- <sup>180</sup>R. Dressler, Y.-H. Chiu, and D. Levandier, "Propellant alternatives for ion and Hall thrusters," in Proceedings of the 28th Aerospace Science Meeting and Exhibit, Reno, NV, USA, 2000.
- <sup>181</sup>O. S. Tverdokhlebov and A. V. Semnenkin, "Iodine propellant for electric propulsion: To be or not to be," in Proceedings of the 37th AIAA/ASME/SAE/ASEE Joint Propulsion Conference, Salt Lake City, UT, USA, 2001.
- <sup>182</sup>M. Tsay, J. Frongillo, and K. Hohmann, "Iodine-fueled mini RF ion thruster for CubeSat applications," in 34th International Electric Propulsion Conference, Hyogo-Kobe, Japan, 2015, IEPC-2015-273.
- <sup>183</sup>M. Tsay, J. Frongillo, J. Model, J. Zwahlen, and L. Paritsky, "Maturisation of iodine-fueled BIT-3 RF ion thruster and RF neutralizer," in 52nd AIAA/SAE/ASEE Joint Propulsion Conference, Salt Lake City, USA, 2016.
- <sup>184</sup>P. Grondein, T. Lafleur, P. Chabert, and A. Aanesland, "Global model of an iodine gridded plasma thruster," *Phys. Plasmas* **23**(3), 033514 (2016).
- <sup>185</sup>H. Schwertfeger, A. A. Fokin, and P. R. Schreiner, "Diamonds are a chemist's best friend: Diamondoid chemistry beyond adamantane," *Angew. Chem.* **47**(6), 1022–1036 (2008).
- <sup>186</sup>K. Lenzke, L. Landt, M. Hoener, H. Thomas, J. E. Dahl, S. G. Liu, R. M. K. Carlson, T. Möller, and C. Bostedt, "Experimental determination of the ionization potentials of the first five members of the nanodiamond series," *J. Chem. Phys.* **127**(8), 084320 (2007).
- <sup>187</sup>M. A. Gunawan, J.-C. Hierso, D. Poinso, A. A. Fokin, N. A. Fokina, B. A. Tkachenko, and P. R. Schreiner, "Diamondoids: Functionalization and subsequent applications of perfectly defined molecular cage hydrocarbons," *New J. Chem.* **38**(1), 28–41 (2014).
- <sup>188</sup>H. C. Straub, P. Renault, B. G. Lindsay, K. A. Smith, and R. F. Stebbings, "Absolute partial and total cross sections for electron-impact ionization of argon from threshold to 1000 eV," *Phys. Rev. A* **52**(2), 1115–1124 (1995).
- <sup>189</sup>H. C. Straub, B. G. Lindsay, K. A. Smith, and R. F. Stebbings, "Absolute partial cross sections for electron-impact ionization of CO<sub>2</sub> from threshold to 1000 eV," *J. Chem. Phys.* **105**(10), 4015–4022 (1996).
- <sup>190</sup>H. C. Straub, B. G. Lindsay, K. A. Smith, and R. F. Stebbings, "Absolute partial cross sections for electron-impact ionization of H<sub>2</sub>O and D<sub>2</sub>O from threshold to 1000 eV," *J. Chem. Phys.* **108**(1), 109–116 (1998).
- <sup>191</sup>S. Maclot, J. Lahl, J. Peschel *et al.*, "Dissociation dynamics of the diamondoid adamantane upon photoionization by XUV femtosecond pulses," *Sci. Rep.* **10**, 2884 (2020).
- <sup>192</sup>S. W. Jackson and R. Marshall, "Conceptual design of an air-breathing electric thruster for CubeSat applications," *J. Spacecr. Rockets* **55**(3), 632–639 (2018).
- <sup>193</sup>W. J. Larson and J. R. Wertz, *Space Mission Analysis and Design*, 3rd ed., Space Technology Library (Microcosm and Wiley Larson, 2005).
- <sup>194</sup>T. Schonherr, K. Komurasaki, F. Romano, B. Massuti-Ballester, and G. Herdrich, "Analysis of atmosphere-breathing electric propulsion," *IEEE Trans. Plasma Sci.* **43**(1), 287–294 (2015).
- <sup>195</sup>K. Nishiyama, "Air breathing ion engine concept," in 54th International Astronautical Congress of the International Astronautical Federation, the International Academy of Astronautics, and the International Institute of Space Law (American Institute of Aeronautics and Astronautics, 2003).
- <sup>196</sup>D. Di Cara, J. Gonzalez del Amo, A. Santovincenzo, B. C. Dominguez, M. Arcioni, A. Caldwell, and I. Roma, "RAM electric propulsion for low earth orbit operation: An ESA study," in 30th International Electric Propulsion Conference, Florence, Italy, 2007, IEPC-2007-162.
- <sup>197</sup>K. Diamant, "A 2-stage cylindrical Hall thruster for air breathing electric propulsion," in 46th AIAA/ASME/SAE/ASEE Joint Propulsion Conference and Exhibit, July 2010.
- <sup>198</sup>T. Andreussi, G. Cifali, V. Giannetti, A. Piragino, E. Ferrato, A. Rossodivita, M. Andrenucci, J. Longo, and L. Walpot, "Development and experimental validation of a Hall effect thruster RAM-EP concept," in 35th International Electric Propulsion Conference, Atlanta, GA, USA, 2017, IEPC-2017-377.
- <sup>199</sup>K. Katsonis, C. Berenguer, J. Gonzalez del Amo, and J. Stavrinidis, "CO<sub>2</sub>/N<sub>2</sub> breathing electric thrusters for low Mars orbit," in Space Propulsion 2016 Conference, Rome, Italy, 2016.
- <sup>200</sup>E. M. Petro and R. J. Sedwick, "Survey of moderate-power electric propulsion systems," *J. Spacecr. Rockets* **54**(3), 529–541 (2017).
- <sup>201</sup>K. Nakamura, Y. Nakagawa, H. Koizumi, and Y. Takao, "Numerical analysis of a miniature microwave-discharge ion thruster using water as the propellant," *Trans. Jpn. Soc. Aeronaut. Space Sci.* **61**(4), 152–159 (2018).
- <sup>202</sup>Y. Nakagawa, D. Tomita, H. Koizumi, and K. Komurasaki, "Design and test of a 100 μN-class thrust stand for a miniature water ion thruster with CubeSat," *Trans. Jpn. Soc. Aeronaut. Space Sci.* **16**(7), 673–678 (2018).
- <sup>203</sup>Y. Nakagawa, H. Koizumi, H. Kawahara, and K. Komurasaki, "Performance characterization of a miniature microwave discharge ion thruster operated with water," *Acta Astronaut.* **157**, 294–299 (2019).
- <sup>204</sup>K. Nakamura, H. Koizumi, M. Nakano, and Y. Takao, "Effects of negative ions on discharge characteristics of water plasma source for a miniature microwave discharge ion thruster," *Phys. Plasmas* **26**(4), 043508 (2019).
- <sup>205</sup>J. Szabo, M. Robin, J. Duggan, and R. R. Hofer, "Light metal propellant Hall thrusters," in 31st International Electric Propulsion Conference (University of Michigan, Ann Arbor, MI, USA, 2009), IEPC-2009-138.
- <sup>206</sup>J. S. Sovey, V. K. Rawlin, and M. J. Patterson, "Ion propulsion development projects in U.S.: Space electric rocket test I to deep space 1," *J. Propul. Power* **17**(3), 517–526 (2001).
- <sup>207</sup>D. Fourie, I. M. Hedgecock, F. De Simone, E. M. Sunderland, and N. Pirrone, "Are mercury emissions from satellite electric propulsion an environmental concern?," *Environ. Res. Lett.* **14**(12), 124021 (2019).
- <sup>208</sup>P. Dietz, F. Becker, K. Keil, K. Holste, and P. J. Klar, "Performance of a rf neutralizer operating with noble gases and iodine," *Eur. Phys. J. Appl. Phys.* (published online 2020).
- <sup>209</sup>S. Matsuishi, Y. Toda, M. Miyakawa, K. Hayashi, T. Kamiya, M. Hirano, I. Tanaka, and H. Hosono, "High-density electron anions in a nanoporous single crystal: [Ca<sub>24</sub>Al<sub>28</sub>O<sub>64</sub>]<sup>4+</sup> (4e<sup>-</sup>)," *Science* **301**(5633), 626–629 (2003).
- <sup>210</sup>M. Lacerda, J. T. S. Irvine, F. P. Glasser, and A. R. West, "High oxide ion conductivity in Ca<sub>12</sub>Al<sub>14</sub>O<sub>33</sub>," *Nature* **332**, 525 (1988).
- <sup>211</sup>J. Jeevaratnam, F. P. Glasser, and L. S. D. Glasser, "Anion substitution and structure of 12CaO-7Al<sub>2</sub>O<sub>3</sub>," *J. Am. Ceram. Soc.* **47**(2), 105–106 (1964).
- <sup>212</sup>D.-K. Lee, L. Kogel, S. G. Ebbinghaus, I. Valov, H.-D. Wiemhoefer, M. Lerch, and J. Janek, "Defect chemistry of the cage compound, Ca<sub>12</sub>Al<sub>14</sub>O<sub>33-δ</sub> - understanding the route from a solid electrolyte to a semiconductor and electride," *Phys. Chem. Chem. Phys.* **11**, 3105–3114 (2009).
- <sup>213</sup>S.-W. Kim, S. Matsuishi, M. Miyakawa, K. Hayashi, M. Hirano, and H. Hosono, "Fabrication of room temperature-stable 12CaO-7Al<sub>2</sub>O<sub>3</sub> electride: A review," *J. Mater. Sci.* **18**(1), 5–14 (2007).
- <sup>214</sup>T. Yoshizumi, S. Matsuishi, S.-W. Kim, H. Hosono, and K. Hayashi, "Iodometric determination of electrons incorporated into cages in 12CaO-7Al<sub>2</sub>O<sub>3</sub> crystals," *J. Phys. Chem. C* **114**(36), 15354–15357 (2010).
- <sup>215</sup>S. W. Kim, T. Shimoyama, and H. Hosono, "Solvated electrons in high-temperature melts and glasses of the room-temperature stable electride [Ca<sub>24</sub>Al<sub>28</sub>O<sub>64</sub>]<sup>4+</sup> · 4e<sup>-</sup>," *Science* **333**(6038), 71–74 (2011).
- <sup>216</sup>M. Reitemeyer, D. Zschätzsch, K. Holste, L. Chen, and P. J. Klar, "Applicability of electride materials for hollow cathodes," in 36th International Electric Propulsion Conference, Vienna, Austria, 2019, IEPC-2019-604.

- <sup>217</sup>M. S. McDonald and N. R. S. Caruso, "Ignition and early operating characteristics of a low-current C12A7 hollow cathode," in 35th International Electric Propulsion Conference, Atlanta, GA, USA, 2017, IEPC-2017-253.
- <sup>218</sup>D. Rafalskyi and A. Aanesland, "Brief review on plasma propulsion with neutralizer-free systems," *Plasma Sources Sci. Technol.* **25**(4), 043001 (2016), URL: <https://doi.org/10.1088/1361-6595/25/4/043001>.
- <sup>219</sup>L. Blackhall and J. Khachan, "A simple electric thruster based on ion charge exchange," *J. Phys. D: Appl. Phys.* **40**(8), 2491–2494 (2007).
- <sup>220</sup>R. Boswell, C. Charles, P. Alexander, J. Dedrick, and K. Takahashi, "Plasma expansion from a radio frequency microdischarge," *IEEE Trans. Plasma Sci.* **39**(11), 2512–2513 (2011).
- <sup>221</sup>C. Charles and R. W. Boswell, "Measurement and modelling of a radiofrequency micro-thruster," *Plasma Sources Sci. Technol.* **21**(2), 022002 (2012).
- <sup>222</sup>S. Mitic, J. Kaupe, P. Riedl, and D. Coenen, "Comparative studies of compact kHz and MHz driven low pressure plasmas by emission and laser spectroscopy," *Phys. Plasmas* **26**(7), 073507 (2019).
- <sup>223</sup>E. Ahedo, "Plasmas for space propulsion," *Plasma Phys. Controlled Fusion* **53**(12), 124037 (2011).
- <sup>224</sup>F. Cannat, T. Lafleur, J. Jarrige, P. Chabert, P.-Q. Elias, and D. Packan, "Optimization of a coaxial electron cyclotron resonance plasma thruster with an analytical model," *Phys. Plasmas* **22**(5), 053503 (2015).
- <sup>225</sup>J. Yim and J. M. Burt, "Characterization of vacuum facility background gas through simulation and considerations for electric propulsion ground testing," in 51st AIAA/SAE/ASEE Joint Propulsion Conference, 2015.
- <sup>226</sup>A. Aanesland, S. Mazouffre, and P. Chabert, "Space Exploration technologies: PEGASES: A new promising electric propulsion concept," *Europhys. News* **42**, 28 (2011).
- <sup>227</sup>D. Rafalskyi and A. Aanesland, "Coincident ion acceleration and electron extraction for space propulsion using the self-bias formed on a set of RF biased grids bounding a plasma source," *J. Phys. D: Appl. Phys.* **47**, 495203 (2014).
- <sup>228</sup>F. F. Chen, *Introduction to Plasma Physics and Controlled Fusion*, Volume 1: Plasma Physics (Springer US, 1984).
- <sup>229</sup>R. Dendy, *Plasma Physics: An Introductory Course* (Cambridge University Press, 1993).
- <sup>230</sup>G. Guan, M. E. Mael, W. M. Holber, and J. B. O. Caughman, "A fluid description for the discharge equilibrium of a divergent electron cyclotron resonance plasma source," *Phys. Fluids B* **4**(12), 4177 (1992).
- <sup>231</sup>G. W. Hammett, M. A. Beer, W. Dorland, S. C. Cowley, and S. A. Smith, "Developments in the gyrofluid approach to tokamak turbulence simulations," *Plasma Phys. Controlled Fusion* **35**, 973 (1993).
- <sup>232</sup>J. M. Dawson, "Particle simulation of plasma," *Rev. Mod. Phys.* **55**(2), 403–447 (1983).
- <sup>233</sup>C. K. Birdsall and A. B. Langdon, *Plasma Physics via Computer Simulations* (CRC Press, 2004).
- <sup>234</sup>P. W. Rambo and J. Denavit, "Fluid and field algorithms for time-implicit plasma simulation," *J. Comput. Phys.* **92**, 185–212 (1991).
- <sup>235</sup>T. Tueckmantel and A. Pukhov, "H-VLPL: A three-dimensional relativistic PIC/fluid hybrid code," *J. Comput. Phys.* **269**, 168–180 (2014).
- <sup>236</sup>A. Stanier, L. Chacón, and G. Chen, "A fully implicit, conservative, non-linear, electromagnetic hybrid particle-ion/fluid-electron algorithm," *J. Comput. Phys.* **376**, 597–616 (2019).
- <sup>237</sup>J. Wang and Y. Hu, "On the limitations of hybrid particle-in-cell for ion thruster plume simulations," *Phys. Plasmas* **26**, 103502 (2019).
- <sup>238</sup>D. Tskhakaya, K. Matyash, R. Schneider, and F. Taccogna, "The particle-in-cell method," *Contrib. Plasma Phys.* **47**(8–9), 563–594 (2007).
- <sup>239</sup>T. Takizuka and H. Abe, "A binary collision model for plasma simulation with a particle code," *J. Comput. Phys.* **25**(3), 205–219 (1977).
- <sup>240</sup>C. K. Birdsall, "Particle-in-cell charged-particle simulations, plus Monte Carlo collisions with neutral atoms, PIC-MCC," *IEEE Trans. Plasma Sci.* **19**(2), 65 (1991).
- <sup>241</sup>V. Vahedi and M. S. Urendra, "A Monte Carlo collision model for the particle-in-cell method: Applications to argon and oxygen discharges," *Comput. Phys. Commun.* **87**(1–2), 179–198 (1995).
- <sup>242</sup>G. A. Bird, *Molecular Gas Dynamics and the Direct Simulation of Gas Flows* (Oxford Science Publications, 1994).
- <sup>243</sup>J. P. Verboncoeur, A. B. Langdon, and N. T. Gladd, "An object-oriented electromagnetic PIC code," *Comput. Phys. Commun.* **87**, 199–211 (1995).
- <sup>244</sup>P. Bumbarger, S. Shawver, J. Browning, D. Plumlee, S. M. Loo, D. Reis, and M. Yates, "Simulation and experimental analysis of a miniature ion thruster fabricated in low temperature co-fired ceramic," in 2012 Abstracts IEEE International Conference on Plasma Science (IEEE, Edinburgh, 2012).
- <sup>245</sup>P. Spaedke and S. Wipf, "KOBRA-3: A code for the calculation of space-charge-influenced trajectories in 3-dimensions," Technical Report No. GSI-89-09, 1989.
- <sup>246</sup>H. W. Loeb, J. Freisinger, K. H. Groh, and A. Scharmann, "State-of-the-art of the RIT ion thrusters and their spin-offs," in 39th Congress of the International Astronautical Federation, Bangalore, India, 1988, IAF-88-258.
- <sup>247</sup>D. Eremin, T. Hemke, R. P. Brinkmann, and T. Mussenbrock, "Kinetic simulation of radio-frequency driven plasmas in He/O<sub>2</sub> mixtures at atmospheric pressure," in Proceedings of 64th Annual Gaseous Electronics Conference, Salt Lake City, UT, USA, 2011.
- <sup>248</sup>T. Binder, "Numerical simulations of ion thruster-induced plasma dynamics," Ph.D. thesis, University of Braunschweig, 2001.
- <sup>249</sup>H. Meusemann and M. Winter, "Electric propulsion in Germany: Current program and perspectives," in 29th International Electric Propulsion Conference, Princeton, NJ, USA, 2005, IEPC-2005-130.
- <sup>250</sup>G. Herdrich *et al.*, "Activities in electric propulsion development at IRS," *Trans. Jpn. Soc. Aeronaut. Space Sci., Space Technol. Jpn.* **7**(ists26), Tb\_5 (2009).
- <sup>251</sup>D. Kahnfeld, "Numerical simulations of ion thruster-induced plasma dynamics," Ph.D. thesis, University of Greifswald, 2019.
- <sup>252</sup>O. Kalentev, J. Duras, K. F. Luskow, K. Matyash, and R. Schneider, "Strategy of multiscale modelling for combined thruster-plume models," in 33rd International Electric Propulsion Conference, Washington, DC, USA, 2013, IEPC-2013-126.
- <sup>253</sup>O. Kalentev, K. Matyash, J. Duras, K. F. Luskow, R. Schneider, N. Koch, and M. Schirra, "Electrostatic ion thrusters - towards predictive modeling," *Contrib. Plasma Phys.* **54**(2), 235–248 (2014).
- <sup>254</sup>A. Passaro, L. Biagioni, and M. Andreucci, "PIC/DSMC models for Hall effect thruster plumes: Present status and ways forward," AIAA Paper No. 2002-4254, 2012.
- <sup>255</sup>R. Jambunathan and D. A. Levin, "Multi-GPU PIC-DSMC solver for modeling ion thruster plasma plume and neutralization," AIAA Paper No. 2018-1297, 2018.
- <sup>256</sup>J. Derouillat, A. Beck, F. Pérez, T. Vinci, M. Chiamello, A. Grassi, M. Flé, G. Bouchard, I. Plotnikov, N. Aunai, J. Dargent, C. Riconda, and M. Grech, "Smilei: A collaborative, open-source, multi-purpose particle-in-cell code for plasma simulation," *Comput. Phys. Commun.* **222**, 351–373 (2018).
- <sup>257</sup>S. Fasoulas, C.-D. Munz, M. Pfeiffer, J. Beyer, T. Binder, S. Copplestone, A. Mirza, P. Nizenzov, P. Ortwein, and W. Reschke, "Combining particle-in-cell and direct simulation Monte Carlo for the simulation of reactive plasma flows," *Phys. Fluids* **31**, 072006 (2019).
- <sup>258</sup>R. Henrich, "Development of a plasma simulation tool for radio frequency ion thrusters," Ph.D. thesis, Justus-Liebig-University Giessen, 2013.
- <sup>259</sup>M. Becker, "Development of a parallel multigrid field solver for large-scale particle-in-cell applications," Ph.D. thesis, Justus-Liebig-University Giessen, 2018.
- <sup>260</sup>M. Invigorito, D. Ricci, F. Battista, and V. Salvatore, "CIRA roadmap for the development of electric propulsion test facilities," in Space Propulsion Conference, Rome, Italy, 2016.
- <sup>261</sup>A. Neumann and E. T. STG-, "DLR electric propulsion test facility," *J. Large-Scale Res. facilities JLSRF* **4**, 134 (2018).
- <sup>262</sup>C. Bundesmann, C. Eichhorn, F. Scholze, D. Spemann, H. Neumann, D. Pagano, S. Scaranzin, F. Scortecci, H. J. Leiter, S. Gauter, R. Wiese, H. Kersten, K. Holste, P. Köhler, P. J. Klar, S. Mazouffre, R. Blott, A. Bulit, and K. Dannenmayer, "An advanced electric propulsion diagnostic (AEPD) platform for in-situ characterization of electric propulsion thrusters and ion beam sources," *Eur. Phys. J. D* **70**(10), 212 (2016).
- <sup>263</sup>A. Galli, A. Vorburger, A. Pommerol, P. Wurzel, B. Jost, O. Poch, Y. Brouet, M. Tulej, and N. Thomas, "Surface charging of thick porous water ice layers relevant for ion sputtering experiments," *Planet. Space Sci.* **126**, 63–71 (2016).
- <sup>264</sup>J. Van Noord and G. Soulas, "A facility and ion thruster backscatter survey for higher power ion thrusters," in 41st AIAA/ASME/SAE/ASEE Joint Propulsion Conference and Exhibit, Tucson, AZ, 10–13 July 2005.

- <sup>265</sup>H. Zheng, G. Cai, L. Liu, S. Shang, and B. He, "Three-dimensional particle simulation of back-sputtered carbon in electric propulsion test facility," *Acta Astronaut.* **132**, 161–169 (2017).
- <sup>266</sup>C. Bundesmann, C. Eichhorn, F. Scholze, D. Spemann, H. Neumann, F. Scortecci, H. J. Leiter, K. Holste, P. J. Klar, A. Bulit, K. Dannenmayer, and J. Gonzales del Amo, "Advanced electric propulsion diagnostic tools at IOM," *Procedia Eng.* **185**, 1–8 (2017).
- <sup>267</sup>F. Scortecci, D. Pagano, C. Bundesmann, C. Eichhorn, F. Scholze, D. Spemann, H. Leiter, H. Kersten, R. Blott, S. Mazouffre, P. Klar, D. Feili, and J. Gonzales del Amo, "AEPD system as a standard on-ground tool for electric propulsion thrusters," in 35th International Electric Propulsion Conference, Atlanta, GA, USA, 2017, IEPC-2017-33.
- <sup>268</sup>J. S. Snyder, J. Baldwin, J. D. Frieman, M. L. R. Walker, N. S. Hicks, K. A. Polzin, and J. T. Singleton, "Recommended practice for flow control and measurement in electric propulsion testing," *J. Propul. Power* **33**(3), 556–565 (2017).
- <sup>269</sup>J. Dankanich, M. Swiatek, and J. Yim, "A step towards electric propulsion testing standards: Pressure measurements and effective pumping speeds," in 48th AIAA/ASME/SAE/ASEE Joint Propulsion Conference and Exhibit, Atlanta, GA, USA, July 2012.
- <sup>270</sup>J. E. Polk, A. Pancotti, T. Haag, S. King, M. Walker, J. Blakely, and J. Ziemer, "Recommended practice for thrust measurement in electric propulsion testing," *J. Propul. Power* **33**(3), 539–555 (2017).
- <sup>271</sup>R. B. Lobbia and B. E. Beal, "Recommended practice for use of Langmuir probes in electric propulsion testing," *J. Propul. Power* **33**(3), 566–581 (2017).
- <sup>272</sup>J. P. Sheehan, Y. Raitses, N. Hershkovitz, and M. McDonald, "Recommended practice for use of emissive probes in electric propulsion testing," *J. Propul. Power* **33**(3), 614–637 (2017).
- <sup>273</sup>C. C. Farnell, C. C. Farnell, S. C. Farnell, and J. D. Williams, "Recommended practice for use of electrostatic analyzers in electric propulsion testing," *J. Propul. Power* **33**(3), 638–658 (2017).
- <sup>274</sup>D. L. Brown, M. L. R. Walker, J. Szabo, W. Huang, and J. E. Foster, "Recommended practice for use of faraday probes in electric propulsion testing," *J. Propul. Power* **33**(3), 582–613 (2017).
- <sup>275</sup>*MEMS and Microstructures in Aerospace Applications*, edited by R. Oslander, M. A. Garrison Darrin, and J. L. Champion (Taylor & Francis, 2006).
- <sup>276</sup>T. Schönherr, B. Little, D. Krejci, A. Reissner, and B. Seifert, "Development, production, and testing of the IFM nano FEEP thruster," in 36th International Electric Propulsion Conference, Vienna, Austria, 2019, IEPC-2019-362.
- <sup>277</sup>D. G. Courtney, Z. Wood, S. Gray, and J. Model, "High-speed transient characterization of the Busek BET-300-P electrospray thruster," in 36th International Electric Propulsion Conference, Vienna, Austria, 2019, IEPC-2019-788.
- <sup>278</sup>D. Di Cara, A. Bulit, J. Gonzalez del Amo, J. A. Romera, H. Leiter, D. Lauer, C. Altmann, R. Kukies, A. Polli, L. Ceruti, A. Antimiani, D. Feili, B. Lotz, and L. Serafini, "Experimental validation of RIT micro-propulsion subsystem performance at EPL," in 33rd International Electric Propulsion Conference, Washington, DC, USA, 2013, IEPC-2013-90.
- <sup>279</sup>D. Krejci and P. Lozano, "Space propulsion technology for small spacecraft," *Proc. IEEE* **106**(3), 362–378 (2018).
- <sup>280</sup>J. Gonzalez del Amo, "European Space Agency (ESA) electric propulsion activities," in 34th International Electric Propulsion Conference, Kobe, Japan, 2015, IEPC-2015-02.
- <sup>281</sup>M. Smirnova, A. Mingo, J. Schein, P. Smirnov, E. Bosch, and L. Massotti, "Test campaign on the novel variable ISP radio frequency mini ion engine," in 36th International Electric Propulsion Conference, Vienna, Austria, 2019, IEPC-2019-574.
- <sup>282</sup>H. J. Leiter, D. Lauer, P. Bauer, M. Berger, and M. Rath, "The Ariane group electric propulsion program 2019–2020," in 36th International Electric Propulsion Conference, Vienna, Austria, 2019, IEPC-2019-592.
- <sup>283</sup>K. Lemmer, "Propulsion for CubeSats," *Acta Astronaut.* **134**, 231–243 (2017).
- <sup>284</sup>I. Levchenko, K. Bazaka, Y. Ding, Y. Raitses, S. Mazouffre, T. Henning, P. J. Klar, S. Shinohara, J. Schein, L. Garrigues, M. Kim, D. Lev, F. Taccogna, R. W. Boswell, C. Charles, H. Koizumi, Y. Shen, C. Scharlemann, M. Keidar, and S. Xu, "Space micropropulsion systems for CubeSats and small satellites: From proximate targets to furthest frontiers," *Appl. Phys. Rev.* **5**, 011104-1–011104-36 (2018).
- <sup>285</sup>K. Huhn, M. Piechotka, T. Henning, and P. J. Klar, "Investigation of the emission behavior of miniaturized SU-8 based colloid emitters," in 33rd International Electric Propulsion Conference, Washington, DC, 2013, IEPC-2013-141.
- <sup>286</sup>M. Martinez-Sanchez and P. Lozano, "16.522 space propulsion," Spring 2015, Massachusetts Institute of Technology: MIT Open CourseWare. License: Creative Commons BY-NC-SA, <https://ocw.mit.edu/courses/aeronautics-and-astronautics/16-522-space-propulsion-spring-2015/lecture-notes/>.
- <sup>287</sup>S. Dandavino, C. Ataman, C. N. Ryan, S. Chakraborty, D. Courtney, J. P. W. Stark, and H. Shea, "Microfabricated electrospray emitter arrays with integrated extractor and accelerator electrodes for the propulsion of small spacecraft," *J. Micromech. Microeng.* **24**, 075011-1–075011-13 (2014).
- <sup>288</sup>E. Gustan-Gutierrez and M. Gamero-Castaño, "Microfabricated electrospray thruster array with high hydraulic resistance channels," *J. Propul. Power* **33**(4), 984–991 (2017).
- <sup>289</sup>See <https://www.enpulsion.com/> for information about commercially available micro- and nanothrusters for CubeSat applications.
- <sup>290</sup>S. Marcuccio, N. Giusti, and A. Tolstoguzov, "Characterization of linear slit FEEP using a ionic liquid propellant," in 31st International Electric Propulsion Conference (University of Michigan, Ann Arbor, MI, USA, 2009), IEPC-2009-180.
- <sup>291</sup>L. F. Velázquez-García, A. I. Akinwande, and M. Martínez-Sánchez, "A micro-fabricated linear array of electrospray emitters for thruster applications," *J. Microelectromech. Syst.* **15**(5), 1260–1271 (2006).
- <sup>292</sup>L. F. Velázquez-García, A. I. Akinwande, and M. Martínez-Sánchez, "A planar array of micro-fabricated electrospray emitters for thruster applications," *J. Microelectromech. Syst.* **15**(5), 1272–1280 (2006).
- <sup>293</sup>Y. Takao, N. Inoue, K. Suzuki, F. Tachibana, M. Nagao, and K. Murakami, "Development of ionic liquid electrospray thrusters with a massive emitter array for higher thrust density," in 36th International Electric Propulsion Conference, Vienna, Austria, 2019, IEPC-2019-149.
- <sup>294</sup>M. Piechotka, K. Huhn, T. Henning, D. Feili, and P. J. Klar, "Microfabrication of colloid emitters based on the photo resist SU-8 and electro plating," in 32nd International Electric Propulsion Conference, Wiesbaden, 2011, IEPC-2011-276.
- <sup>295</sup>B. J. Kim and E. Meng, "Review of polymer MEMS micromachining," *J. Micromech. Microeng.* **26**, 013001-1–013001-21 (2016).
- <sup>296</sup>A. d. Campo and C. Greiner, "SU-8: A photoresist for high-aspect-ratio and 3D submicron lithography," *J. Micromech. Microeng.* **17**, R81–R95 (2007).
- <sup>297</sup>A. Mata, A. J. Fleischman, and S. Roy, "Fabrication of multi-layer SU-8 microstructures," *J. Micromech. Microeng.* **16**, 276–284 (2006).
- <sup>298</sup>T. Henning, K. Huhn, S. Hengsbach, K. Bade, and P. J. Klar, "Additive manufacturing of electrospray emitters at the microscale," in Space Propulsion 2018 conference, Sevilla, Spain, 2018, SP2016\_070.
- <sup>299</sup>T. Henning, K. Huhn, and P. J. Klar, "Characterisation of electrospray microemitters fabricated by planar and 3D photolithography," in 36th International Electric Propulsion Conference, Vienna, Austria, 2019, IEPC-2019-344.
- <sup>300</sup>M. Malinauskas, V. Purlys, M. Rutkauskas, and R. Gadonas, "Two-photon polymerization for fabrication of three-dimensional micro- and nanostructures over a large area," *Proc. SPIE* **7204**, 72040C-1–72040C-11 (2009).
- <sup>301</sup>See <https://www.nanoscribe.com/> for details about the commercially available 3D microlithography device in use at JLU for designing electrospray emitters.
- <sup>302</sup>F. Niesler and M. Hermatschweiler, "Two-photon polymerization—A versatile microfabrication tool," *Laser Tech. J.* **12**, 44–47 (2015).
- <sup>303</sup>T. Henning, K. Huhn, S. Feng, Z. Xie, S. Hengsbach, K. Bade, and P. J. Klar, "Three-dimensional lithography for the microfabrication of colloid emitters," in Space Propulsion 2016 Conference, Rome, 02/06 May 2016, SP2016\_3124766.
- <sup>304</sup>C. Tato, F. de la Cruz, and J. Palencia, "Power control unit for ion propulsion assembly in GOCE program," in 30th International Electric Propulsion Conference, Florence, Italy, 2007, IEPC-2007-295.
- <sup>305</sup>F. Pintó, J. Palencia, G. Glorieux, and N. Wagner, "Airbus defence and space power processing units: New HET and GIT PPU developments qualification status," in 35th International Electric Propulsion Conference, Atlanta, GA, USA, 2017, IEPC-2017-266.
- <sup>306</sup>C. Bowick, *RF Circuit Design* (Newnes, 2007).
- <sup>307</sup>R. L. Steigerwald, "A comparison of half-bridge resonant converter topologies," *IEEE Trans. Power Electron.* **3**(2), 174–182 (1988).



- <sup>308</sup>J. Simon, U. Probst, and P. J. Klar, "Development of a radio-frequency generator for RF ion thrusters," *Trans. Jpn. Soc. Aeronaut. Space Sci.* **14**(ists30), Pb\_33–Pb\_39 (2016).
- <sup>309</sup>J. Simon and U. Probst, "High-Performance digital-controlled radio-frequency generator for RF ion thrusters," in Proceedings of the 6th Russian-German Conference on Electric Propulsions and Their Application, 2016.
- <sup>310</sup>J. Simon, "Entwicklung und aufbau eines radiofrequenzgenerators zur versorgung und elektrischen charakterisierung induktiv-gekoppelter plasmen in radiofrequenz-ionentriebwerken," Ph.D. thesis, Justus Liebig Universität Gießen, 2016.
- <sup>311</sup>J. E. Junker, U. Probst, and P. J. Klar, "An alternative circuit topology for radio-frequency generators driving RIT," in Proceedings of the 7th Russian-German Conference on Electric Propulsion and Their Applications, 2018.
- <sup>312</sup>J. E. Junker, U. Probst, and P. J. Klar, "Development of a full bridge series resonant radio-frequency generator for optimized RIT operation," in 36th International Electric Propulsion Conference, Vienna, Austria, 2019, IEPC-2019-474.
- <sup>313</sup>R. Redl, N. O. Sokal, and L. Balogh, "A novel soft-switching full-bridge DC/DC converter: Analysis, design considerations, and experimental results at 1.5 kW, 100 kHz," *IEEE Trans. Power Electron.* **6**(3), 408–418 (1991).
- <sup>314</sup>J. A. Sabate, V. Vlatkovic, R. B. Ridley, F. C. Lee, and B. H. Cho, "Design considerations for high-voltage high-power full-bridge zero-voltage-switched PWM converter," in Fifth Annual Proceedings on Applied Power Electronics Conference and Exposition, 1990.
- <sup>315</sup>R. Redl, L. Balogh, and D. W. Edwards, "Optimum ZVS full-bridge DC/DC converter with PWM phase-shift control: Analysis, design considerations, and experimental results," in *Proceedings of 1994 IEEE Applied Power Electronics Conference and Exposition - ASPEC'94* (IEEE, 1994).
- <sup>316</sup>F. Belloni, R. Grossi, P. G. Maranesi, and M. Riva, "HV driver for ion thrusters," in 2005 European Conference on Power Electronics and Applications, Dresden, Germany, 2005.
- <sup>317</sup>A. Peña, F. Santamaría, and E. A. Narváez, "Operation of the phase-shifted zero-voltage-switching full-bridge dc/dc converter: Analysis and design considerations," *Tecnura J.* **19**, 176–183 (2015).
- <sup>318</sup>Y. Jiang, Z. Chen, J. Pan, X. I. Zhao, and P. Lee, "A novel phase-shift full-bridge converter with voltage-doubler and decoupling integrated magnetics in PV system," *Bull. Pol. Acad. Sci.: Tech. Sci.* **56**(3), 285 (2008).
- <sup>319</sup>P. Maranesi, "The switch in-line converter," in *Proceedings of IEEE Power Electronics Specialist Conference - PESC '93* (IEEE, 1993).
- <sup>320</sup>F. Belloni, P. G. Maranesi, and M. Riva, "DC/DC converter for the international space station," *IEEE Trans. Aerosp. Electron. Syst.* **46**(2), 623–634 (2010).
- <sup>321</sup>C. Rößler, U. Probst, J. Simon, and P. J. Klar, "Development of a controlled high voltage power supply for gridded ion thrusters," in 35th International Electric Propulsion Conference, Atlanta, GA, USA, 2017, IEPC-2017-337.
- <sup>322</sup>C. Rößler, U. Probst, and P. J. Klar, "Design and implementation of a high voltage supply for gridded ion thrusters using model-based control algorithms," in 36th International Electric Propulsion Conference, 2019, IEPC-2019-409.
- <sup>323</sup>T. Baruth, "Untersuchungen zur elektromagnetischen verträglichkeit von radiofrequenz-ionentriebwerken am beispiel eines RIT4," Ph.D. thesis, Justus-Liebig-Universität Gießen, 2017.
- <sup>324</sup>J. J. Goedbloed, "Electromagnetic compatibility," *Phys. Technol.* **18**(2), 61–67 (1987).
- <sup>325</sup>V. M. Arbatskiy, S. V. Baranov, N. A. Vazhenin, A. P. Plokhikh, and G. A. Popov, "Peculiarities of determination of electromagnetic interference emission from electric propulsion thrusters under ground conditions," *Procedia Eng.* **185**, 97–104 (2017).
- <sup>326</sup>E. Beiting and M. Garrett, "Facility for high-fidelity electromagnetic compatibility studies of electric thrusters," in 43rd AIAA/ASME/SAE/ASEE Joint Propulsion Conference and Exhibit, July 2007.
- <sup>327</sup>D. Bräunig, *Wirkung hochenergetischer Strahlung auf Halbleiterbauelemente*, 1st ed., Mikroelektronik (Springer-Verlag Berlin Heidelberg, 1989).
- <sup>328</sup>M. Tanabashi *et al.*, "Review of particle physics," *Phys. Rev. D* **98**(3), 030001 (2018).
- <sup>329</sup>M. Martucci *et al.*, "Proton fluxes measured by the PAMELA experiment from the minimum to the maximum solar activity for solar cycle 24," *Astrophys. J.* **854**(1), L2 (2018).
- <sup>330</sup>E. Robbrecht and D. Berghmans, "Automated recognition of coronal mass ejections (CMEs) in near-real-time data," *Astron. Astrophys.* **425**(3), 1097–1106 (2004).
- <sup>331</sup>E. Robbrecht, D. Berghmans, and R. A. M. Van der Linden, "Automated LASCO CME catalog for solar cycle 23: Are CMEs scale invariant?," *Astrophys. J.* **691**(2), 1222–1234 (2009).
- <sup>332</sup>S. C. Rogers, "Radiation damage to satellite electronic systems," *IEEE Trans. Nucl. Sci.* **10**(1), 97–105 (1963).
- <sup>333</sup>A. S. Oates, "Reliability of silicon integrated circuits," in *Reliability Characterisation of Electrical and Electronic Systems*, edited by J. Swingler (Woodhead Publishing, Oxford, 2015), Chap. 7, pp. 115–141.
- <sup>334</sup>T. S. Nidhin, A. Bhattacharyya, R. P. Behera, and T. Jayanthi, "A review on SEU mitigation techniques for FPGA configuration memory," *IETE Tech. Rev.* **35**(2), 157–168 (2018).
- <sup>335</sup>M. J. Campola and J. A. Pellish, "Radiation hardness assurance: Evolving for NewSpace," in 30th European Conference on Radiation Effects on Components and Systems, Montpellier, France, 2019, URL: <https://ntrs.nasa.gov/search.jsp?R=20190031733>.
- <sup>336</sup>D. Shougang, Y. Suge, L. Hongxia, F. Long, and Z. Hongchao, "Predictions for proton and heavy ions induced SEUs in 65 nm SRAMs," *J. Semicond.* **36**(11), 114010 (2015).
- <sup>337</sup>NASA Goddard Space Flight Center, GSFC radiation data base, <https://radhome.gsfc.nasa.gov/radhome/RadDataBase/RadDataBase.html>.
- <sup>338</sup>JEDEC, Test standard for the measurement of proton radiation single event effects in electronic devices, <https://www.jedec.org/standards-documents/docs/jesd234>.
- <sup>339</sup>JEDEC, Test methods for real-time soft error rate. <https://www.jedec.org/standards-documents/docs/jesd-89-1a>.
- <sup>340</sup>E. Daly *et al.*, "Standards for space radiation environments and effects," in *Proceedings of the 7th European Conference on Radiation and Its Effects on Components and Systems, 2003, RADECS 2003* (IEEE, 2003), pp. 175–179.
- <sup>341</sup>A. J. Tylka *et al.*, "CREME96: A revision of the cosmic ray effects on micro-electronics code," *IEEE Trans. Nucl. Sci.* **44**(6), 2150–2160 (1997).
- <sup>342</sup>The PANDA Collaboration, "Technical design report for PANDA electromagnetic calorimeter (EMC)," [arXiv:0810.1216](https://arxiv.org/abs/0810.1216) [physics.ins-det] (2008).
- <sup>343</sup>K. Peters, L. Schmitt, T. Stockmanns, and J. Messchendorp, "PANDA: Strong interaction studies with antiprotons," *Nucl. Phys. News* **27**(3), 24–28 (2017).
- <sup>344</sup>B. C. Lee, W. Huang, L. Tao, N. Yamamoto, A. D. Gallimore, and A. P. Yalin, "A cavity ring-down spectroscopy sensor for real-time Hall thruster erosion measurements," *Rev. Sci. Instrum.* **85**(5), 053111 (2014).
- <sup>345</sup>R. V. Akhmetzhanov, A. V. Bogaty, E. V. Vorob'ev, D. V. Dukhopel'nikov, D. A. Kashirin, V. A. Obukhov, G. A. Popov, V. V. Svtina, and M. V. Cherkasova, "Two-electrode ion-extraction system of a radio-frequency ion source: Numerical and experimental studies of erosion of the accelerating electrode," *J. Surf. Invest.: X-Ray, Synchrotron Neutron Tech.* **13**(6), 1061–1066 (2019).
- <sup>346</sup>M. Celik, O. Batishchev, and M. Martinez-Sanchez, "Use of emission spectroscopy for real-time assessment of relative wall erosion rate of BHT-200 Hall thruster for various regimes of operation," *Vacuum* **84**(9), 1085–1091 (2010).
- <sup>347</sup>A. Sengupta, J. A. Anderson, C. Garner, J. R. Brophy, K. K. de Groh, B. A. Banks, and T. A. K. Thomas, "Deep space 1 flight spare ion thruster 30,000-hour life test," *J. Propul. Power* **25**(1), 105–117 (2009).
- <sup>348</sup>R. E. Wirz, J. R. Anderson, D. M. Goebel, and I. Katz, "Decel grid effects on ion thruster grid erosion," *IEEE Trans. Plasma Sci.* **36**(5), 2122–2129 (2008).
- <sup>349</sup>D. Yu and Y. Li, "Volumetric erosion rate reduction of hall thruster channel wall during ion sputtering process," *J. Phys. D: Appl. Phys.* **40**(8), 2526–2532 (2007).
- <sup>350</sup>R. I. S. Roy, D. E. Hastings, and N. A. Gastonis, "Ion-thruster plume modeling for backflow contamination," *J. Spacecr. Rockets* **33**(4), 525–534 (1996).
- <sup>351</sup>S. Madeev, M. Selivanov, A. Shagayda, and A. Lovtsov, "Experimental study of ion optics with square apertures for high-power ion thrusters," *Rev. Sci. Instrum.* **90**(4), 043302 (2019).
- <sup>352</sup>S. Satori, Y. Shimizu, K. Toki, H. Kuninaka, and K. Kuriki, "Experimental investigation of carbon contamination inside discharge chamber of ion thruster," *Trans. Jpn. Soc. Aeronaut. Space Sci.* **41**(134), 216–218 (2000).



- <sup>353</sup>T. Meng, C. Qiao, Y. Wang, Z. Ning, and D. Yu, "Accelerated erosion of keeper electrode during coupling discharge between Hall thruster and hollow cathode," *Vacuum* **172**, 109040 (2020).
- <sup>354</sup>W. Ohmichi and H. Kuninaka, "Performance degradation of a spacecraft electron cyclotron resonance neutralizer and its mitigation," *J. Propul. Power* **30**(5), 1368–1372 (2014).
- <sup>355</sup>L. N. Ahmed and M. W. Crofton, "Surface modification measurements in the T5 ion thruster plume," *J. Propul. Power* **14**(3), 336–347 (1998).
- <sup>356</sup>J. Duras, O. Kalentev, R. Schneider, K. Matyash, K. F. Luskow, and J. Geiser, "Electrostatic ion thrusters - towards predictive modeling," *Acta Polytech.* **55**(1), 7–13 (2015).
- <sup>357</sup>J.-F. Roussel, T. Tondou, J.-C. Mateo-Velez, E. Chesta, S. D'Escrivan, and L. Perraud, "Modeling of FEEP plume effects on MICROSCOPE spacecraft," *IEEE Trans. Plasma Sci.* **36**(5), 2378–2386 (2008).
- <sup>358</sup>P. Sigmund, "Theory of sputtering. I. Sputtering yield of amorphous and polycrystalline targets," *Phys. Rev.* **184**(2), 383–416 (1969).
- <sup>359</sup>M. Tartz, T. Heyn, C. Bundesmann, C. Zimmermann, and H. Neumann, "Sputter yields of Mo, Ti, W, Al, Ag under xenon ion incidence," *Eur. Phys. J. D* **61**(3), 587–592 (2011).
- <sup>360</sup>T. Nenadović, B. Perrailon, Ž. Bogdanov, Z. Djordjević, and M. Milić, "Sputtering and surface topography of oxides," *Nucl. Instrum. Methods Phys. Res., Sect. B* **48**(1), 538–543 (1990).
- <sup>361</sup>R. Behrisch and W. Eckstein, *Sputtering by Particle Bombardment: Experiments and Computer Calculations from Threshold to MeV Energies* (Springer Science & Business Media, 2007), Vol. 110.
- <sup>362</sup>H. F. Winters and J. W. Coburn, "Surface science aspects of etching reactions," *Surf. Sci. Rep.* **14**(4–6), 162–269 (1992).
- <sup>363</sup>M. Wahl and A. Wucher, "VUV photoionization of sputtered neutral silver clusters," *Nucl. Instrum. Methods Phys. Res., Sect. B* **94**(1–2), 36–46 (1994).
- <sup>364</sup>H. Tsuge and S. Esho, "Angular distribution of sputtered atoms from polycrystalline metal targets," *J. Appl. Phys.* **52**(7), 4391–4395 (1981).
- <sup>365</sup>T. Aoyama, M. Tanemura, and F. Okuyama, "Angular distribution of particles sputtered from GaAs by Ar<sup>+</sup> and Xe<sup>+</sup> ion bombardment," *Appl. Surf. Sci.* **100–101**, 351–354 (1996).
- <sup>366</sup>T. Mousel, W. Eckstein, and H. Gnaser, "Energy spectra of sputtered species under sub-keV ion bombardment: Experiments and computer simulations," *Nucl. Instrum. Methods Phys. Res., Sect. B* **152**(1), 36–48 (1999).
- <sup>367</sup>J. B. Malherbe, "Sputtering of compound semiconductor surfaces. I. Ion-solid interactions and sputtering yields," *Crit. Rev. Solid State* **19**(2), 55–127 (1994).
- <sup>368</sup>R. Behrisch, G. Maderlechner, B. M. U. Scherzer, and M. T. Robinson, "The sputtering mechanism for low-energy light ions," *Appl. Phys.* **18**(4), 391–398 (1979).
- <sup>369</sup>V. S. Smentkowski, "Trends in sputtering," *Prog. Surf. Sci.* **64**(1–2), 1–58 (2000).
- <sup>370</sup>C. García-Rosales, W. Eckstein, and J. Roth, "Revised formulae for sputtering data," *J. Nucl. Mater.* **218**(1), 8–17 (1995).
- <sup>371</sup>M. P. Seah, "Pure element sputtering yields using 500–1000 eV argon ions," *Thin Solid Films* **81**(3), 279–287 (1981).
- <sup>372</sup>Ch. Steinbruechel, "A simple formula for low-energy sputtering yields," *Appl. Phys. A* **36**(1), 37–42 (1985).
- <sup>373</sup>D. Rosenberg and G. K. Wehner, "Sputtering yields for low energy He<sup>+</sup>, Kr<sup>+</sup>, and Xe<sup>+</sup> ion bombardment," *J. Appl. Phys.* **33**(5), 1842–1845 (1962).
- <sup>374</sup>R. V. Stuart and G. K. Wehner, "Sputtering thresholds and displacement energies," *Phys. Rev. Lett.* **4**(8), 409–410 (1960).
- <sup>375</sup>J. Roth, W. Eckstein, E. Gauthier, and J. Laszlo, "Sputtering of low-Z materials," *J. Nucl. Mater.* **179–181**, 34–36 (1991).
- <sup>376</sup>K. B. Cheney and E. T. Pitkin, "Sputtering at acute incidence," *J. Appl. Phys.* **36**(11), 3542–3544 (1965).
- <sup>377</sup>H. Oechsner, "Sputtering—A review of some recent experimental and theoretical aspects," *Appl. Phys.* **8**(3), 185–198 (1975).
- <sup>378</sup>O. Almén and G. Bruce, "Collection and sputtering experiments with noble gas ions," *Nucl. Instrum. Methods Phys. Res., Sect. B* **11**, 257–278 (1961).
- <sup>379</sup>W. Höslér and W. Pamler, "Effects of crystallinity on depth resolution in sputter depth profiles," *Surf. Interface Anal.* **20**(8), 609–620 (1993).
- <sup>380</sup>H. Winter, "Scattering of atoms and ions from insulator surfaces," *Prog. Surf. Sci.* **63**(7–8), 177–247 (2000).
- <sup>381</sup>Z. L. Liao, W. L. Brown, R. Homer, and J. M. Poate, "Surface-layer composition changes in sputtered alloys and compounds," *Appl. Phys. Lett.* **30**(12), 626–628 (1977).
- <sup>382</sup>H. Gnaser, "Processes in low-energy ion-surface collisions: Preferential sputtering, defect and adatom formation," *Appl. Surf. Sci.* **100–101**, 316–328 (1996).
- <sup>383</sup>D. F. Mitchell, G. I. Sproule, and M. J. Graham, "Sputter reduction of oxides by ion bombardment during Auger depth profile analysis," *Surf. Interface Anal.* **15**(8), 487–497 (1990).
- <sup>384</sup>S. J. Chey and D. G. Cahill, "Surface defects created by low energy ( $20 < E < 240$  eV) ion bombardment of Ge(001)," *Surf. Sci.* **380**(2–3), 377–384 (1997).
- <sup>385</sup>H. Saitoh, T. Kyuno, I. Hosoda, and R. Urao, "Surface morphology of polycrystalline diamond films etched by Ar<sup>+</sup> beam bombardment," *J. Mater. Sci.* **31**(3), 603–606 (1996).
- <sup>386</sup>G. K. Wehner, "Velocities of sputtered atoms," *Phys. Rev.* **114**(5), 1270–1272 (1959).
- <sup>387</sup>G. K. Wehner and D. Rosenberg, "Angular distribution of sputtered material," *J. Appl. Phys.* **31**(1), 177–179 (1960).
- <sup>388</sup>H. Oechsner and L. Reichert, "Energies of neutral sputtered particles," *Phys. Lett.* **23**(1), 90–92 (1966).
- <sup>389</sup>P. Sigmund, "LSS and the integral equations of transport theory," *Phys. Scr.* **28**(3), 257–267 (1983).
- <sup>390</sup>W. Szymczak and K. Wittmaack, "Angular distributions of gold sputtered from a (111) crystal: Dependence of spot shapes and of spot and background yields on the primary ion mass and energy and on the target temperature," *Nucl. Instrum. Methods Phys. Res., Sect. B* **82**(2), 220–233 (1993).
- <sup>391</sup>H. Gnaser and W. O. Hofer, "The emission of neutral clusters in sputtering," *Appl. Phys. A* **48**(3), 261–271 (1989).
- <sup>392</sup>R. B. Jackman, "Ion beam-assisted etching of semiconductors: Surface chemistry vs surface physics," *Vacuum* **44**(3–4), 239–243 (1993).
- <sup>393</sup>P. Sigmund and A. Gras-Marti, "Distortion of depth profiles during sputtering," *Nucl. Instrum. Methods* **168**(1–3), 389–394 (1980).
- <sup>394</sup>U. Littmark and W. O. Hofer, "Recoil mixing in solids by energetic ion beams," *Nucl. Instrum. Methods* **168**(1–3), 329–342 (1980).
- <sup>395</sup>K. Schmid, J. Roth, and W. Eckstein, "Influence of diffusion on W sputtering by carbon," *J. Nucl. Mater.* **290–293**, 148–152 (2001).
- <sup>396</sup>J. W. Coburn and H. F. Winters, "Plasma etching—A discussion of mechanisms," *J. Vac. Sci. Technol.* **16**(2), 391–403 (1979).
- <sup>397</sup>I. Utke, P. Hoffmann, and J. Melngailis, "Gas-assisted focused electron beam and ion beam processing and fabrication," *J. Vac. Sci. Technol.* **26**(4), 1197 (2008).